Transition metal oxide and sulphide based electrochemical sensing and super-capacitance

By

BARNAMALA SAHA

PHYS05201204002

Saha Institute of Nuclear Physics

A thesis submitted to the

Board of Studies in Physical Sciences

In partial fulfilment of requirements

for the Degree of

DOCTOR OF PHILOSOPHY

of

HOMI BHABHA NATIONAL INSTITUTE

July, 2018

Homi Bhabha National Institute[1]

Recommendations of the Viva Voce Committee

As members of the Viva Voce Committee, we certify that we have read the dissertation prepared by <Candidate Name> entitled <" Title" > and recommend that it may be accepted as fulfilling the thesis requirement for the award of Degree of Doctor of Philosophy.

RBhattacharyya

Chairman - <Name> SATYA RANJAN BHATTACHARYYA Date: 07/12/2018

Guide / Convener - <Name> SANGAM BANERJEE Date: 07/12/18

Co-guide - <Name> (if any) Date:

Rajeev

Examiner - <Name> K.P. RAJEEV Date: 07 Dec 2018

Supratic Chakraborty

Member 1- <Name> SUPRATIC CHAKRABORTY Date: 07/12/18

Member 2- <Name> SATYAJIT HAZRA Date: 07/12/18

Final approval and acceptance of this thesis is contingent upon the candidate's submission of the final copies of the thesis to HBNI.

I/We hereby certify that I/we have read this thesis prepared under my/our direction and recommend that it may be accepted as fulfilling the thesis requirement.

Date: 07/12/18

Place: SINP Kolkata.

<Signature>
Co-guide (if applicable)

<Signature>
Guide

---

[1] This page is to be included only for final submission after successful completion of viva voce.

Version approved during the meeting of Standing Committee of Deans held during 29-30 Nov 2013

STATEMENT BY AUTHOR

This dissertation has been submitted in partial fulfilment of requirements for an advanced degree at Homi Bhabha National Institute (HBNI) and is deposited in the Library to be made available to borrowers under rules of the HBNI.

Brief quotations from this dissertation are allowable without special permission, provided that accurate acknowledgement of source is made. Requests for permission for extended quotation from or reproduction of this manuscript in whole or in part may be granted by the Competent Authority of HBNI when in his or her judgment the proposed use of the material is in the interests of scholarship. In all other instances, however, permission must be obtained from the author.

Barnamala Saha

BARNAMALA SAHA

DECLARATION

I, hereby declare that the investigation presented in the thesis has been carried out by me. The work is original and has not been submitted earlier as a whole or in part for a degree / diploma at this or any other Institution / University.

Barnamala Saha

BARNAMALA SAHA

List of Publications arising from the Thesis

Journal

Published:

1. An optimized alternative electron transfer process for electrochemical detection of glucose in blood serum using CdS nanostructures, **B. Saha**, S. K. Jana, S. Majumder, and S. Banerjee, published in Sensors and Actuators B: Chemical, Vol. 283 (2019) 116-123.

2. Selective growth of co-electrodeposited Mn_2O_3-Au spherical composite network towards enhanced non-enzymatic hydrogen peroxide sensing, **B. Saha**, S. K. Jana, S. Majumder, B. Satpati and S. Banerjee, published in Electrochimica Acta, 2015, Vol.174, Pages 853-863.

3. Structural and electrochemical analysis of novel co-electrodeposited Mn_2O_3-Au nanocomposite thin film, S. K. Jana*, **B. Saha***, S. Majumder, B. Satpati and S. Banerjee, published in Dalton Transactions, Vol. 44 (2015) Pages 9158-9169.

Conferences

1. 59th DAE Solid State Physics Symposium: presented poster on "Electrodeposited Nanostructured MnO_2 for Non-Enzymatic Hydrogen Peroxide Sensing", December 2014, Vellore Institute of Technology, Vellore

Barnamala Saha
BARNAMALA SAHA

For My Father,

for his incessant support and unconditional love

ACKNOWLEDGEMENTS

First of all, I extend my sincere gratitude to my supervisor, Prof. Sangam Banerjee for introducing me to the fascinating world of electrochemical materials science. I thank him for his numerous interesting questions, discussions, and suggestions. I am deeply grateful for his constant motivation which has resulted in my strong interest in various aspects of this field of research. A special thanks to Dr. Sourav Jana, for teaching me some of the basic experimental electrochemical techniques during my initial years of research.

The members of my doctoral committee, Prof. Satyaranjan Bhattacharyya, Prof. Supratic Chakraborty, Prof. Satyajit Hazra and Prof. Gayathri N. Banerjee, have been generous in reviewing my work and sharing their expertise.

I thank all my lab members (past and present) Bishnuda, Anuradhadi, Mayukhda, Koushikda, Sumit, Sampad, Montu, and Amrita for their co-operation in making the duration of research truly memorable.

I thank all the members of the Surface Physics and Materials Science division at the Saha Institute of Nuclear Physics for instilling vibrance and positivity within and outside the division. I am truly thankful to all my friends and batchmates especially, those who stood by me through thick and thin and have guided me in times of uncertainty.

I express my deepest gratitude to my grandparents, Late Prof. N. K. Saha and Late Smt. Indulekha Saha as they continue to motivate me through their principles, thoughts and blessings. I extend my heartfelt gratitude to my parents Prof. Shovan. K. Saha and Smt. Suparna Saha for their constant encouragement, undying patience and love. A big thanks to my brother Atulan, for he instilled scientific curiosity in me from a very young age. Thanks to my sister in law Shivnetra, for actively listening to all my queries and clarifying my innumerable doubts.

My stay in Kolkata wouldn’t have been as enjoyable had it not been for the love and support of the members of my extended family. I express my sincere gratitude and love to my maternal grandparents, Late Shri M. M. Chowdhury and Smt. Chhaya Chowdhury and all my uncles, aunts and cousins.

Finally, I express my deepest gratitude towards Prof. Udaya Narayan Singh and Smt. Suchita Singh (my in laws) for embracing me into their lives with love. I thank my husband, Rajarshi for being my pillar of strength, for his encouragement, and patience.

•

CONTENTS

SYNOPSIS

Studying electrochemical processes in the context of materials synthesis and applications has far reaching consequences. The versatility of this subject arises from the fundamental nature of charge transfer mechanisms associated with various natural and applied systems. Materials scientists equipped with the knowledge of basic and applied electrochemistry play key roles in optimizing various electrochemical systems and elucidating in-depth analysis and understanding of fundamental electrochemical processes.

The rich diversity in terms of the applications of electrochemistry is manifested in the form of electrochemical sensors, batteries, electrochemical capacitors, fuel cells, and photo-electrochemical systems. The electrode and electrolyte form the basis of any electrochemical system and exploring the mechanisms of the reactions occurring at their interface is of primary concern. Electrochemical materials scientists usually work towards achieving novel electrode and electrolyte materials for improving performances associated with electrochemical systems. These may include, obtaining electrode materials towards improved sensitivity and detection of an analyte, or optimizing electrode properties towards achieving improved performance of an electrochemical reaction which may be subsequently applied in a device.

Besides fundamental and applied electrochemistry, electrochemical processes are applicable as synthesis procedures as well. In this regard, electrodeposition and anodization are the two categories of processes which are commonly utilised [1]. Since these electrochemical techniques do not require very high-end sophisticated equipment and facilities, compared to those necessary in vacuum deposition, sputtering or many wet chemical synthesis procedures, they provide an alternate route for synthesis of low cost, large scale commercial applications. For instance, electrodeposited solder connections [2], synthesis of high moment magnetic material films [3], electrodeposited copper wiring on computer chips [4], nanofabrication and nano-pattering [5], and electroplating [6]. On the other hand, electrochemical anodization, which is a controlled oxidation process, is used to synthesize porous oxide films and templates by electrochemically etching metallic surfaces in the presence of an external current [7]. In recent times, electrochemical processes are being utilized for environmental applications such as waste water treatment and degradation of contaminants [8]. Electrochemical oxidation, involving direct and indirect anodic oxidation routes are being developed and applied for breaking up organic compounds.

This thesis is focused on three important aspects of electrochemical applications to materials and they are: electrodeposition, electrochemical sensing, and electrochemical capacitance. A novel, one step electrochemical co-deposition synthesis protocol has been formulated to incorporate gold-nanostructures in a matrix of manganese oxide film and the influence of incorporating gold nanostructures on the electrochemical sensing and capacitive properties have been studied. A thorough comparative analyses of structural, morphological, and electrochemical properties of co-electrodeposited Mn_2O_3-Au composite film and pristine Mn_2O_3 film has been performed. Furthermore, since, most electrochemical sensors rely on drop casted films of glassy carbon substrates, it is essential to evaluate the necessity of following a systematic approach in their electrochemical characterization. A brief description of each chapter is presented as follows:

Chapter 1: Introduction

This chapter is divided into two parts. The first provides a general introduction to some of the important aspects of electrochemical materials science including the basic processes of materials synthesis, electrochemical characterization techniques, and important applications. This includes a discussion on the prominent aspects of the Helmholtz layer, in the context of electrodeposition. The chapter cites several examples from the literature on various aspects of electrochemical materials science, such as the important electrochemical techniques and their uses, the various industrial applications and versatility of this subject. Examples of oxygen reduction reaction and ionic liquids have been illustrated. The recently developed applications of electrochemistry in environmental applications have been mentioned explaining the utility of oxidation and reduction processes in cleaning, reclamation, and contamination removal.

In the second part, the motivation and need to conduct this thesis work has been discussed. Herein, a discussion on enzyme based and non-enzymatic electrochemical biosensors has been presented. A comparison of their properties, advantages, and disadvantages has been discussed.

Subsequently, the need for research on electrochemical capacitors has been presented. An elaborate discussion on the application of supercapacitors, their advantages, and shortcomings have been cited from literature.

A thorough review of literature presents that the co-electrodeposited Mn_2O_3-Au composite system is the first of its kind, in terms of materials synthesis technique and electrochemical application.

Chapter 2: Experimental Techniques:

To understand electrochemical processes with clarity, it is important to understand the parts that make up an electrochemical system and the processes involved. The different electrochemical techniques that were utilised have been discussed in the second chapter. Cyclic voltammetery (CV), chronoamperometery (CA), and electrochemical impedance spectroscopy (EIS) are the most commonly used techniques [9]. Besides these, we have utilised the Mott-Schottky (M-S) analysis at electrode -electrolyte interface, for performing band structure analysis [10]. To gain a thorough understanding of the electrode-electrolyte system, especially, in cases of semiconductor electrodes, it is important to understand the nature of the semiconductor-electrolyte interface in terms of their flat band potential representation. In this context, understanding the relationship between the semiconductor and electrolyte energy levels is of crucial significance. The electrochemical synthesis and characterization experiments conducted in this work, were performed using a three-electrode cell on CHI 660C electrochemical workstation. The three-electrode system comprised of a reference electrode (RE), working electrode (WE), and counter electrode (CE) (also called the secondary or auxiliary electrode). This configuration offers the advantage of a steady electrical potential of the reference electrode during electrochemical measurements.

The working principle and underlying theory of the electrochemical techniques used, i.e., CV, CA, EIS, and M-S studies have been discussed elaborately.

The advanced materials characterization tools used in our study for morphological and structural analyses have also been discussed briefly. These include scanning and transmission electron microscopy, X-ray diffraction spectroscopy, Raman spectroscopy, X-ray photoelectron spectroscopy, and electron energy loss spectroscopy.

Chapter 3: Electrochemical co-deposition of Mn_2O_3-Au composite film:

Here, we discuss the electrochemical co-deposition synthesis protocol in detail. The synthesis was performed using CV. The experimental conditions have been discussed along with detailed materials characterization of the pristine and composite samples. The samples of pristine oxide film and co-electrodeposited composite films were synthesized for two sets of electrolyte molar concentrations. The electrolytes used were manganese acetate, sodium sulphate, and aurochloric acid. For the second case, the molar concentration of manganese acetate was made ten times.

Comparing the morphologies of the pristine and the composite sample, significant differences could be observed. To understand the mechanism behind the formation of the co-electrodeposited film, a systematic stepwise analysis was performed as shown in Fig.1. The entire cycle for deposition was divided into four parts corresponding to four voltage ranges: -1.2 to 0 V, -1.2 to 1 V, a complete cycle starting from -1.2 V, four rounds of the complete cycle and the electron micrograph of the samples was recorded at each stage. Based on the results of CV and electron microscopy, a schematic of the formation mechanism has been proposed. The electrochemical reactions accompanying the process have also been discussed.

The structural analyses of the pristine and composite samples were performed using advanced materials characterization tools. The results obtained have been discussed based on previously reported conclusions as cited in the chapter.

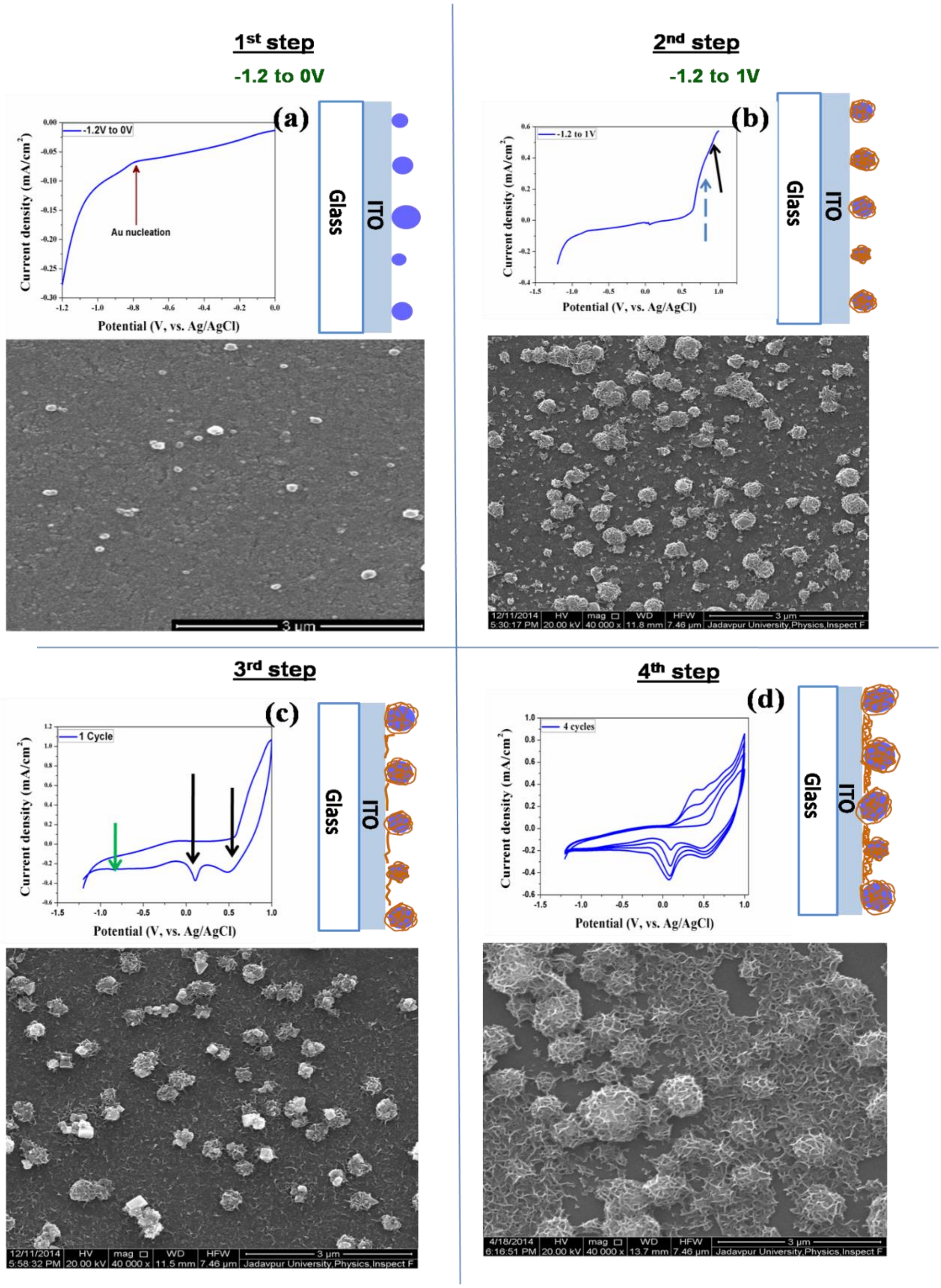

Fig.1 Schematic diagram depicting the co-electrodeposition process (a) step 1 CV between potentials -1.2 to 0 V, (b) step 2. CV between potentials -1.2 to 1 V, (c) step 3 one complete CV cycle between -1.2 and 1 V, (d) step 4 complete deposition for 4 CV cycles between -1.2 and 1 V.

This chapter constitutes portions of two of our peer-reviewed publications.

Chapter 4: Electrochemical hydrogen peroxide sensing with Mn_2O_3-Au composite

This chapter begins with an introduction on the need to design novel materials for electrochemical hydrogen peroxide sensing and gives an account of the types of materials used for this purpose. The properties of hydrogen peroxide, some of its typical characteristics, and uses have been discussed. The results of non-enzymatic electrochemical H_2O_2 sensing using Mn_2O_3-Au composite film have been presented. These include a comparative analysis using EIS, CV, and amperometric sensing of H_2O_2. The EIS spectra reveals a reduction in charge transfer resistance and surface resistance in the composite film. To verify the experimental results, the graphs were fitted with suitable equivalent circuits. The electrochemical sensing studies were conducted in an alkaline NaOH medium. The comparative cyclic voltammograms reveal an improvement in the electrochemical redox property of the composite structure. This could be correlated with the reduced charge transfer resistance which leads to an improvement in electro-catalytic properties. With the addition of increasing values of molar concentration of H_2O_2 to the NaOH background electrolyte, the redox current in the CV successively increased. To obtain the calibration between the molar concentration and corresponding redox current, amperometric I-t measurements were performed. In this technique, the working electrode was held at a fixed potential (corresponding to the maximum redox current), and increasing molar concentrations of H_2O_2 was added at regular intervals of time. The electrolyte was continuously stirred, in order to maintain homogeneity in the solution while adding H_2O_2. The sensitivity was obtained from the slope of the calibration curve. The effect of other common interfering species was analysed by both CV and amperometery techniques.

The results were compared with some of the previously reported electrochemical H_2O_2 sensing substrates such as, polycrystalline gold, nanoporous gold, MnO_2-graphene oxide composite, and few peroxidases. The results indicate a significantly low detection limit and comparable value of sensitivity. This chapter forms a part of one of our peer reviewed publications.

Chapter 5: Electrochemical charge storage properties of Mn_2O_3-Au film

In chapter 5, the classification of supercapacitors in terms of their charge storage mechanisms and the materials used in the fabrication of their electrodes have been discussed. Supercapacitor electrodes can be primarily categorized into three types, i.e. the electrochemical double layer capacitors (EDLCs), pseudocapacitors, and hybrid capacitors. EDLCs can store charge electrostatically, via a non-faradic process, which doesn't involve transfer of charge between the electrode and the electrolyte. Currently, the major focus of EDLC research is towards improving the energy performance and working range of temperature, where batteries cannot operate. Performance of EDLCs may also be adjusted by modifying the type of electrolyte used. Compared to EDLCs, that store charge electrostatically, pseudocapacitors store charge via faradaic processes which involves the transfer of charge between electrode and electrolyte [11]. When an external potential is applied to a pseudocapacitor, reduction and oxidation takes place on the electrode material, resulting in passage of charge across the double layer. This causes a faradaic current to pass through the supercapacitor cell. The faradaic processes involved in pseudocapacitors allow them to achieve greater specific capacitances and energy densities compared to EDLCs [12]. The materials commonly employed in fabrication of pseudocapacitors are metal oxides and conducting polymers. In the case of a hybrid system, a combination of both the features is seen, which comprises of an energy source of a battery-like electrode and power source of capacitor-like electrode in the same cell [13, 14]. By incorporating the appropriate electrode combination in hybrid systems, it is possible to increase the cell voltage, which in turn leads to an improvement in energy and power densities.

In the past, different combinations of electrode materials corresponding to both positive and negative electrodes in aqueous and inorganic electrolytes have been tested. However, in comparison with the EDLCs, hybrid devices exhibit higher energy density owing to the faradaic characteristics. This tends to reduce the cyclic stability, which resembles the features of an ordinary battery more than those of a good supercapacitor [15].

The fundamental parameters that decide the type of electrode materials which may be used in fabrication of supercapacitor electrodes are its capacitance and charge storage. Metal oxides present another alternative for fabrication of supercapacitor electrodes. The commonly used metal oxides are nickel oxide, ruthenium dioxide, manganese oxide, and iridium oxide [16]. In general, their low cost of production and use of milder electrolyte solutions make them a feasible alternative in supercapacitor fabrication [17].

The electrochemical capacitor market continues to grow and expand into a greater number of applications. Continuous research on electrode materials, cell assembly, and entire cell systems should yield electrochemical capacitors that exhibit the excellent properties of both conventional capacitors and batteries and might ultimately facilitate the emergence of new types of energy storage devices.

Recently, manganese oxide has attracted tremendous research interest owing to its unique physical and chemical properties along with a wide range of applications in ion exchange, catalysis, biosensor, energy storage, and molecular adsorption. Special attention is devoted to manganese dioxide as an electrode material for supercapacitors due to its low cost, excellent capacitive performance in aqueous electrolytes and environmental benignity [18]

Composite electrodes integrate different materials such as carbonaceous materials with either metal oxides or conducting polymer materials, which in turn offers both physical and chemical charge storage mechanisms in a single electrode. Manganese oxides, as an environmentally friendly material with various oxidation states, have been used for a long time as electrode materials for batteries. The pioneering work on the pseudocapacitive behavior of manganese oxide in an aqueous solution was published in 1999 by Lee and Goodenough. [19]. Following this, several studies were performed to establish the charge storage mechanism in manganese oxide electrodes. Pseudocapacitive (faradaic) reactions occurring on the surface and in the bulk of the electrode are the major components of charge storage mechanisms for manganese oxides. The surface faradaic reaction involves the surface adsorption of electrolyte cations (H^+, Li^+, Na^+ and K^+) on manganese oxide [20]. The bulk Faradaic reaction relies on the intercalation or deintercalation of electrolyte cations in the bulk of the manganese oxide. To improve the electrical conductivity of MnO_2 based electrode material, considerable research efforts have been invested towards the development of composite materials based on MnO_2 coupled with various conducting materials such as SnO_2 [21], conducting polymers [22, 23], graphene [24], and carbon nanotubes (CNTs) [25] etc.

Here, we discuss the capacitive behavior of the novel, co-electrodeposited Mn_2O_3-Au composite film using electrochemical characterization techniques. Our aim is to verify the electronic conductivity of the co-electrodeposited film after incorporation of metal nanostructure (Au). Furthermore, the effect of incorporation of metal nanostructure inside Mn_2O_3 film on its charge storage property has been investigated. Since, both electronic and ionic transport properties along with charge transfer reaction at the electrode/electrolyte interface are required for better understanding of electrochemical behavior, a detailed investigation of these aspects have been performed. Electronic and ionic properties of the active electrode materials were characterized by the M-S and EIS techniques and charge carrier concentrations in both the samples were obtained. CV on both samples was carried out to compare their capacitive behavior. Moreover, frequency behavior of both the samples was studied to understand the supercapacitance property of the samples for possible charge storage application.

EIS was conducted to understand the conductivity and charge transport in the electrode-electrolyte interface and mechanistic analysis of interfacial processes. Decrease of charge transfer resistance of Mn_2O_3-Au is ascribed to the large number of charge carriers in bulk of the same sample. The presence of these charge carriers is primarily due to the presence of Au inside the Mn_2O_3 which facilitate fastest electron transport and shortest ion-diffusion path inside the Mn_2O_3-Au. Another feature of the Nyquist plots is the straight line in the low frequency range (10 Hz to 10 mHz) which corresponds to the Warburg impedance [26] associated with diffusion of ions inside the porous electrode material. Also, this straight line makes an angle (called the phase angle) with Z_{real} axis. In our case, we observe that Warburg impedance is lower in Mn_2O_3-Au compared to Mn_2O_3. This result indicates that Mn_2O_3-Au shows better pseudocapacitive nature compared to Mn_2O_3. Moreover, increase in the phase angle which indicates capacitive nature of the active electrode material. Thus, the capacitive behavior of Mn_2O_3-Au is nearer to ideal capacitance than the Mn_2O_3. This can be investigated in detail by studying the frequency dependent phase angle plot (Bode plot) of both Mn_2O_3 and Mn_2O_3-Au sample. The Mn_2O_3-Au composite electrodes exhibited significantly higher charge storage capacity than the pristine Mn_2O_3. In our case, the following redox reaction in the composite film has been proposed :

$$Mn_2O_3 + (x+y)Na^+ + (xe_{ITO}^- + ye_{Au}^-) \longleftrightarrow Mn_2O_3[(x+y)Na]$$

The excellent performance of Mn_2O_3-Au electrode can be ascribed to the following reasons: (1) Urchin like gold nanostructure embedded in Mn_2O_3 increases the effective surface area as well as efficient ion intercalation/de-intercalation which results in improved charge storage capability of the composite sample compared to pristine Mn_2O_3; (2) the highly conducting metal nanoparticles provides an effective pathway for charge transport; and (3) the binder-free device fabrication enables a low interfacial resistance and fast electrochemical reaction rate. Moreover, frequency response analysis of Mn_2O_3-Au sample confirms superior charge storage property of the sample which can be used a supercapacitor eletrode.

Chapter 6: A systematic approach for electrochemical characterization of drop-casted films: CdS nanorods

Owing to the large number of drop-cast fabricated electrodes used in electrochemical sensing, it is important to perform a systematic evaluation of the experimental steps involved in its construction. This chapter fulfils that aspect based on hydrothermally synthesized CdS nanorods, using chitosan as the binder. A systematic protocol for optimized working electrode and electrolyte conditions accompanied by relevant electrochemical characterizations have been performed. All the steps of optimization are accompanied by relevant electrochemical characterizations such as electrocatalytic current and charge-transfer resistance. Based on the calibration plot, the values of sensitivity and limit of detection were calculated corresponding to the allowed working range of the electrode.

The research paper summarizing the results of this chapter, has been communicated.

Chapter 7 Conclusions and Future Outlook:

The conclusions derived from this work, can be summarized as follows:

1. It is possible to incorporate metallic nanostructures inside oxide thin film matrices, using one-step electrochemical co-deposition technique. This work proposes a novel strategy for fabricating Mn_2O_3-Au composite film by a one-step co-electrodeposition procedure. Based on systematic electrochemical and microscopic analysis, a schematic formation mechanism has been proposed. The electron microscopy results indicate that the morphology of the films are strongly dependent on the molar concentration of the electrolytes used.

   A detailed characterization using X-Ray diffraction spectroscopy, Raman Spectroscopy, X-Ray photoelectron spectroscopy, and electron energy loss spectroscopy indicate that structural nature of the oxide in the pristine and composite samples are identical.

2. The properties of the co-deposited film towards non-enzymatic, electrochemical H_2O_2 sensing was evaluated in an alkaline medium of NaOH. Electrochemical impedance spectroscopy results indicate a significant reduction in the interfacial charge transfer resistance, indicating enhanced electrocatalytic properties. This is in agreement with the results obtained by cyclic voltammetery. Amperometric I-t curves reveal good sensing performance upto 500μM of H_2O_2 concentration. The sensitivity and detection limits were obtained from the clibration curves, and the results have been compared with some of the previous reports on electrochemical H_2O_2 sensors.

3. The charge storage behaviour of the co-electrodeposited Mn_2O_3-Au film were evaluated using electrochemical techniques and the results were compared with pristine Mn_2O_3 film. Mott-Schottky studies were performed to understand the influence of the incorporated Au nanostructures on the flat band potential structure of the composite film and the charge carrier density was determined from that. A schematic depicting the electrochemical charge storage behavior of the composite film has been presented.

4. In the case of drop-casted films, it was found that electrochemical sensing behavior is highly dependent on electrode and electrolyte optimization techniques. The effect of binder quantity is a crucial factor in determining the response of electrochemical sensor electrodes.

In future, we wish to explore the possibility of incorporating more constituents in the composite films via co-electrodeposition. We feel this would increase the robustness of properties of composite films and allow their applicability in a wider range of systems.

References:

[1] M. Bigas, E. Cabruja, High density of electrodeposited Sn/Ag bumps for flip chip connection, Microelectron. Engg. 83 (2006) 399-403.

[2] X. Liu, G. Zangari, Electrodeposition of soft, high moment, Co-Fe-Ni thin films, J. Appl. Phys. 87 (2000)

[3] P. M. Vereecken, R. A. Binstead, H. Deligianni, and P. C. Andricacos, IBM J. Res. Dev., 49, 3 (2005).

[4] D. Natelson, Nanofabrication: Best of both worlds, Nat. Mat. 5 (2006) 853-854.

[5] K. M. Takahashi, Electroplating copper onto resistive barrier films, J. Electrochem. Soc.147 (2000) 1414.

[6] C. Lee, A. Kim, J. Kim, Electrochemically etched porous stainless steel for enhanced oil retention, Surf. Coat. Technol. 264 (2005) 127-131.

[7] Y. Feng, L. Yang, J. Liu, B. E. Logan, Electrochemical technologies for wastewater treatment and resource reclamation, Environ. Sci: Water Res. Technol.2 (2016) 800-831.

[8] Electroanalytical Methods: Guide to Experiments and Applications (2002)

[9] K. Gelderman, L. Lee, S. W. Donne, Flat-Band Potential of a Semiconductor: Using the Mott–Schottky Equation, J. Chem. Educ. 84 (2007) 685

[10] M. Vangari, T. Pryor, L. Jiang, Supercapacitors: Review of Materials and Fabrication Methods, J. Ener. Engg. 39 (2013)

[11] K. Fic, G. Lota, M. Mellera, E.Frackowiak, Novel insight into neutral medium as electrolyte for high-voltage supercapacitors, Energy Environ. Sci 5 (2012)

[12] A. Vlad, N. Singh, J. Rolland, S. Melinte, P. M. Ajayan, J.-F. Gohy, Hybrid supercapacitor-battery materials for fast electrochemical charge storage, Sci. Rep.4 (2014)

[13] F. Zhang, T. Zhang, X. Yang, L. Zhang, K.Leng, Y. Huanga, Y. Chen, A high-performance supercapacitor-battery hybrid energy storage device based on graphene-enhanced electrode materials with ultrahigh energy density, Energy Environ. Sci 6 (2013), 1623-1632.

[14] D. P. Dubal, O. Ayyad, V. Ruiz, P. G. Romero, Hybrid energy storage: the merging of battery and supercapacitor chemistries, Chem. Soc. Rev. 44 (2015) 1777-1790.

[15] Z. S. Iro, C. Subramani, S.S. Dash, A Brief Review on Electrode Materials for Supercapacitor, Int. J. Electrochem. Sci., 11 (2016) 10628 – 10643.

[16] C. J. Xu, C. G. Wei, B. H. Li, F. Y. Kang, Z. C. Guan, Charge storage mechanism of manganese dioxide for capacitor application: Effect of mild electrolytes containing alkaline and alkaline-earth metal cations, J. Power Sources 196 (2011) 7854-7859.

[17] J. G. Wang, Y. Yang, Z. H. Huang, F. Kang, Effect of temperature on the pseudocapacitive behaviour of freestanding MnO2@carbon nanofibers composite electrodes in mild electrolyte, J. Power Sources 224 (2013) 86-92.

[18] O. Giraldo, S. L. Brock, W. S. Willis, M. Marquez, S. L. Suib, Manganese Oxide Thin Films with Fast Ion-Exchange Properties, J. Am. Chem. Soc. 122 (2000) 9330–9331.

[19] H. Y.Lee,J. B.Goodenough, Supercapacitor Behavior with KCl Electrolyte, J. Solid State Chem.**144**, (1999)220–223.

[20] W. Wei, X. Cui, W. Chen, D. G. Ivey, Manganese oxide-based materials for electrochemical supercapacitor electrodes, Chem. Soc. Rev. 40 (2011) 1697-1721.

[21] Y. M. Dai, S. C. Tang, J. Q. Peng, S. K. Meng, MnO_2@SnO_2 core–shell heterostructured nanorods for supercapacitors, Mat. Lett. 130 (2014) 107-110.

[22] S. A. Hashmi, H. M. Upadhyaya, MnO_2-polypyrrole conducting polymer composite electrodes for electrochemical redox supercapacitors, Ionics 8 (2002) 272-277.

[23] Y. Shi, L. Peng, Y. Ding, Y. Zhaoa, G. Yu, Nanostructured conductive polymers for advanced energy storage, Chem. Soc. Rev. 44 (2015) 6684-6696.

[24] H. Lee, J. Kang, M. S. Cho, J.-B. Choic, Y. Lee, MnO_2/graphene composite electrodes for supercapacitors: the effect of graphene intercalation on capacitance, J. Mater. Chem. 21 (2011) 18215-18219.

[25] L. Li, Z. A. Hu, N. An, Y. Y. Yang, Z. M. Li, H. Y. Wu, Facile Synthesis of MnO2/CNTs Composite for Supercapacitor Electrodes with Long Cycle Stability, J. Phys. Chem. C 118 (2014) 22865-22872.

[26] Y. Tsividis, J. Milios, A detailed look at electrical equivalents of uniform electrochemical diffusion using nonuniform resistance–capacitance ladders, J. Electroanal. Chem.707 (2013) 156-16

List of Figures:

Chapter 1

Chapter 2

Chapter 3

Chapter 4

Chapter 5:

space charge capacitance (C_{sc}). Because both C_{sc} and double layer capacitance (C_{dl}, which is large than C_{sc}) are in series. So equivalent capacitance is C_{sc}. R_{ct}, W, and R_s are the charge transfer resistance, Warburg impedance and series resistance of the device respectively.

3. Fig. 5.3: Comparative study of Nyquist plot and of both Mn_2O_3 and Mn_2O_3-Au sample.
4. Fig. 5.4: Comparative study of frequency response on change in phase angle (Bode plot) of both Mn_2O_3 and Mn_2O_3-Au sample.
5. Fig. 5.5: Analysis on the (a) real part of the capacitance vs. the frequency and (b) imaginary part of the capacitance vs. the frequency of both Mn_2O_3 and Mn_2O_3-Au.
6. Fig. 5.6: CV profile of both pristine and composite sample at a fixed scan rate of 0.04 Vs-1
7. Fig. 5.7: Schematic representation of enhanced pseudocapacitive current of Mn_2O_3-Au.
8. Fig. 5.8: CV curves of Mn_2O_3-Au sample at different scan rate.

Chapter 6:

1. Fig. 6.1: (a) XRD plot of CdS nanorods, (b) SEM image of CdS nanorods with two different scales (i) 500 nm, (ii) 10 nm, elemental color mapping to show homogeneity at 10 µm scale of (iii) Cadmium and (iv) Sulfur, (c) EDX spectrum indicating the presence of Cadmium and Sulphur in the sample. (Au signal is due to the gold sputtering performed during SEM measurement.)
2. Fig. 6.2: (a) EIS spectra of bare ITO and CdS coated ITO along with equivalent Randle Circuit in the inset, (b) calibration plot between electro-reduction current density as a function of CdS weight, (c) EIS spectra for varying concentrations of chitosan solution and (d) the corresponding plot of charge transfer resistance as a function of chitosan concentration.
3. Fig. 6.3: (a) CV response CdS/ITO in presence of 20 µM H_2O_2 for increasing chitosan concentration for preparing drop casted electrode (b)CV response of CdS/ITO in presence of H_2O_2 for varying Electrolyte concentration.
4. Fig. 6.4: (a) CV response CdS/ITO in presence of 20 µM H_2O_2 for increasing chitosan concentration for preparing drop casted electrode (b)CV response of CdS/ITO in presence of H_2O_2 for varying Electrolyte concentration
5. Fig. 6.5: (a) CV plot of CdS/ITO for increasing concentration of H_2O_2 (b) CV plot of CdS/ITO for increasing values of scan rate (c) amperometric I-t response for increasing molar concentration of H_2O_2, (d, e, f) calibration plot corresponding to (a), (b), and (c), respectively.
6. Fig. 6.6: EIS spectra revealing optimization of molar concentration of GOx dissolved PBS for performing AET studies.
7. Fig. 6.7: (a) CV plot CdS/ITO in AET set-up for increasing molar concentration of glucose, (b) calibration plot corresponding to (a), (c) CV plot for increasing values of scan rate and (d) calibration plot corresponding to (c)

List of Tables:

Chapter 2:

Chapter 3:

Chapter 4:

Chapter 6:

CHAPTER 1

Chapter 1

Introduction

1.1 A bird's eye view of electrochemical materials science

Electrochemistry is a branch of physical chemistry that examines phenomena resulting from a combination and interdependence of chemical reactions and accompanying charge transfer processes. In the context of materials science, it has a prominent influence, as a tool for synthesis, characterization, and application of different kinds of nanomaterials, microstructures, and thin films which may be useful in the areas of diagnostics, agriculture, energy devices, and several others. The following paragraphs give a brief overview of these three aspects of electrochemical techniques.

1.1.1 Electrochemical processes for materials synthesis

For materials synthesis, the two commonly used electrochemical processes are electrochemical deposition and electrochemical anodization. Electrodeposition of metals and their oxides involve electric field driven single or multistep reduction and oxidation processes of cations and anions from an electrolyte mixture and coating them as a film onto a conductive substrate surface. Since, the chemical reaction around the area of the electrode takes place under the influence of an applied potential, it causes a rearrangement of the ions of the electrolyte near the electrode's surface resulting in the formation of an electric double layer, called the Helmholtz layer [1].

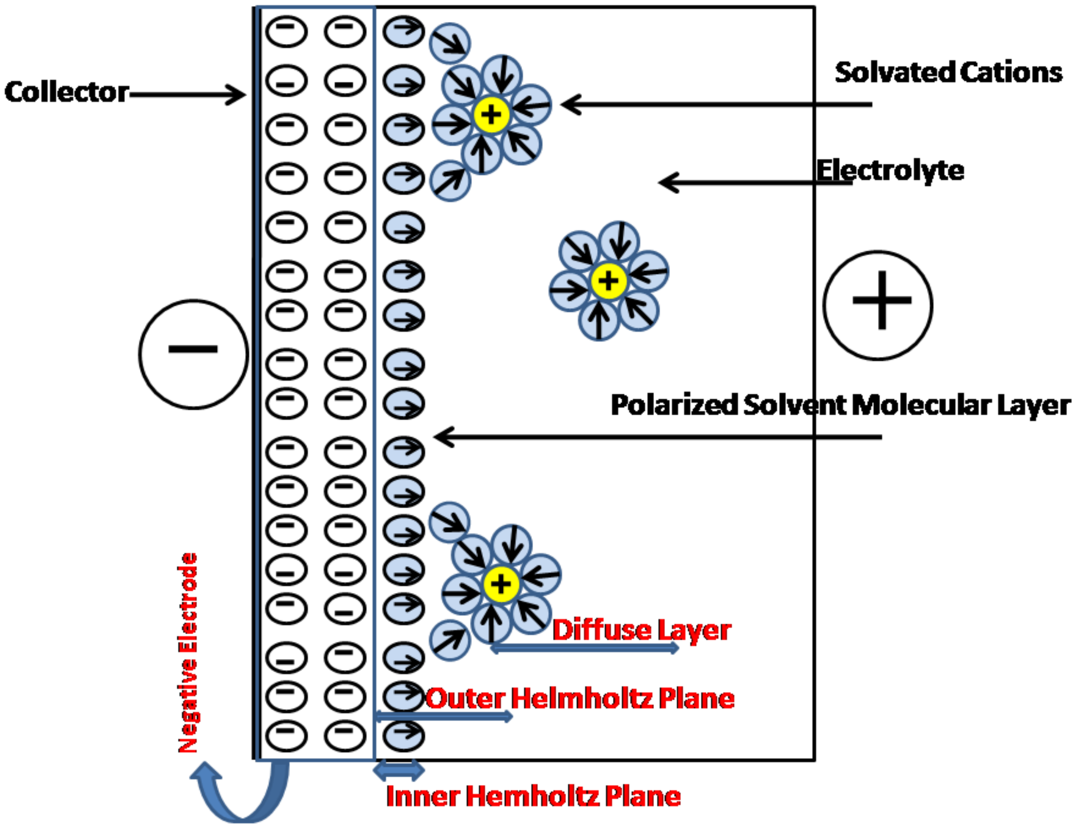

Fig.1.1: Schematic diagram depicting Helmholtz double layer of a negatively biased electrode

With the help of the schematic diagram of a negatively biased electrode and its adjacent Helmholtz layer, as depicted in Fig. 1.1, the electrodeposition of a metal can be understood in the following steps:

1. First, the hydrated metal ions in the electrolyte migrate towards the cathode under the influence of an applied current as well as by diffusion and convection processes.
2. Electron transfer takes place at the cathode surface as the hydrated metal ion enters the diffused double layer where the water molecules of the hydrated ions are aligned. Eventually, the metal ion enters the Helmholtz double layer, where it is deprived of its hydrate envelope.

3. Next, the dehydrated ion gets neutralized and adsorbed on the cathode surface. Subsequently, it migrates or diffuses to the point of growth on the cathode surface.

The properties of the electro-deposited film, such as its thickness, morphology, conductivity, and adhesiveness may be adjusted by regulating the duration of deposition, pH of electrolyte, bath temperature, and addition of external additives to the precursor bath. Electrodeposition is widely used as a synthesis method in microelectronics and offers several advantages such as low cost, reliability, and environmental friendliness as compared to other techniques, such as sputtering, chemical vapor deposition etc. In this regard, some of the technological innovations and breakthroughs which are worth mentioning are the electrodeposited solder connections [2] and magnetic materials [3]. The latter has made significant contributions to the implementation of technologies such as thin film inductive head and giant magneto-resistive read head [4].

Owing to the development of advanced techniques which facilitate manipulation of matter at a nano scale using processes, such as, the scanning tunnelling microscopy, electrodeposition can be applied at different length scales. A prominent example of this is the huge lengths of electrodeposited copper wires, accommodated on single wafer substrates [5].

On the other hand, anodization is an oxidation process which is used to synthesize porous oxide films and templates by electrochemically etching metallic surfaces in the presence of an external current [6]. The metal, undergoing oxidation is suitably biased in the electrochemical cell to facilitate electrochemical oxidation process. Aluminium and titanium are the two most common examples of metals where electrochemical anodization is applied to produce ordered oxide structures [7, 8]. In the recent years, it has been extended to other metallic substrates such as nickel [9], copper [10], manganese [11], and stainless steel [12]. The resultant morphology obtained from the controlled anodization of titanium sheets can be observed from the scanning electron microscopy image in Fig.1.2 [13].

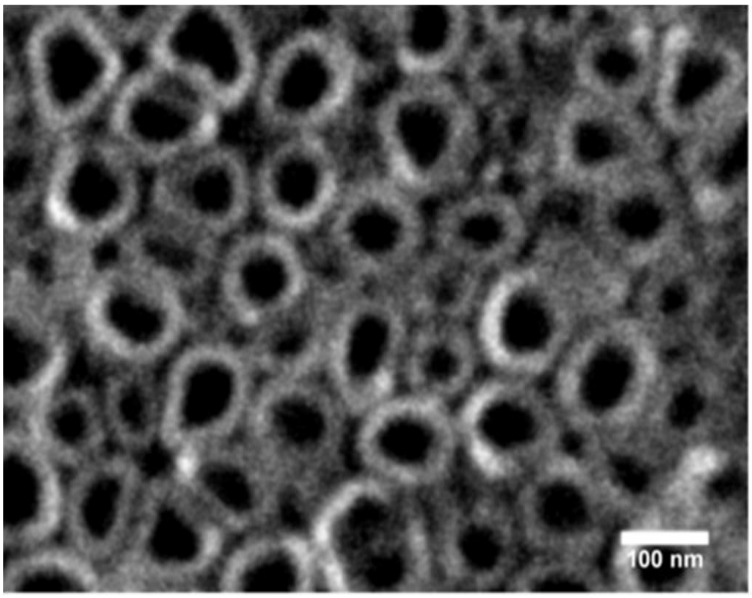

Fig.1.2: Scanning electron microscopy image of TiO_2 nanotubes formed by anodization [13]

By controlling the bias potential, electrolyte composition, and bath temperature, the porosity can be controlled, and the wall thickness of the nanotubes can be tuned. These materials are widely used as templates for electrochemical and solvo-thermal synthesis [14]. Owing to the nano-pattering, which results in a larger effective surface area, they are a popular choice as substrates for loading electro-catalytic materials for sensing applications [15].

1.1.2 Electrochemical techniques for materials characterization

Electrochemical characterization methods can be applied as standalone techniques for materials characterization for evaluating various surface and charge transport properties at the electrode-electrolyte interface. Amongst them, cyclic voltammetry (CV), chronoamperometry (CA), and electrochemical impedance spectroscopy (EIS) are the most commonly used. CV and CA techniques are applicable for materials synthesis (electrodeposition) as well as characterization and can be subsequently utilised in device fabrication, such as for sensors, batteries, and electrochemical capacitors.

Apart from its application in synthesis processes, CV is a versatile tool, which allows the identification of underlying mechanisms of redox systems and may be applied for investigating various transport properties of electroactive species in a solution. Oxidation and reduction processes occurring at the electrode surface, often involve complex steps comprising of adsorption, oxidation/reduction, and desorption phenomena. In this method, an applied voltage at the working electrode is scanned at a constant rate, once or repeatedly between two values and the resulting current is measured. A graphical plot between the applied voltage and measured current is obtained and used for further analyses. This technique is the first electrochemical experiment performed to characterize an electrode material for any application involving electrochemical reactions at electrode surfaces. It can be used to obtain information on thermodynamics of redox processes, kinetics of heterogeneous electron transfer reactions, coupled chemical reactions, and adsorption processes. As a detection technique as well, CV offers great potential in a variety of applications. For example, in the presence of a supporting electrolyte or buffer solution, CV may be performed upon the addition of a target species which is of interest for detection. In a situation, where, the species participates in an electrochemical reaction with the working electrode under study, a noticeable change in the voltammogram may be observed, which could be subsequently calibrated as a function of the concentration of the target species. This is a very simplistic way of understanding electrochemical detection using CV, and more detailed explanations will be provided in the subsequent chapters. There are other variations of voltammetry based on the way in which the external bias is applied, namely, square wave voltammetry, differential pulse voltammetry etc. Lately, another extension of the CV technique which has drawn considerable amount of attention is the fast scan cyclic voltammetry. As the name suggests, the rate at which the applied voltage is swept is very high, typically, of the order of $1 \text{ X } 10^6$ Volts/sec leading to a rapid acquisition of the voltammogram within a few milliseconds [16]. This technique has grown to become a very popular method for detection of neurotransmitters, hormones, and metabolites in biological systems [17].

The CA technique is a constant potential method, which may be applied for the synthesis and detection of nanomaterials. A fixed bias potential is applied at the electrode, and the current is monitored as a function of time. By choosing the appropriate electrolyte, a suitable potential and electrode substrate, deposition of nanomaterials and thin films of oxides, metals, and chalcogenides can be performed. In the case of a stationary electrode, for a given potential in an unstirred solution, mass transport towards the electrode is solely governed by diffusion and the current-time dependence reflects the change in the concentration gradient of the electrolyte species in the vicinity of the electrode surface. For macro-electrodes, this technique is commonly used for determination of diffusion coefficients corresponding to a specific electro-active surface area [18]. Changes in the value of current with the addition of target species may be observed owing to a certain electrochemical reaction occurring at a specific applied potential. This suggests the usefulness of CA as a detection technique. A variation of CA is the pulsed CA which offers the advantage of overcoming electrode fouling during any detection application and is particularly relevant for detecting organic molecules, wherein, the measurement potential is maintained for a short time (measurement pulse) followed by the electrode cleaning and conditioning pulse, resulting in the in-situ cleaning and reactivation of the electrode surface during the process of detection. For example, with the application of this technique for pentachlorophenol detection at carbon nanotube working electrode as an alternate to CA, an improvement in sensitivity by a hundred orders is obtained [19].

The third important electrochemical technique is the EIS. Herein, the electrode under study is perturbed with a small amplitude sinusoidal potential and the resulting impedance is measured. This process is performed over a range of frequencies which are incremented by a fixed amount, and simultaneously, the corresponding impedances are recorded. As the frequency is scanned from high to low values, the resulting spectra reveals interesting details about the charge transfer processes and electrochemical reactions taking place at the interface of electrode and electrolyte. This is an extremely useful technique for characterizing working electrode surfaces which are used in the fabrication of biosensors, where, the appropriate value of charge transfer resistance at the interface of electrode and electrolyte is crucial for ensuring good electrocatalytic property. The charge transfer resistance corresponds to the resistance across the electrode/electrolyte interface arising from the faradaic reactions. The spectra can be divided into separate regions in accordance with the frequency values, revealing the resistive (high frequency) and capacitive (low frequency) behaviour of the electrode-electrolyte interface. Hence, this method is useful for comparing capacitive properties of different materials loaded onto current collector electrodes. This application is of significant relevance in our work along with the charge transfer impedance studies. The use of EIS for charge transfer determination and study of capacitive properties have been discussed elaborately in the following chapters. Additionally, this technique is indispensable for materials analysis in corrosion and solid-state laboratories. Due to the barrier properties of coatings against corrosive species, they are often used to protect metals against corrosion. This is because they create a high electrical resistance across the coating thickness. With the passage of time, the interconnecting network of pores, between the epoxy matrices tend to become saturated with moisture and salts, thereby, exposing the underlying metal substrate into its adjacent corrosive environment. Corrosion scientists often correlate this with a term called the ‘polarization resistance’ which can be understood as the associated rate of corrosion process [20]. The main advantage of using EIS in corrosion monitoring is that it allows a quantitative determination of coating properties without affecting the coating and its performance. It facilitates the detection of changes at much smaller fractions of exposure time as compared to the conventional mechanical or visual methods [21]. In fuel cell diagnostics, EIS proves to be a powerful and cost-effective tool for characterizing their limitations and thereby, suggesting ways for improving their performance.

The impedance across the electrode-electrolyte interface can be modelled with suitable equivalent circuit networks to simulate the physiochemical processes occurring within the fuel cell. A network of resistors, capacitors, and inductors, may be used to obtain meaningful information about the sources of these impedances. Since, these processes, namely electronic and ionic transport, transport of gas and solid phase reactants and heterogeneous reactions have different characteristic time constants, their characteristic features are reflected at different AC frequencies. Consequently, when EIS is conducted over a broad range of frequencies, the impedance associated with the various processes can be identified. A detailed discussion on the theoretical and mathematical aspects of EIS has been provided in Chapter 2.

1.1.3. Application of electrochemical techniques in the context of devices

Any electrochemical device is essentially made up of two components, the electrode, and the electrolyte. The role of materials scientists is crucial for researching on ways to improve upon the properties and shortcomings of these two components and design novel materials with improved characteristics as per the requirement of the system. Designing materials for application as electrode and electrolyte materials for electrochemical sensors, working electrodes for batteries, super-capacitors, and fuel cells are of primary interest. On one hand, electrochemical sensors rely on the study of oxidation or reduction of the specific analyte under consideration along with a corresponding calibration of concentration vs. current or voltage or impedance and on the other, energy devices (batteries, supercapacitors, fuel cells), rely on various mechanisms of charge generation and storage by means of electrochemical reactions occurring on the electrode. To illustrate these aspects better, we consider the examples of two widely studied topics i.e. oxygen reduction reaction (ORR) and ionic liquid.

The ORR is a fundamental reaction related to various disciplines such as energy conversion, materials' dissolution, or biological application [22]. So far, platinum based electro-catalysts are the most commonly used cathode materials for ORR. Recently explored alternatives include carbon materials that are doped with a variety of non-precious metal atoms. For instance, Guo et.al studied model graphite catalysts to understand the role of nitrogen doping and elucidate the nature of active catalytic sites [23]. Bimetallic catalysts, particularly, graphene supported Pd-Ru catalyst has been recognized to be one of the most promising materials for fuel cell applications [24]. Materials having different kinds of morphologies, such as vertically aligned nanotubes, bundles, and materials of cylindrical morphology, have been of great interest due to their unique mechanical properties and potential application in a wide range of electrochemical applications [25]. One of the most commonly used electrode materials for modifying glassy carbon working electrode surfaces, are, the doped and undoped multi walled carbon nanotubes which show great promise towards high electrocatalytic activity for oxygen reduction in alkaline medium [26]. Extensive studies have shown that cost-effective electrode materials such as TiO_2, ZrO_2 and TaO_2 are promising candidates as active cathode catalyst for polymer electrolyte fuel cells [27]. Utilisation of modified electrodes (Carbon, metal, metal oxides, conducting polymers, and composites), may significantly enhance the working electrode's catalytic activity towards ORR in fuel cells' application.

In the context of materials research on electrolytes, ionic liquids are one of the most prominent examples. An ionic liquid is defined as a salt whose melting point is lower than the boiling point of water and are known by several different names, like, neoteric solvents, designer solvents, ionic fluids, and molten salts. Amongst these, structurally, most of them are composed of organic cation and inorganic anion entities. Dupont et al. extensively reviewed the application of ionic liquids as a catalytic phase in various organometallic reactions [28]. Catalytic applications of metal nanoparticles have been explored in ionic liquid media by

Migowski and Dupont [29, 30]. Ionic liquids find extensive applications in enhancing supercapacitance properties, as exemplified in a recent report by Mourad et.al [31].

Besides finding applications in devices, such as sensors, batteries, capacitors, and fuel cells, electrochemical processes have gained increasing interest in environmental applications like wastewater treatment and degradation of contaminants [32]. In this context, refractory carboxylic acids and perfluorocarboxylic acids have received significant attention in the past. Some of the primary advantages of electrochemical processes include operation at ambient pressure and temperature, their capability to adjust to variations in the influent composition and flow rate, easy adaptability to various applications, and efficient synchronization with other technologies. Electrochemical oxidation is considered as being one of the most powerful tools for breaking up organic compounds. The three major electrochemical reduction processes, namely, electrodeposition, cathodic electrochemical dechlorination, and electrochemical denitrification, are the commonly available technologies for removal and reclamation of pollutants from wastewater. In comparison with the conventionally used coagulation process, the amounts of chemicals required is small, and the amount of sludge produced is less. Sonochemical technology shows great promise and potential as an approach for improving electrochemical processes by activating the electrode surface and subsequently enhancing the mass transfer efficiency. Under present circumstances, more experimentation and analyses are required to get a better understanding of the degradation processes that occur within such hybrid electrochemical technologies.

To summarise, electrochemical materials science is essentially a bridge between electrochemical processes and materials science. Primarily based on electrochemical oxidation and reduction processes, this field of study encompasses a wide variety of topics starting from methods for fabrication of thin films, designing electrode and electrolyte materials for various applications and utilizing electrochemical processes for environmental applications. The success in electrochemical technology may be attributed to the continued design and development of newer materials with the aim to meet the needs of the modern society. These include, designing materials for electrochemical power sources such as rechargeable lithium ion batteries, solid oxide fuel cells, and supercapacitors. Furthermore, development of innovative synthesis and processing techniques to achieve unique compositions and microstructures offer superior performance in energy storage and conversion technologies. Some of the other important areas of study include the development of membranes for gas separation, fabrication and study of biosensors, electrochemical DNA and immunosensor arrays. Corrosion engineering of metal alloys, ceramics, and photoelectrochemical processes at semiconductors are equally relevant and challenging topics pertaining to electrochemical processes in materials science.

1.2 Motivation

The field of biosensor research started with the introduction of the first generation of glucose oxidase biosensor in 1962. Designed for a specific detection purpose, biosensors are highly selective due to a specific interaction of compounds that display a good degree of binding affinity with certain molecules. This results in the possibility of tailoring the surface of sensor substrate with the desired molecule through immobilization of biological recognition elements. The commonly used recognition elements in biosensors' fabrication are enzymes, nucleic acids, antibodies, whole cells, and receptors [33]. Out of these, enzymes are the most frequently used. Fabrication of electrochemical sensors for hydrogen peroxide (H_2O_2), glucose, cholesterol, and uric acid using their corresponding oxidase enzymes i.e. horseradish peroxidase, glucose oxidase, cholesterol oxidase, and uricase have been studied widely. In the current context of medical applications, there are a growing number of biosensors being used as diagnostic tools in point of care testing. Among these, a variety of instruments referred to as biosensors, can be found in research labs around the world. Some of the inherent advantages of electrochemical biosensors include, their operational robustness, easy miniaturization while fabrication, and excellent obtainable detection limits utilizing very small volumes of analyte. In electrochemical bio-sensing, the electrical properties of a system are measured for extracting information about biological systems which occurs via an electrochemical process. Hence, the bio-electrochemical component under study serves as the main transduction element. Usually, in bio-electrochemistry, the reaction under investigation would generate one of the following three possible parameters, i.e. a measurable current (amperometric), a measurable potential or a certain charge accumulation (potentiometric) between the electrodes. Since reactions are generally detected only in the vicinity of the electrode surface, the electrodes themselves play a crucial role in the performance of biosensors. For ensuring operational stability, the electrodes should be conductive and chemically stable. Materials which are commonly used in electrode fabrication, are, platinum, gold, carbon, and silicon compounds depending on the analyte under investigation. Despite the numerous advantages of enzyme based electrochemical sensing, it suffers from some intrinsic drawbacks associated with complicated steps of enzyme purification and immobilization, high cost of enzymes, and often suffer from hindrance in direct electron transfer due to the presence of the thick protein shell in which the redox active centre is embedded. Furthermore, owing to the oxygen dependency of first generation enzymatic biosensors, they are unsuitable for practical and reliable analytical use [34]. To ensure the stability of the immobilized enzyme on the working electrode surface and mediator electrodes a considerable amount of attention is required in view of the elaborate fabrication processes of electro-polymerisation and covalent cross linking of a pre-treated surface. This may result in higher costs of fabrication, lower reproducibility of performance, and short-term stability.

On the other hand, the possible usage of non-enzymatic electrodes offers great potential in terms of low cost and good stability under temperature and pH variation and enhanced electrochemical sensing properties which can be achieved by the rational designing and utilization of nanomaterials for electrode fabrication. Additionally, the need to come up with simple low cost materials and synthesis procedures which may be applied for a commercial scale synthesis of working electrodes is extremely crucial. In our work, we explore these aspects of enzyme based sensing of glucose and enzyme-less sensing of hydrogen peroxide using two kinds of nanomaterials i.e. manganese oxide and cadmium sulfide. Particularly, the non-enzymatic electrochemical sensing properties of a co-electrodeposited Mn_2O_3-Au composite was investigated thoroughly by us as described in this thesis. In most cases, nanomaterials are synthesized by solvothermal, wet chemical or other procedures and working electrodes are prepared by drop casting on conducting substrates for performing electrochemical characterizations. Consequently, depending on the amount used, utilising binders for drop casting procedure may hamper the electrocatalytic property of the film. This suggests the need to evaluate the optimization routes for drop casted working electrode and electrolyte solutions in order to obtain the best performance.

In this thesis, I have also addressed electrochemical charge storage studies. In the current scenario of world energy consumption, energy storage is a key component for creating sustainable energy systems. Even though, current technologies, such as solar photovoltaics and wind turbines, can generate energy in a sustainable and environmentally friendly manner, their intermittent nature prevents them from becoming a primary energy source. Electrochemical energy storage technologies have the potential to suggest solutions for overcoming the intermittency problem of renewable energy sources by storing the generated intermittent energy and subsequently making it accessible as per demand.

Based on the mechanism of electrical energy storage, these technologies can be classified into two groups. In the first case, electricity is stored directly in the form of electrical charges. The examples belonging to this category are capacitors or supercapacitors that are highly efficient (almost 100%), however, suffer from low energy density and discharge rapidly within a short period of time. For application purposes, these technologies are extremely useful in power management (e.g., in frequency regulation). Perhaps, the largest group of technologies for stationary applications are the electrochemical storage technologies especially, batteries, that can efficiently store electricity in chemicals and reversibly release it as per the energy requirement.

The charge and discharge times of super-capacitors are comparable to those of ordinary capacitors and it is possible to obtain high charge and discharge currents due to their low internal resistance. Usually, batteries require several hours to reach a fully charged state, while super-capacitors can be brought to the same charged state within a few minutes. The specific power of a battery or a super-capacitor is used to compare different technologies in terms of maximum power output divided by total mass of the device. Super-capacitors possess specific power values 5 to 10 times greater than that of batteries [35]. For instance, in the case of Li-ion batteries, specific power is of the order of 1 – 3 kW/kg, while that of a typical super-capacitor is around 10 kW/kg [36]. This property can be especially useful in applications that require rapid and reliable bursts of energy release.

Another major point of difference between super-capacitors and batteries is that it can be charged and discharged through millions of cycles. This makes super-capacitors very useful in applications where frequent storage and release of energy is required.

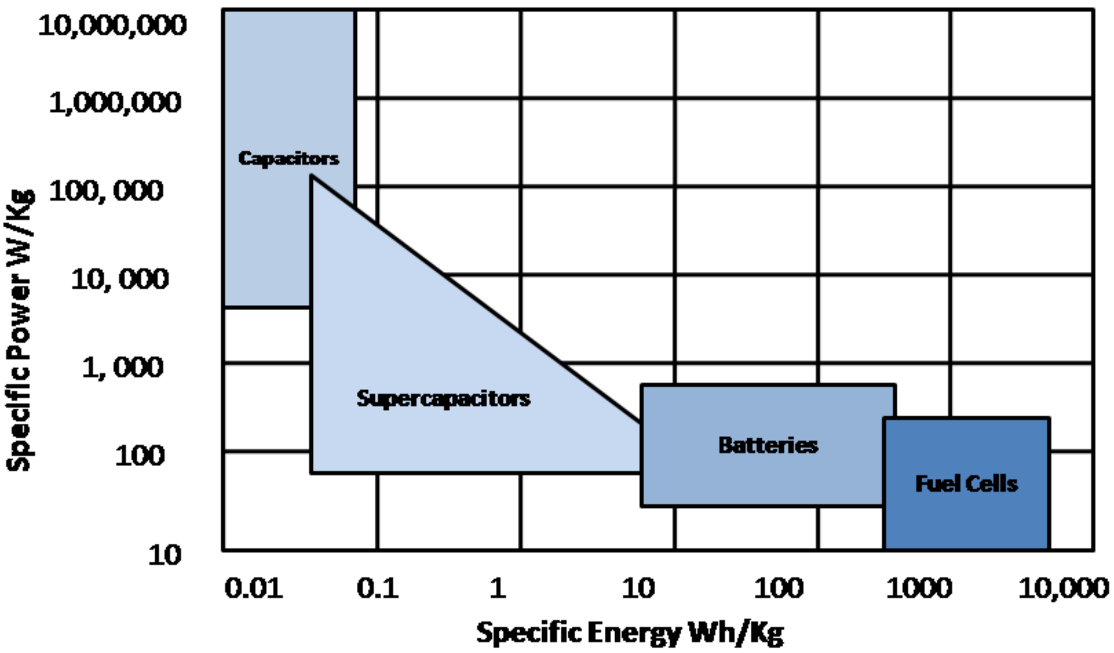

Fig.1.3: Schematic of the Ragone Plot depicting various energy storage devices

Fig.1.3 depicts the schematic of a Ragone plot indicating the position of supercapacitors in terms of their specific power and specific energy values as compared to other energy storage devices.

Owing to their infinite lifespan, super-capacitors are most commonly used in backup power applications and are electronic devices that have an unusually high energy density when compared to common capacitors. A common capacitor is an electrical device that can deliver energy in the electric field between a pair of conductors or plates. Capacitors and batteries are comparable in the sense, that they can both deliver electrical energy, however, batteries in addition can also produce energy.

Other areas which can find possible usage of super-capacitors are in low-power applications, where a high capacity is not essential, but a high life cycle or quick recharging is important. Electrochemical capacitors, ultracapacitors, electrochemical double layer capacitors are technologically relevant owing to their apparent simplicity and properties which compliment those of batteries.

As an energy-efficient alternative, super-capacitors have limitations in both cost and performance. In view of the current research achievements, super-capacitors cannot be substituted for the battery technology. However, they can be applied as a supplement for temporary power outage by providing instantaneous current as per requirement, thereby reducing battery current. Despite the limitation of super-capacitors in large scale commercial applications, it is essential to carry out advanced research in these areas to improve our understanding thereby developing a broad and deep knowledge base.

Most studies and research papers pertaining to super-capacitor research are focussed on improving electrode properties, such as, specific capacitance, cyclic stability, and power density. These issues are addressed by optimising the mass loading on current collectors [37], designing advanced nanomaterials like composites, core-shell nanostructures, utilising efficient current collector electrodes such as free-standing graphene foam [38], multi-walled carbon nanotubes [39]. A variety of oxide nanomaterials displaying excellent pseudocapacitive properties have recently attracted a great deal of enthusiasm [40]. Most of these studies have discussed different synthesis and design protocols such as combining oxide materials with carbonaceous materials [41], fabricating mesoporous materials [42], and engineering nanomaterial morphologies to increase effective surface area [43]. These aspects collectively aim towards improvement of electronic conductivity, increase of mass loading of active materials, and enhancement of the surface area of working electrodes in contact with the electrolyte, thereby improving specific capacitance values.

However, despite these previous reports, there hasn’t been significant research on investigating the role of metal nanostructures embedded in oxide film matrix on its supercapacitance property. Even though, in a recent work by Sharma et.al [44], the supercapacitance property of metal doped ceria decorated aminated graphene has been discussed, an exact cause for this observation based on electrochemical analyses has not been proposed. Nano-porous gold combined with manganese oxide display high specific capacitance, close to the theoretical value as suggested by Lang et.al. [45]. Furthermore, in most super-capacitor working electrodes, electroactive materials are prepared by chemical, solvo-thermal, sol-gel and other routes, and are subsequently loaded on current collector electrodes using polymeric binders.

In our work, we fabricate a manganese oxide-gold composite pseudocapacitive electrode by co-electrodeposition on indium tin oxide coated glass (ITO) substrates. Advanced characterization techniques were applied to study the material properties thoroughly, and detailed electrochemical studies were conducted to understand the role of the incorporated gold nanostructures on the enhancement of supercapacitance property. A brief literature survey of the oxide materials used for supercapacitor fabrication has been presented in Chapter 5.

The motivation for this thesis was to understand few crucial aspects of electrochemical sensing and supercapacitance such as improving these electrochemical properties by incorporating gold nanostructures. It is imaginable, that, the low values of electronic conductivity are a hindrance in obtaining good electrochemical sensing and supercapacitance behaviour. Manganese oxide being a low cost, abundantly available, inorganic oxide material that may exist in several oxidation states, was chosen as the material for our study. Owing to its above-mentioned advantages, especially being inexpensive, manganese oxide could be a suitable material for large scale, commercial fabrication of working electrodes which may find suitable application in electrochemical sensing and supercapacitance. A novel co-electrodeposition technique was formulated, to incorporate, gold nanostructures in manganese oxide film. In order to understand the mechanism of formation and suggest a possible route of synthesis, a series of systematic studies based on electrochemical and electron microscopy techniques were conducted.

To summarise, utilisation of low cost, easily available inorganic materials along with an approach to improve their electrochemical properties by incorporation metal nanostructures, such as, gold was the main aim for this thesis. Additionally, this work also aims to elucidate some crucial aspects of drop casted working electrodes, such as the role of binder concentration, and an investigation of enzyme dissolved buffer on the electrochemical sensing performance.

CHAPTER 2

Chapter 2
Experimental Methods

2.1 Introduction:

In this chapter, some of the basic concepts and theoretical aspects of the experimental techniques used in this work have been addressed. These include an understanding of the parts that make up an electrochemical experimental set up, which are the electrochemical cell, and the potentiostatic arrangements using which electrochemical experiments were conducted. A potentiostat is used to keep a working electrode (WE) at a desired potential with respect to a reference electrode (RE). This is achieved by passing current from the WE to the counter electrode (CE). From the perspective of electronics, potentiostat is a specific kind of feed-back amplifier.

The schematic representation of the arrangement of a three-electrode electrochemical cell is shown in Fig.1. We discuss the importance of using a three-electrode electrochemical cell while highlighting its differences from its two-electrode counterpart.

Additionally, some more theoretical aspects of the advanced materials characterization techniques used for sample characterizations, such as scanning and transmission electron microscopy methods, electron energy loss spectroscopy, X ray diffraction, X ray photoelectron spectroscopy methods and Raman spectroscopy techniques have been discussed.

2.2 *Basics of Voltammetry and three electrode cell:*

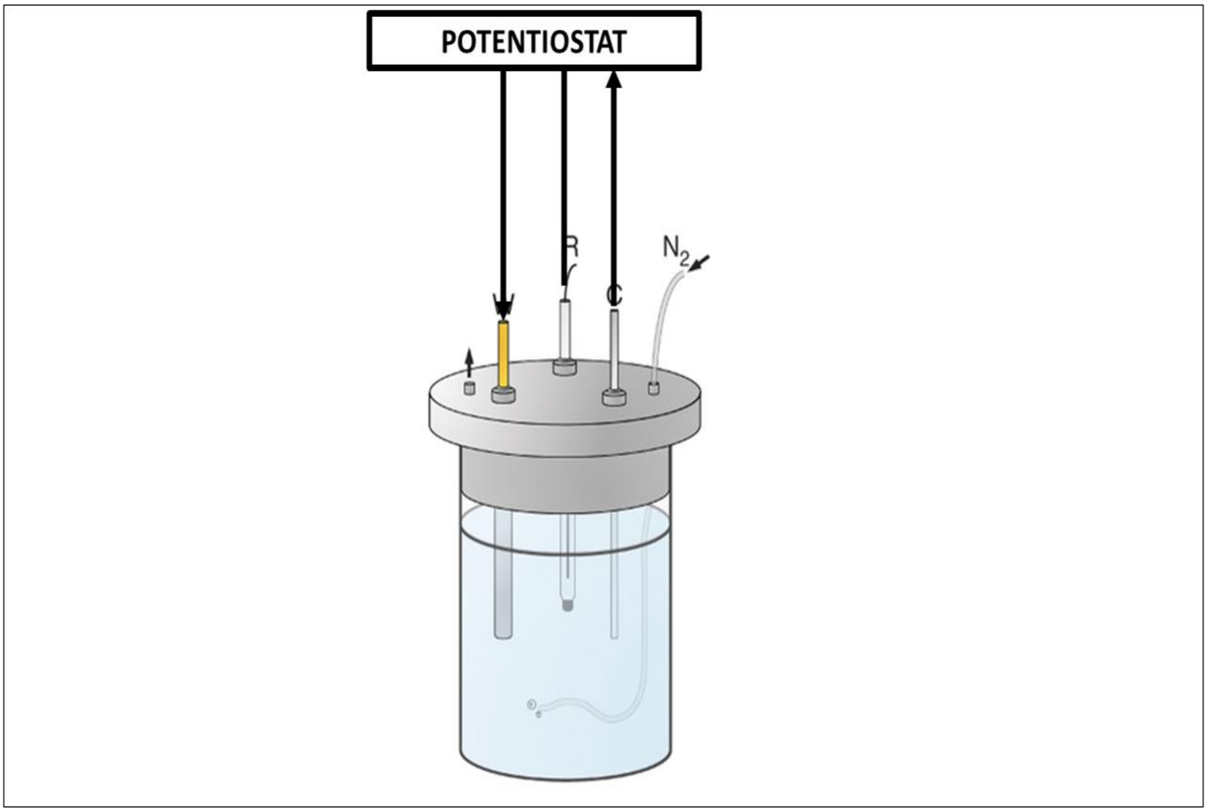

Fig.2.1: Schematic representation of a three-electrode electrochemical cell depicting the working electrode, counter electrode, and reference electrode as WE, CE, and RE respectively.

Fig.2.1 represents the schematic of a three-electrode electrochemical cell with the WE, CE, and RE labelled on the diagram. A similar set up was used for all our electrochemical synthesis and analyses processes.

Voltammetry techniques are used in analytical chemistry and in various other industrial processes. It derives information about an analyte by measuring the current with the variation of applied potential. In voltammetry experiments, the half-cell reactivity of the analyte is investigated. The graphical representation of the curve I = f (E) are called voltammograms. The potential can be varied either in a step by step or in a continuous manner and the resulting value of current is measured as the dependent variable. A minimum of two electrodes are required to perform such experiments. To the first, i.e. the working electrode, a desired potential is applied which would facilitate the transfer of charge to and from the analyte/electrolyte. The second electrode must have a known potential using which the potential of the working electrode can be determined. Furthermore, it must be able to balance the charge added or removed by the working electrode. In this set up, it is difficult to maintain a constant potential while passing current to counter the redox events at the working electrode. Hence, the supply of electrons for providing a reference potential, is performed by a separate electrode. The RE is the half cell with a known reduction potential. Its only purpose is to act as a reference in measuring and controlling the working electrode's potential and at no point it passes any current. The auxiliary electrode/CE passes the current thereby, balancing the observed current at the working electrode. These three electrodes, namely, the working, the auxillary, and the reference constitute the three-electrode system. In practice, it is important to have a working electrode with known dimensions and surface characteristics. Due to this, it is a common practice to clean and polish the working electrodes regularly. The auxiliary electrode should be stable in the bulk of the analyte solution and should be a good conductor. The reference electrode has a stable and well-known electrode potential. The stability of the electrode can be maintained by employing a redox system in contact with a buffered concentration of each participants of the redox reaction.

The techniques used in the electrochemical and materials characterizations have been discussed in the following pages. A basic understanding of the electrochemical techniques used has been elaborated [46, 47, 48].

2.2.1 Cyclic Voltammetry:

In order to obtain preliminary information about any new electrode/electrolyte system, cyclic voltammetry (CV) is most crucial among the available characterization techniques. With this technique, it is possible to derive information about the type of reaction observed in the system and the potentials at which they occur. The three-electrode configuration is the most widely used because the electrical potential of reference does not change during the measurement. A standard CV experiment involves the measurement of current flowing through the WE with a triangular waveform of voltage perturbation. The applied potential is measured against the RE, while the CE closes the electrical circuit for the current to flow. The experiments are performed using a potentiostat that effectively controls the voltage between the RE and WE, while measuring the current through the CE. Typically, the electrolyte is added to the background solution to ensure sufficient conductivity. The combination of the solvent, electrolyte and specific working electrode material dictates the range of the potential to be applied.

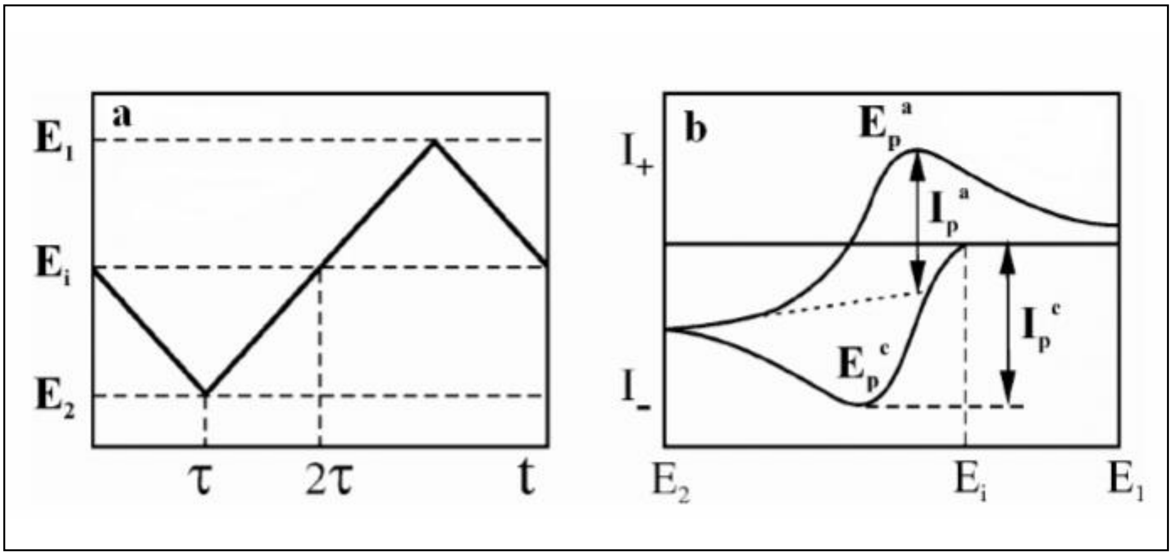

Fig.2.2: Schematic representation of applied voltage (a) and corresponding cyclic voltammogram for a reversible system

Fig.2.2 depicts a schematic plot of the applied voltage and its corresponding voltammogram for a typical CV measurement. This voltammorgram is representative of a reversible electrochemical system. Briefly, this method can be introduced as a voltage reversal technique, which involves sweeping the electrode potential between two limits at a known sweep rate. Initially, the working electrode is held at the potential, E_i, at which no electrochemical reaction occurs. Subsequently, the potential is swept linearly at a rate ν between two limiting values E_1 and E_2 (Fig.2.2) at the same sweep rate for both the forward and reverse sweep. The corresponding current is recorded as a function of the varying potential. For the cathodic scan (applied potential is decreasing) the current has a negative sign, while for the anodic scan (applied potential is increasing) the current has a positive sign.

This technique has been utilised extensively for the electrochemical co-deposition process, as discussed in Chapter 3. Furthermore, it is applied to investigate the electrochemical sensing and capacitive phenomena. These results have been discussed in Chapters 4, 5 and 6.

2.2.2 Chronoamperometry:

Chronoamperometry (CA) is versatile and powerful method for obtaining the preliminary information about nucleation and growth mechanism in an electrochemical system. It is also useful for the determination of a nucleation rate constant and an adsorption isotherm. In CA, the current is measured as a function of time as a response to a (sequence of) potential pulse. The recorded current can be analyzed and its nature can be identified from the variations with time. In particular, when measuring at short times, the capacitive component is dominant ($\propto e^{-t/RC}$) where R is the solution resistance and C is the capacitance, while at longer time scales, the diffusion limited faradaic current prevails ($\propto t^{-1/2}$).

Fig. 2.3 depicts a schematic plot of the applied voltage (a) and its corresponding chrnoamperometry plot (b). At the beginning, the potential of the working electrode is held at

E_i (Fig. 2.3). At t = 0 the potential is instantaneously changed to a new value E_1, and corresponding current time response is recorded as shown in Fig. 2.3.

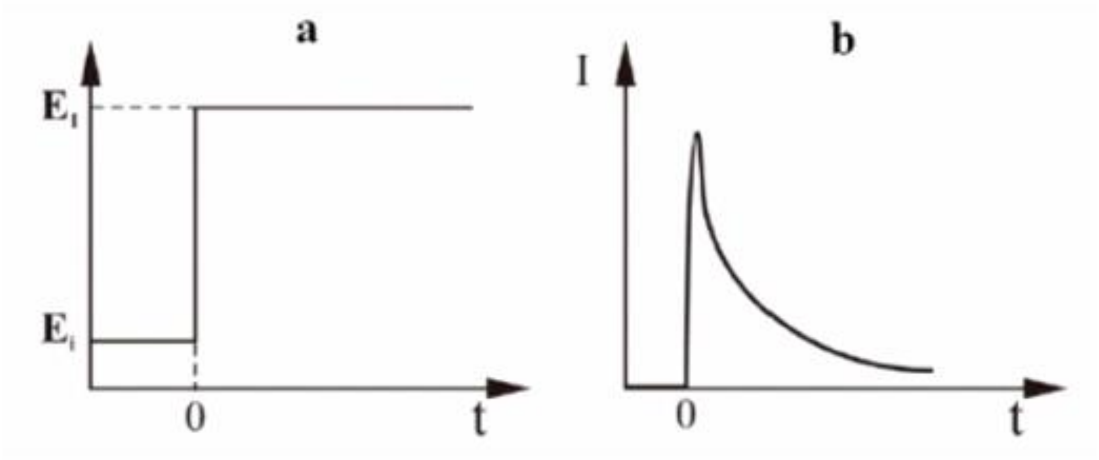

Fig.2.3: Schematic representation of applied voltage (a) and its corresponding chronoamperometry plot (b)

The exact form of current-time dependence for a planar electrode can be represented using the Cottrell equation:

$$I = \{nF(D_o)^{1/2}C^{\infty}_{o}\}/(\pi t)^{1/2}$$

For diffusion-controlled process, the rate of fall of the current goes as $t^{-1/2}$. This characteristic is regularly used as a test for diffusive processes and from the slope of I vs. $t^{-1/2}$ from which the diffusion coefficient D_O can be calculated.

For shorter time durations, the current consists of a large non-faradaic component due to charging of the double-layer capacitance. The non-faradaic component of current decays exponentially, with a time constant RC_d, where R is an uncompensated resistance and C_d is the double layer capacitance. Mathematically, the decaying and charging currents can be represented by equations (1a) and (1b) respectively

$$I = E/R\ e^{-t/RCd} \qquad (1a)$$

$$I = 1 - E/R\ e^{-t/RCd} \qquad (1b)$$

Therefore, measurements should be performed for times which are much greater than RC_d. After passing current for time equivalent to RC_d, the double layer capacitance is charged by 63 % and after $3RC_d$ by 95 %.

After sufficient duration of time, natural convection processes comes into effect and diffusion in that case is not the only mode of the mass transport. Typically, time range of chronoamperometric measurements normally lies within few 100 s. However, the current and voltage characteristics of a potentiostat can limit the maximum current and temporal resolution. Even though chronoamperometry is a very simple technique, it presents a number of challenges, which are related to the interpretation of the current-transient curve. Hence, it is absolutely essential to find the possibility of a comparative analysis of the chronoamperometric results with the results of CA and other techniques. This type of comparison is essential for gaining a complete understanding of the system under study.

2.2.3. Electrochemical Impedance Spectroscopy:

Impedance indicates the ability of a system to resist the flow of an electric current. Electrochemical impedance is measured by applying an AC potential to an electrochemical cell and measuring the current through the cell. In the case of a sinusoidal potential excitation, the response is an AC current signal, containing the excitation frequency along with the associated higher harmonics. This current signal can be represented as a Fourier series expressed as a sum of sinusoidal functions. In order to measure electrochemical impedance, a small excitation signal is applied to generate a pseudo-linear response from the cell. In a linear (or pseudo-linear) system, the current response to a sinusoidal potential will be a sinusoid at the same frequency but shifted in phase. The following section describes linearity in more details:

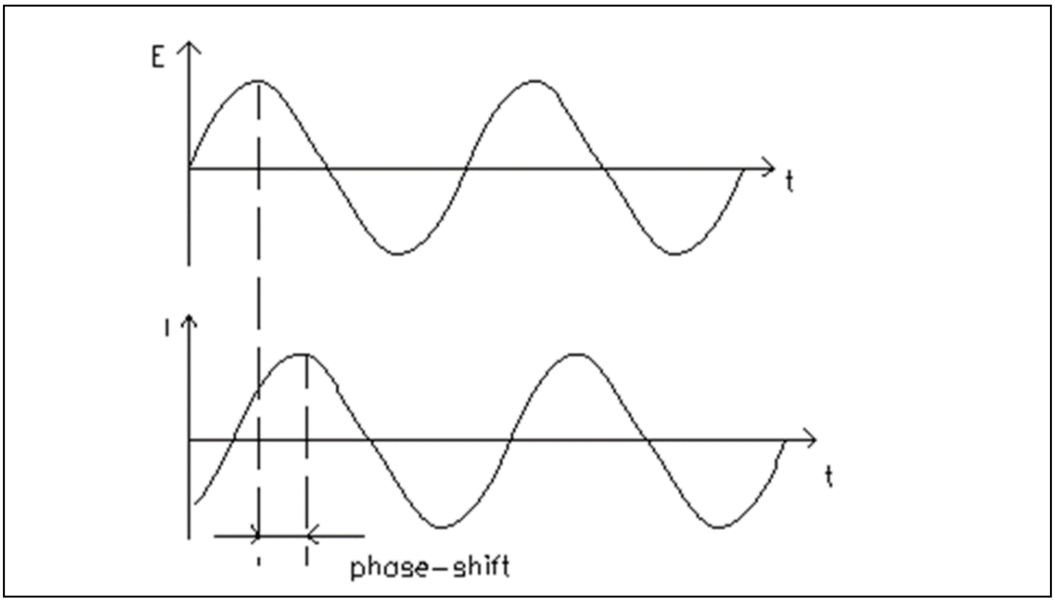

Fig.2.4: Schematic plot depicting a sinusoidal potential and its response current

The excitation signal, expressed as a function of time, has the form of:

$$E(t) = E_o \cos(\omega t) \qquad (2)$$

Where, E(t) is the potential at time t and E_o is the amplitude of the signal, ω and is the radial frequency. The relationship between radial frequency (expressed in radians/second) and frequency f (expressed in Hertz (1/sec)). Z:impedance

$$\omega = 2*\pi*f \qquad (3)$$

$$Z(\omega, Eo) = dE(\omega)/dI(\omega) \qquad (4)$$

Since dI(ω) contains information on phase as well as magnitude, the AC current may contain the characteristics of a phase lag Φ with respect to the AC voltage. This can be correlated with the schematic plot of Fig. 2.4.

If we apply $E=Eo +dE\cos(\omega t)$ and measure the subsequent current as

$$I = Io + dI\cos(\omega t - \Phi) \qquad (5)$$

The impedance can be represented as:

$$Z(\omega, E_o) = (dE / dI) \, x\{\cos(\Phi) + i\sin(\Phi)\} \qquad (6)$$

where $i^2 = -1$ and both magnitude and phase of the impedance, Z and Φ vary with ω.

In a linear system, the response signal, the current I(t), is shifted in phase (Φ) and can be represented as:

$$I(t) = I_o\cos(\omega t - \Phi) \qquad (7)$$

Using this expression, the impedance can be calculated as follows (in terms of a magnitude, Z_0, and a phase shift, Φ):

$$Z(t) = E(t)/I(t) = E_o\cos(\omega t)/I_o\cos(\omega t - \Phi) = Z_o\cos(\omega t)/\cos(\omega t - \Phi) \qquad (8)$$

Alternately, impedance may also be expressed as following:

The result will be $Z(\omega, Eo) = dE(\omega) / dI(\omega)$ (9)

The response to an applied electric field E(t) is I(t), and upon perturbing the system at a certain field E with a small perturbation dE, the response current I has a small response perturbation dI. In the first approximation, as the perturbation dE is small, the response dI will be a linear. This is depicted schematically in Fig. 2.5.

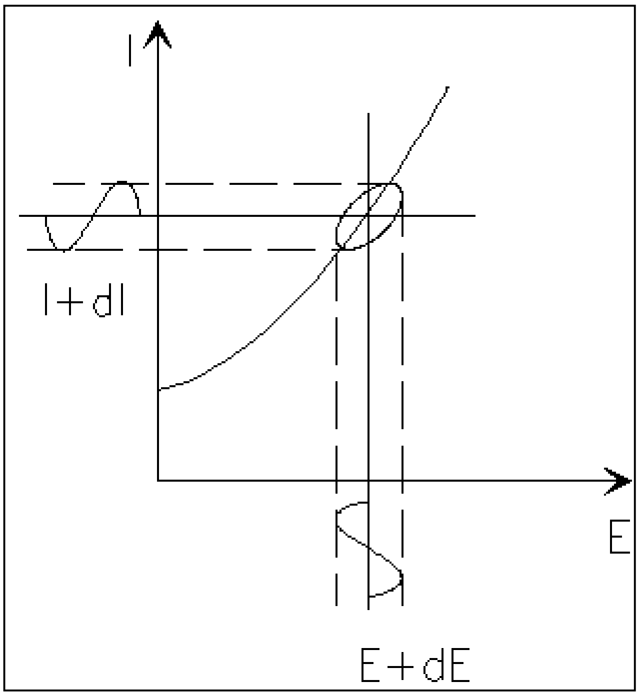

Fig.2.5: Schematic figure showing response dI of dE from the current (I)/Field(E) relation

The plot of the applied sinusoidal signal and the sinusoidal response signal I(t), results in the superposition results in an oval figure, also known as a 'Lissajous figure'.

The impedance, written as,

$$Z(t) = E(t)/I(t) = E_o\cos(\omega t)/I_o\cos(\omega t\text{-}\Phi) \qquad (10)$$

Using Eulers relationship, $\exp(i\Phi) = \cos\Phi + i\sin\Phi$, the impedance may be expressed as a complex function. The potential may be described as

$$E(t) = E_o\exp(i\omega t) \qquad (11)$$

And the current response as

$$I(t) = I_o\exp(i\omega t\text{-}\ \Phi) \qquad (12)$$

Hence, the impedance is represented as a complex number,

$$Z = E/I = Z_o exp(i\Phi) = Z_o(\cos \Phi + i\sin \Phi) \qquad (13)$$

The data representation i.e. the Nyquist Plot is with reference to the Impedance Vector, that can be represented as follows:

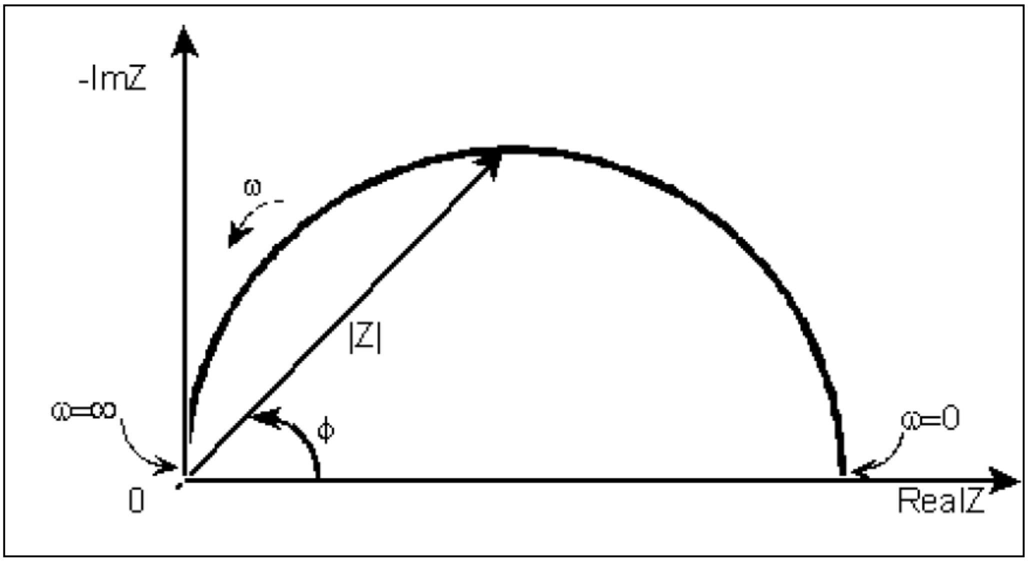

Fig.2.6: Schematic plot for data representation of Nyquist plot along with the impedance vector for a typical RC circuit.

It is evident from the expression above that the impedance, Z(ω) is composed of a real and an imaginary part, which are plotted on the x and the y axes respectively. The resulting Nyquist plot is also known as the electrochemical impedance spectrum. The impedance can be represented as a vector of length |Z|. The angle between this vector and the X axis is Φ.

The data points corresponding to the low frequency values fall on the right side of the plot and those recorded at higher frequencies are on the left. The Nyquist plot in the schematic represented in Fig.2.6 is representative of a typical RC circuit, wherein, the semicircle is a characteristic of a single value of time constant. The EIS plots often depict more than one time constants, depending on the constituent electrochemical processes. Based on the experimental conditions, only a portion of one or more of their semicircles is seen.

Another representation of EIS data is through a Bode plot. The impedance is plotted as the logarithm of frequency on the x- axis, and both the absolute value of the impedance ($|Z| = Z_0$) and phase-shift are plotted on the y-axis. The schematic representing the Bode plot for the RC circuit is shown in Fig. 2.7. It is noteworthy, that unlike the Nyquist plot, the Bode plot explicitly depicts information on frequency dependence of the system.

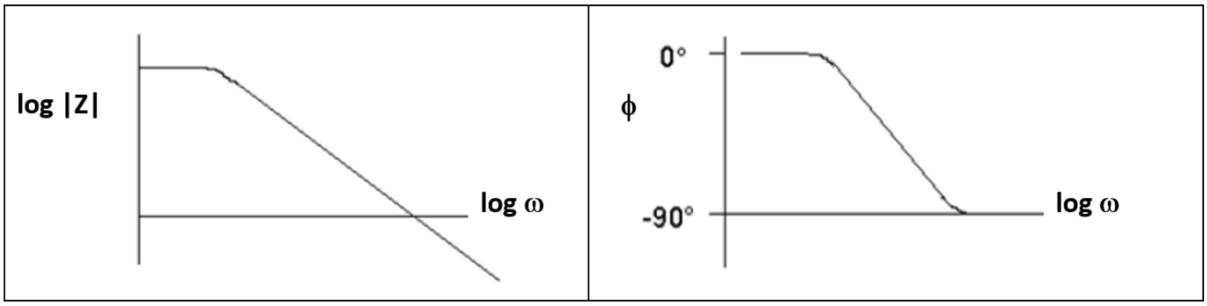

Fig.2.7: Schematic representation of a bode plot for an RC circuit

The analysis of impedance spectra of linear circuits is simpler as compared to their non-linear counterparts. Fundamentally, a linear system is one that satisfies the property of superposition, i.e. if the input consists of the weighted sum of several signals, then the output is simply the superposition.

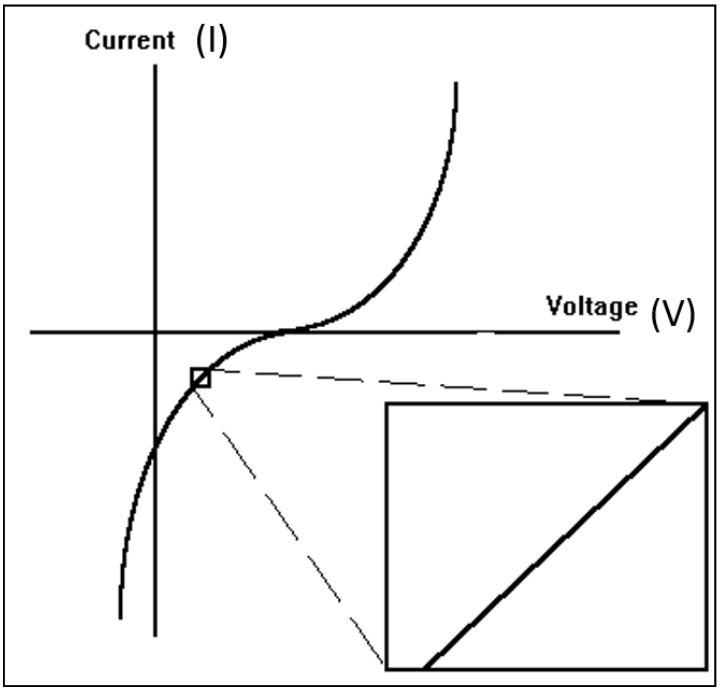

Fig.2.8: Schematic representation of the current versus voltage of an electrochemical cell depicting pseudo-linearity

For a potentiostated electrochemical cell, the input is the potential and the output is the current. Evidently, the response of electrochemical cells is not linear since doubling the voltage would not lead to the doubling of current.

However, electrochemical systems can be approximated as being pseudo-linear. For example, if we consider an infinitesimally small portion of a cell's current versus voltage curve, it appears to be linear. This is depicted in Fig. 2.8. For performing EIS measurements a small amplitude (1 to 10 mV) of AC signal is applied to the cell. The small amplitude signal confines the system to a pseudo-linear domain of the cell's I-V response.

It is noteworthy that we do not measure the cell's nonlinear response to the DC potential but in EIS we only examine the cell current at the excitation frequency. Measuring an EIS spectrum over a broad range of frequency often takes a long time (~several hours). Furthermore, the system under study must be at a steady state throughout the duration of measurement. A common cause of problems in EIS measurements and their analysis is the phenomenon of drifting in the system being measured. This makes it difficult to maintain a steady state. The cell characteristics may undergo changes owing to processes such as adsorption of solution impurities, growth of oxide layers, built-up of reaction products in solution, coating degradation, temperature changes etc. Standard EIS analysis tools may present inaccurate results on a system that is not in a steady state.

EIS data is routinely analyzed by fitting it to an equivalent electrical circuit model. The circuit elements in the model are common electrical elements such as resistors, capacitors, and inductors. This exercise is useful, because the elements in the model bear a correspondence in the physical electrochemistry of the system. As an example, most circuit models contain a resistor that models the cell's solution resistance.

The Table 1 lists the common circuit elements, the equation for their current versus voltage relationship, and their impedance:

Table1. List of common circuit elements and their connection with impedance

Component	**Current vs. Voltage**	**Impedance**
Resistor	$E = IR$	$Z=R$
Inductor	$E = LdI/dt$	$Z = i\omega L$
Capacitor	$I = CdE/dt$	$Z=1/i\omega C$

Electrolyte resistance is a significant contributing factor to the impedance of an electrochemical cell. A modern three electrode potentiostat compensates for the solution resistance between the counter and reference electrodes. However, any solution resistance between the reference electrode and the working electrode must be accounted for while fitting it with an electrical circuit. The resistance of an ionic solution depends on the ionic concentration, type of ions, temperature and the geometry of the area in which current is carried. In a bounded region of area, A and length l, across which a uniform current is transported, the resistance is defined as:

$$R = \rho l/A \qquad (14)$$

Where, ρ is the solution resistivity. The conductivity of the solution, σ, is more commonly used in solution resistance calculations. Its relationship with solution resistance is:

$$R = (1/\sigma)(l/A) \qquad (15)$$

The values of σ corresponding to specific solutions can be derived from standard tabulated values.

However, in most of the cases the electrochemical cells do not possess a uniform current distribution across a definite electrolyte area. In most modern EIS set up, the experimental EIS data can be fitted to a circuit model to obtain the values of various electrochemical circuit parameters.

At the interface between an electrode and its surrounding electrolyte an electric double layer is present. As depicted in Fig. 2.9, this double layer is formed as ions from the solution adhere to the electrode surface. Charges in the electrode are separated (few angstroms) from the charges of these ions.

The value of the double layer capacitance depends on factors, such as the electrode potential, temperature, ionic concentrations, types of ions, oxide layers, electrode roughness and impurity adsorption.

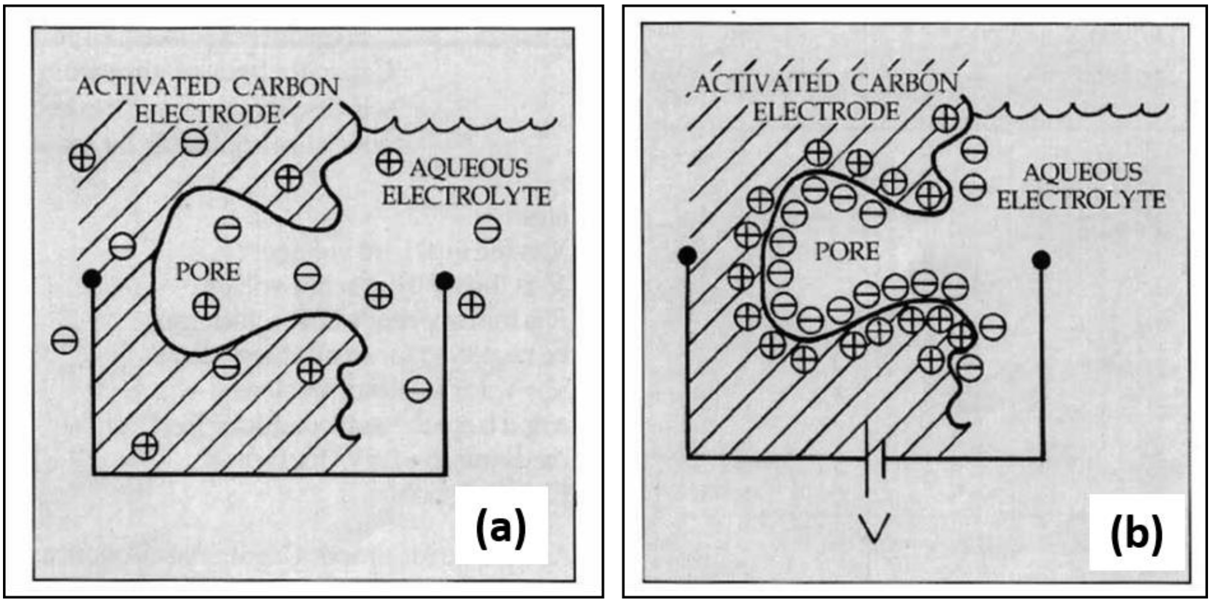

Fig.2.9: Schematic representation for the principle of formation of electric double layer as depicted in absence and presence of external bias

When an electrode is polarized, current flows via electrochemical reactions that occur at the surface of the electrode. The amount of current is controlled by the kinetics of the reactions and the diffusion of reactants both towards and away from the electrode.

A single kinetically controlled electrochemical reaction at the working electrode, results in the formation of a resistance. In this case, we do not have a mixed potential, but rather a single reaction at equilibrium. This is true for a metal substrate in contact with an electrolyte. The metal molecules can be electrolytically dissolved into the electrolyte, according to:

$$Me \longleftrightarrow Me^{n+} + ne^{-} \qquad (16)$$

Or in more general terms,

$$Red \longleftrightarrow Ox + ne^{-} \qquad (17)$$

Diffusion processes within the electrochemical cell results in the formation of the Warburg impedance, which in turn depends on the frequency of the AC potential perturbation. At significantly higher frequencies the Warburg impedance is small, since the diffusing reactants don't have to move very far. At low frequencies, the reactants tend to diffuse farther, resulting in a substantial contribution to the Warburg impedance.

On the Nyquist plot the infinite Warburg impedance appears as a diagonal line with a slope of 0.5. On a Bode plot, the Warburg impedance exhibits a phase shift of 45°.

A capacitor is formed when two conducting plates are separated by a non-conducting media, called the dielectric. The value of the capacitance depends on the size of the plates, the distance between the plates and the properties of the dielectric.

The relationship is:

$$C = \varepsilon_o \varepsilon_r A/d \qquad (18)$$

Where,

ε_o = electrical permittivity, ε_r = relative electrical permittivity, A = surface of one plate,

d = distance between two plates

On one hand, the electrical permittivity is a physical constant, while the relative electrical permittivity depends on the medium. Permittivity of water is around 80.1 whereas organic coatings have permittivity value in the range between 4 and 8. The capacitance of a coated substance changes as it absorbs water. Hence, EIS can be used to measure that change.

Capacitors in EIS experiments often do not behave ideally. Instead they act like a constant phase element (CPE) as defined below

$$Z = A(i\omega)^{-\alpha} \qquad (19)$$

When this equation describes a capacitor, the constant A = 1/C (the inverse of capacitance) and the exponent $\alpha = 1$. For a constant phase element, the exponent is less than one. The double layer capacitor on real cells often behave as a CPE instead of a capacitor. Several theories have been proposed to account for the non-ideal behaviour of the double layer, but none have been universally accepted. In most cases α is treated as an empirical constant without emphasizing on its physical basis.

Some of the common equivalent circuit elements used in circuit models have been tabulated in Table 2.

Table2: Elements used in equivalent circuit models:

Equivalent element	**Admittance**	**Impedance**
R	1/R	R
C	$i\omega C$	$1/i\omega C$
L	$1/i\omega L$	$i\omega L$
W (infinite warburg)	$Y_o(i\omega)^{1/2}$	$1/Y_o(i\omega)^{1/2}$
Q(CPE)	$Y_o(i\omega)^{\alpha}$	$1/Y_o(i\omega)^{\alpha}$

For instance, a purely capacitive coating generally has a very high impedance and the value of capacitance cannot be determined from the Nyquist plot. It can be determined from a curve fit or from the examination of the data points. The intercept of the curve with the real axis gives an estimate of the solution resistance.

The same data may be represented as a bode plot as seen in Fig. 2.10. The capacitance can be estimated from the graph, but the solution resistance value doesn’t appear on the chart. Even at frequencies of 100 kHz, the impedance of the coating is higher than the solution resistance.

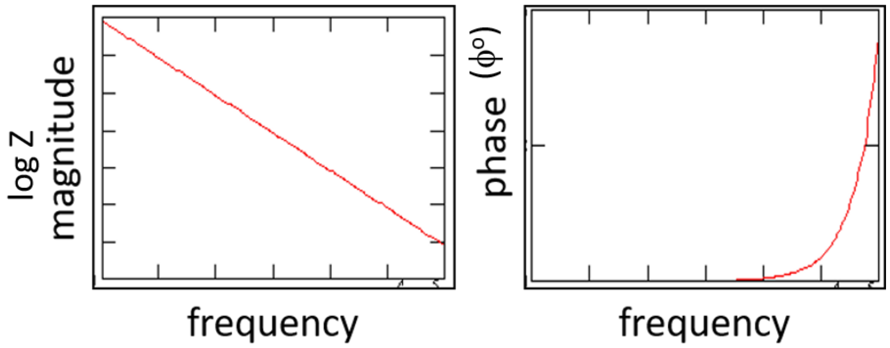

Fig.2.10: Schematic representation of the Bode plot of a purely capacitive system

For modelling the electrode/electrolyte interface with an equivalent circuit, one of the most commonly used circuits is the Randle's circuit. It includes a solution resistance, a double layer capacitor and a charge transfer or polarization resistance. In addition to being a useful model in its own right, the Randle's cell model is usually taken as the starting point for other more complex circuit models. The equivalent circuit for the Randle's cell is shown Figure 2.11(a). The double layer capacitance is in parallel with the impedance due to the charge transfer reaction.

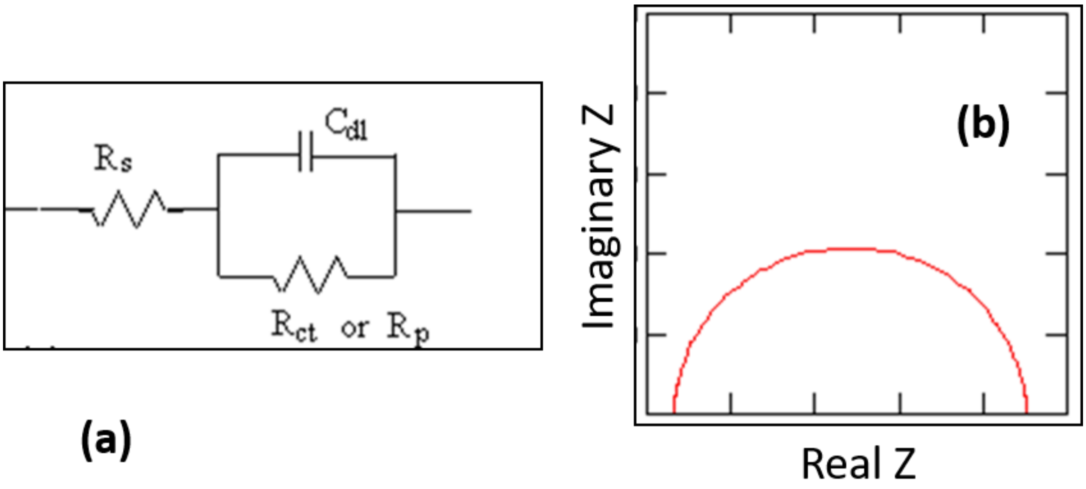

Fig. 2.11: Schematic representation of a Randle's circuit (a)corresponding EIS plot (b)

The Nyquist plot for a Randle’s cell is always a semicircle. The solution resistance can be estimated by reading the real axis value at the high frequency intercept. This intercept is near the origin of the plot. The schematic in Fig. 2.11 corresponds to a solution resistance of 20 Ohms and charge transfer resistance of 250 Ohms. The real axis value at the other low frequency intercept is the sum of the polarization resistance and solution resistance. The diameter of the semicircle is equal to the polarization resistance.

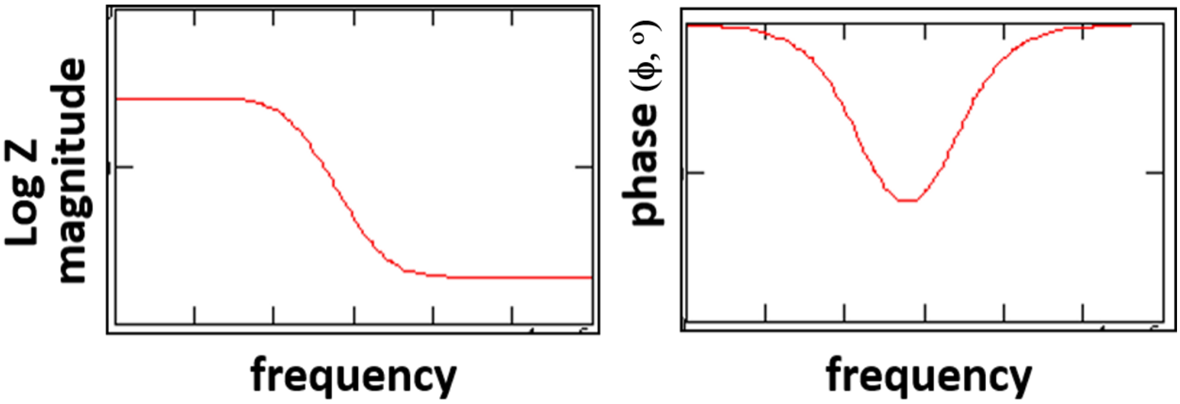

Fig.2.12: Schematic representation of the Bode plot for the Randle’s circuit corresponding to Fig.2.11(a)

Fig. 2.12 gives the schematic representation of the bode plot corresponding to the Randle’s circuit depicted in Fig. 2.11(a). The solution resistance and the sum of the solution resistance and the polarization resistance can be read from the magnitude plot. The phase angle does not reach 90° as it would for a purely capacitive impedance. If the values for R_s and R_p were more widely separated, the phase would approach 90°.

Next, let us consider the example of a half fuel cell.

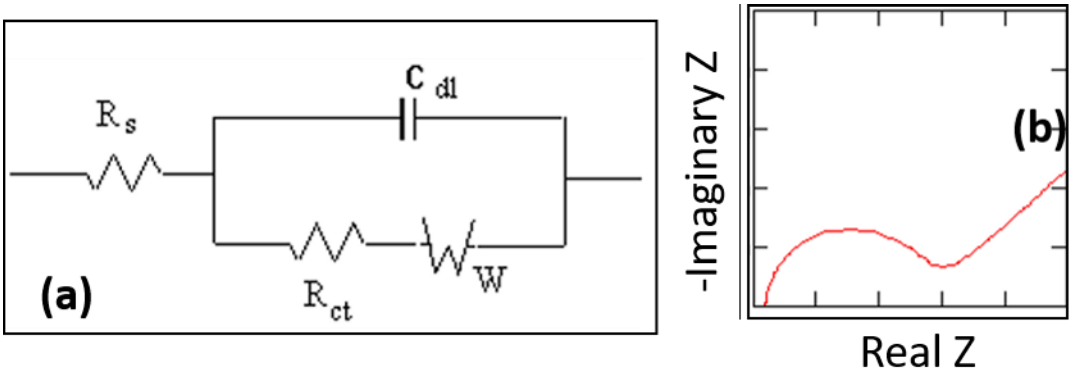

Fig.2.13: Schematic representation of a circuit corresponding to a half fuel cell (a) and its corresponding EIS spectra (b)

This circuit models a cell where polarization is due to a combination of kinetic and diffusion processes. The Nyquist plot for this circuit is shown in the Fig. 2.13(b).

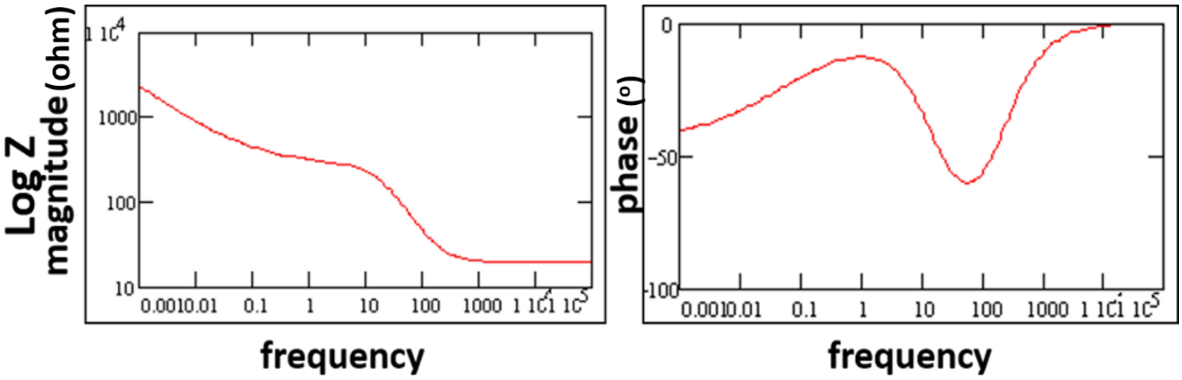

Fig.2.14: Schematic representation of the Bode plot for Nyquist spectrum corresponding to Fig.2.13

Fig. 2.14 depicts the schematic representation for the Bode plot corresponding to the half fuel cell as represented in the Nyquist Plot of Fig. 2.13. The lower frequency limit is set to 1 mHz to better illustrate the differences in the slope of the magnitude and in the phase between the capacitor and Warburg impedance. It can be seen that the phase approaches 45^{o} at low frequency.

2.2.4. Mott-Schottky Analysis:

The following section presents a basic understanding of the Mott-Schottky Analysis [49]. While studying electrode-electrolyte systems especially, where semiconductors electrodes are used, it is important to understand the nature of the semiconductor-electrolyte interface in terms of their flat band potential representation. Fundamentally, the flat band potential is the potential required to bring back the semiconductor band edges to their flat band position. In this context, understanding the relationship between semiconductor and electrolyte energy levels is of crucial significance. This can be understood with better clarity with the example of an n type semiconductor, which is in contact with a redox couple in the electrolyte solution.

Fig. 2.15 depicts the energy level diagram corresponding to this electrode electrolyte system.

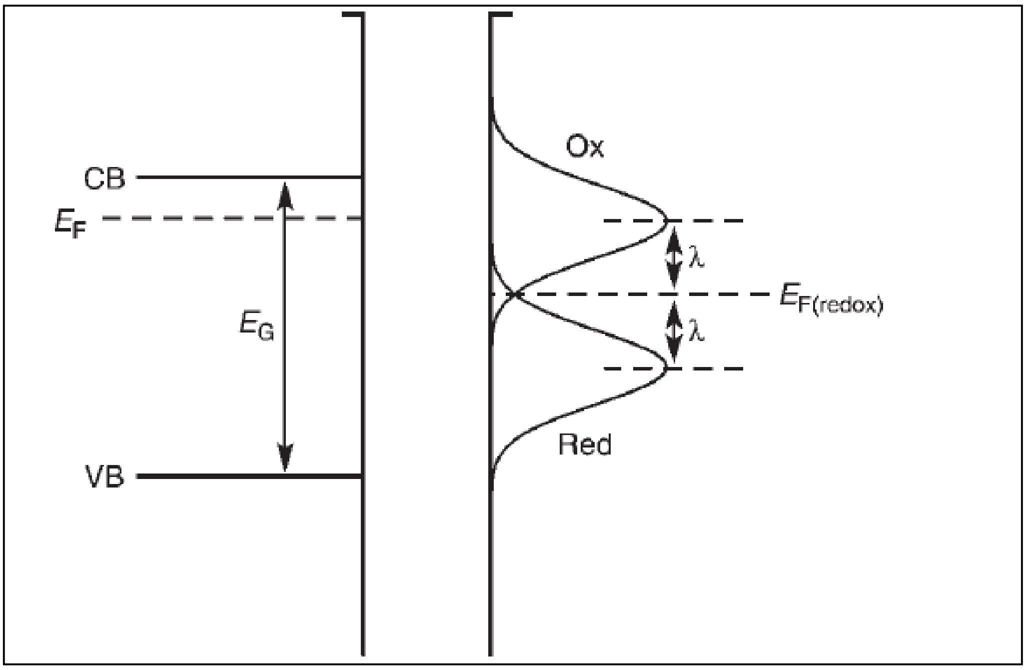

Fig. 2.15: Schematic representation of energy level diagram corresponding to electrode-electrolyte system

The valence and conduction band edges of the semiconductor, can be identified as VB and CB respectively, the band gap energy as E_G, and the Fermi level as E_F. The Fermi level, represents the energy at which the probability of occupancy of an electronic state is 0.5. These band positions are dependent on the semiconductor potential Φ, changing as -eΦ, where 'e' denotes the charge of an electron.

The energy levels for the redox active species in the solution arise by the virtue of donors (R_{ed}) and acceptors (O_x) in solution; i.e.,

$$O_x + e^- \longleftrightarrow R_{ed} \qquad (20)$$

The energies of the solution's states dependent on the state, whether it is occupied (R_{ed}) or vacant (O_x) owing to the presence of different solvent sheath energies λ, around the R_{ed} and O_x species. Since, solvent molecules exchange energy between the coordination sphere of the redox active species and the bulk electrolyte, it is a dynamic process leading to a range of solvent sheath energies, the density of redox states is described in terms of their individual Gaussian profiles. The redox Fermi level $E_{F(redox)}$, is defined as the energy at which the probability of a state being occupied by an electron is 0.5. In the present case, when an n type semiconductor and a redox couple come into contact, (E_F is higher in energy compared to E_{Fredox}), equilibrium can be achieved through transfer of electrons from the semiconductor to Ox so that the Fermi levels for both phases equilibrate. This is depicted in Fig.2.16.

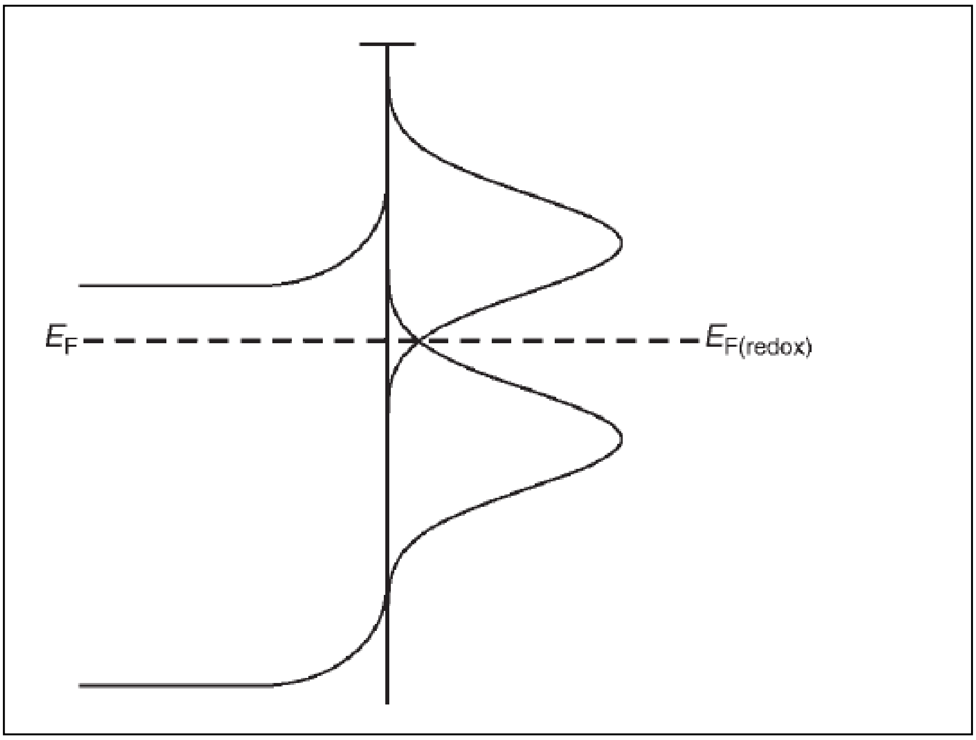

Fig.2.16: Schematic representation depicting the Fermi levels of electrode/electrolyte to be equal

As a result, the semiconductor is charged positively, and since semiconductor carrier densities are much lower than those in solution, the diffused charge in the semiconductor i.e. the space charge, can be counterbalanced by a sheet of charge in the electrolyte. Furthermore, varying the value of applied voltage to the semiconductor, the semiconductor and redox couple fermi levels tend to separate and hence, the level of band bending owing to electron depletion in the semiconductor gets modified in accordance with the value of the applied voltage. When the applied voltage is at such a value that there is no band bending, or charge depletion, such as seen in the schematic representation of Fig.2.17, then the semiconductor is at its flat band potential V_{fb}.

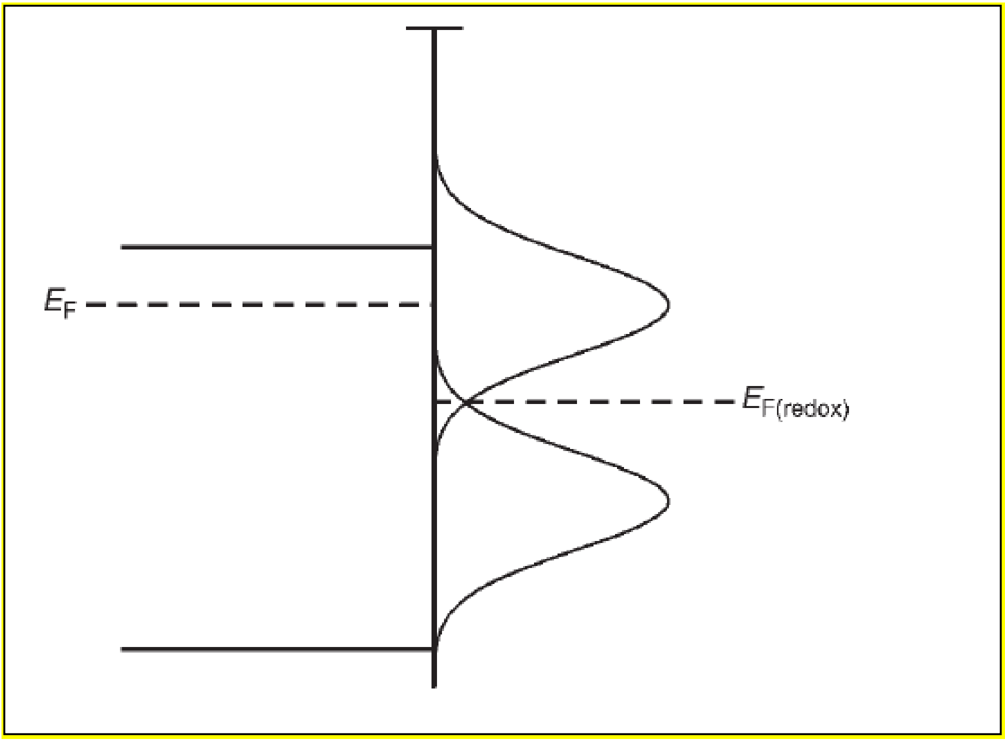

Fig.2.17: Schematic representation of energy levels corresponding to the flat band potential

Furthermore, we can develop an understanding of the Mott-Schottky equation which will be essential for our studies.

Under the circumstances as depicted by Fig. 20.17, i.e. when $E_F > E_{Fredox}$, the Mott-Schottky equation can be useful for determining the flat-band potential of the semiconductor. Understanding its derivation is crucial for the experiment, since it forms the basis of several key concepts associated with the semiconductor-electrolyte interface. The starting point of the derivation is the Poisson's equation in one dimension, that describes the relationship between charge density and potential difference V in a phase.

$$d^2 V/dx^2 = -\rho/\varepsilon\varepsilon_o \qquad (21)$$

where ρ corresponds to the charge density at a position x away from the semiconductor surface, ε is the dielectric constant of the semiconductor and ε_o is the permittivity of free space. Using the Boltzmann distribution to describe the distribution of electrons in the space charge region and Gauss's law in relating the electric field through the interface to the charge contained within that region, Poisson's equation can be solved to give the Mott-Schottky equation as follows:

For a semiconductor, the charge density of an n type semiconductor can be approximated as

$$\rho = eN_D(1-e-^{eV/K_bT}) \qquad (22)$$

Thus, the Poisson's equation becomes

$$d^2\, V/dx^2 = eND/\varepsilon\varepsilon_o\,(1-e-^{eV/K_bT}) \qquad (23)$$

Using the identity,

$$2(d\, V/dx)(d^2\, V/dx^2) = d/dx(d\, V/dx)^2 \qquad (24)$$

Integrating with V = d V/dx = 0 in the bulk yields

$$(d\, V/dx)^2 = 2\, eND/\varepsilon\varepsilon_o\,(V-K_bT/e((1-e-^{eV/K_bT})) \quad (25)$$

Using Gauss's law for a charged surface

$$d\, V\,/dx = Q/A\varepsilon\varepsilon_o \qquad (26)$$

The space charge layer forms when V deviates from the flat band potential ($V - V_{fb}$) and the capacitance is defined as

$$C= dQ/dV \qquad (27)$$

Which yields the Mott-Schottky Equation:

$$1/C^2 = 2/\varepsilon\varepsilon_o A^2 eN_D\,(V - V_{fb} - k_BT/e) \qquad (28)$$

Where,

C = interfacial capacitance, A = area, N_D = number of donors, V = applied voltage, k_B = Boltzmann constant, T = absolute temperature, e = electronic charge

Therefore, a plot of $1/C^2$ vs. V would give a straight line from where V_{fb} can be determined from the intercept on the V axis. The value of N_D can also be conveniently obtained from the slope by substituting the value of ε and A.

Now let us discuss some basic concepts related with the advanced materials characterization tools used in this work [50, 51, 52, 53, 54, 55].

2.2.5. X- ray Diffraction:

The process by which X-rays interact with and are reflected from the atoms in a crystalline solid is called x- ray diffraction. The diffracted X-rays generate a pattern that reveals the location of each atom in a given compound. X-ray diffraction (XRD) studies present experimental results on the geometry or shape of a molecule using X-ray beam as a probe. This technique is essentially based on the elastic scattering of X-rays from structures that have long range order, i.e. crystalline solids. XRD is an important method to characterize the structure of crystalline material. Furthermore, it is applicable for determination of either the lattice parameters or arrangement of individual atoms in a single crystal and to perform the phase analysis in case of polycrystalline materials and compounds. With the application of a thorough analysis using XRD and fundamental concepts of crystallography, it is possible to determine the exact crystal structure and the resultant molecular formula of a crystalline compound under study.

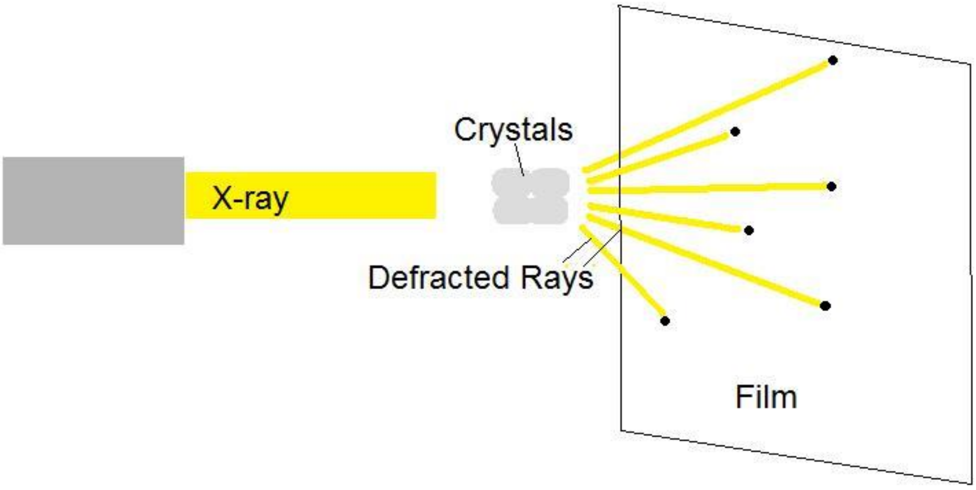

Fig.2.18: Schematic representation of material interaction with X-rays

When the X-ray beam encounters the regular three-dimensional arrangement of atoms in a crystal, the majority of X-rays undergo destructive interference with each-other and ultimately, cancel each-other out. However, in certain specific directions the X-ray beams interfere constructively and reinforce one another. It is these reinforced diffracted X-rays that produce the characteristic X-ray diffraction pattern that is used for crystal structure determination.

These reflections occur only under certain conditions which satisfy the condition for constructive interference:

$$n = 2d\sin(\theta) \qquad (29)$$

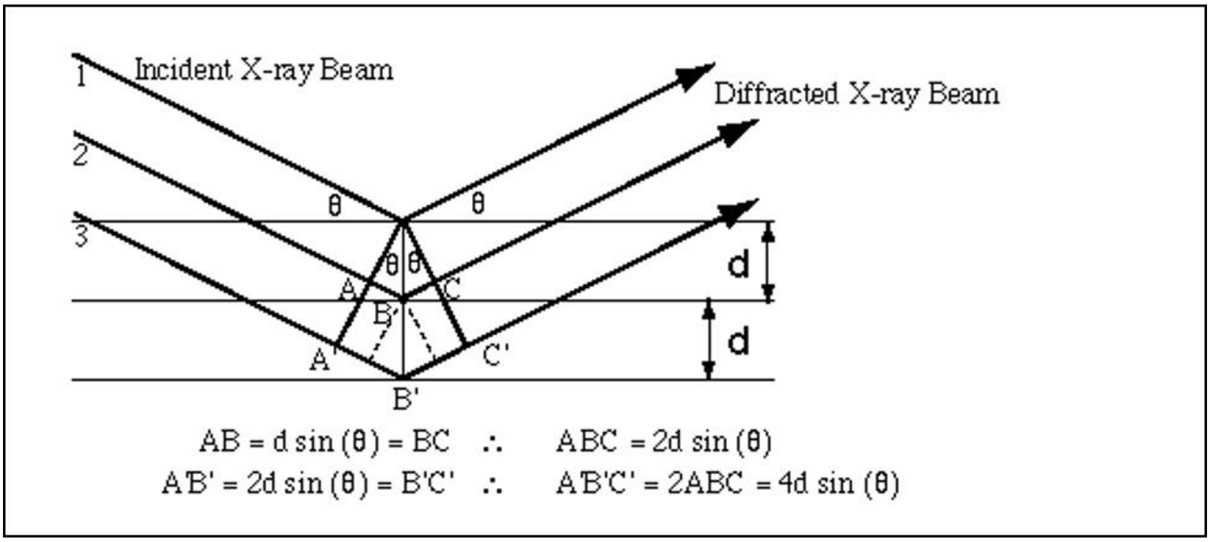

Fig.2.19: Schematic representation of Bragg Planes depicting geometrical analysis of X ray diffraction

The above equation is also known as Bragg's equation. Here *n* is an integer (1,2,3. n), lambda is the wavelength, *d* is the distance between the atomic planes, and theta is the angle of incidence of the X-ray beams. An X-ray beam takes a longer (but parallel) path because if 'reflects' off an adjacent atomic plane. This path length difference must be equal to an integer value of the λ of the incident X-ray beams for the constructive interference to occur such that a reinforced diffracted beam is produced. X-ray crystallography is a method for determining the arrangement of atoms within a crystal, in which a beam of X-rays strikes a crystal surface and gets scattered into many different directions. Using the angles and intensities of these scattered beams a three-dimensional picture of the density of electrons within the crystal can be reproduced. After performing an extensive analysis of this electron density picture, the mean positions of the atoms in the crystal can be determined, as well as their chemical bonds, their disorder and various other information about their structural parameters can be obtained. Since a large variety of materials can exist in a crystalline state, X-ray crystallography has been fundamental in the development and understanding of many scientific areas which involve studying and understanding of structure of materials.

2.2.6. Raman Spectroscopy:

Raman spectroscopy is a materials characterization technique based on the measurement of inelastically scattered light (typically monochromatic laser light) for exploring the vibrational (and rotational) modes of organic or inorganic molecules. When light interacts with matter, the photons can be absorbed, transmitted or scattered. Absorption can take place when the energy of the photons is equal to the energy difference between two, real vibrational states (IR spectroscopy). Scattering, on the other hand, begins with the excitation to a virtual vibrational state. Most of the photons are elastically scattered, i.e. they retain the same energy (and frequency) which does not affect the vibrational state of the material. This phenomenon is known as the Rayleigh scattering. However, a small number of photons (~1 in 10^7) are scattered inelastically, i.e. their exchange energy affects the vibrational state of the material. If the photons lose energy, which is the case when the system gains vibrational energy, the resulting phenomenon is known as Stokes Raman scattering. Conversely, if the photons gain energy, in which case the system loses vibrational energy, it is known as anti-Stokes Raman scattering. Since the lower vibrational modes are more populated than the upper ones, Stokes Raman scattering is typically significantly stronger than anti-Stokes Raman scattering. Hence, for a vibrational mode to be Raman-active, a change in the polarizability needs to be introduced for the molecule under study. The Raman shift can be calculated according to:

$$\Delta\nu\,(cm^{-1}) = (1/\lambda_o\,(nm) - 1/\lambda_1(nm)) \times 10^7\,(nm)/(cm) \qquad (30)$$

where $\tilde{\nu}$ is the wavenumber, λ_0 the incident wavelength and λ_1 the scattered wavelength. The magnitude of Raman shift depends on several parameters, such as geometry of the molecule and the different oxidation states. However, it is worth noting that the Raman shift, which represents differences in wavenumber corresponding to transitions between specific vibrational states, is independent of the frequency of the incident laser.

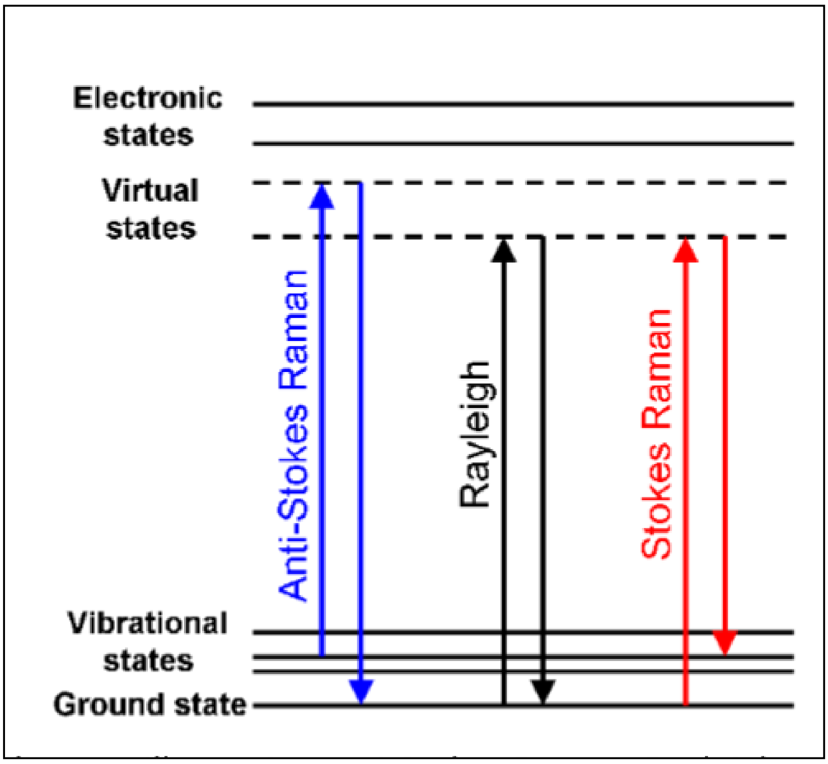

Fig. 2.20: Schematic Representation depicting the energy level transitions during Raman Scattering

. The energy level diagram illustrating anti-Stokes Raman, Rayleigh and Stokes Raman scattering is depicted in Fig.2.20.

The following confocal Raman microscope was used for performing the Raman experiments in this work

Microscope model - Olympus BX 41.

Microscope objective- 50X

Spectrometer model- TRIAX 550 JY equipped with peltier cooled charged coupled detector (model name- Synapse, Horiba JY), Laser excitation wavelength-488 nm

2.2.7. X – Ray photoelectron spectroscopy:

X-ray photoelectron spectroscopy, a well-established technique for electron spectroscopy for chemical analysis, is a type of photoelectron spectroscopy based on the phenomenon of photoelectric effect which is observed when matter is irradiated with X-rays. This method offers a high surface sensitivity (0-10 nm) and is commonly used for quantitative surface analysis in various materials (e.g. semiconductors, catalysts and polymers). All elements except hydrogen and helium can be detected (detection limit of ~0.1 %) using the XPS technique. When matter is irradiated with high energy X-rays (typically Al Kα at 1486.6 eV or Mg Kα at 1253.6 eV), electrons are knocked out from the core energy levels. The kinetic energy of these knocked out electrons primarily depend on the X-ray source and the sample. The binding energy can be calculated according to

$$E_{bind} = h\nu - E_{kin} - \Phi \qquad (31)$$

where E_{bind} is the binding energy of the electrons, $h\nu$ the energy of the incident X-rays, E_{kin} the kinetic energy of the emitted electrons and Φ the work function of the material under study. The graphical representation of the XPS spectrum of a material is typically displayed as a plot of the binding energy in electron volts (eV) vs. the number of detected electrons and is therefore independent of the X-ray source. By utilising the values of known binding energies of specific elements and orbitals (e.g. C 1s) the chemical composition of a sample can be determined. Since these binding energies exhibit additional chemical shifts depending on the chemical state, it is possible to distinguish between different oxidation states of the same element. Auger peaks are a commonly observed as a secondary effect in XPS. Since their kinetic energies are independent of the X-ray source, they exhibit apparent shifts in binding energy when the X-ray source is changed, which can be used to isolate them from the peak positions in the XPS plot. X-ray photoelectron spectrometers usually operate under ultrahigh-vacuum conditions to minimize undesired interactions between the emitted electrons and gas molecules. As a result, the spectra corresponding to volatile and sensitive compounds cannot be measured and the possible effects of the ultrahigh vacuum on the samples should be considered.

2.2.8. Scanning Electron Microscopy:

Scanning electron microscopy (SEM) is a type of imaging technique based on electron microscopy conducted on samples via scanning with a focussed electron beam. This method offers a significant improvement in magnification (resolution of ~1 nm) as compared with the technique of optical microscopy. When electrons interact with matter, a variety of signals containing information about the sample are obtained. Among those, the two commonly used signals are the inelastically scattered secondary electrons and the elastically backscattered electrons. Secondary electrons (from the sample) contain useful morphological information whereas backscattered electrons (from the primary electron beam) are more sensitive to differences in atomic number (mass contrast). In a typical scanning electron microscopy set up, electrons are emitted from the electron gun and are accelerated to a few kilo-electron volts and focussed by a number of condenser lenses. The focussed electron beam then passes through pairs of scanning coils that allows a deflection parallel to the x-y-plane and thus enables a two-dimensional scanning of a rectangular raster scan. Subsequently, the electrons (or X-rays) are detected and amplified. Finally, the image is reconstructed by correlating the position with the signal at each point of the raster scan. Scanning electron microscopes are usually operated under high-vacuum conditions to minimize unwanted interactions between the electrons and gas molecules. As a consequence, the volatile and sensitive compounds cannot be measured and the possible effects of the high vacuum on the samples should be considered.

2.2.9. Transmission Electron Microscopy:

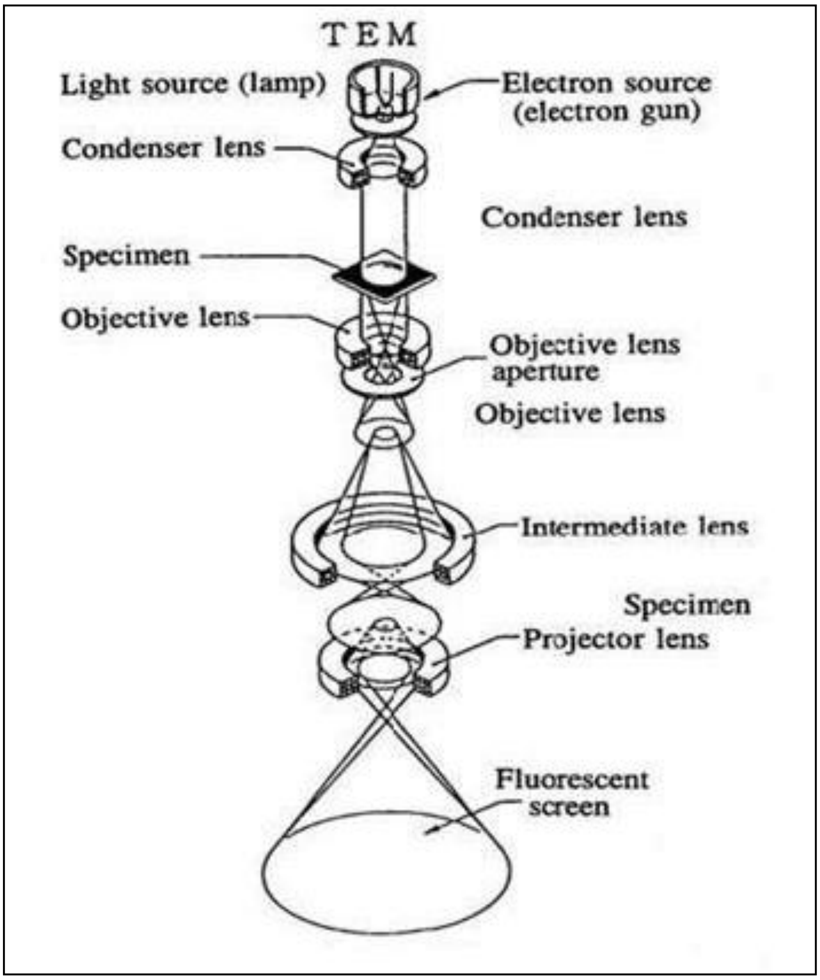

Fig. 2.21: General layout of a TEM describing the path of electron beam in a TEM (Taken from JEOL 2000FX Handbook, [53])

The transmission electron microscope is an extremely useful tool in the microscopic study of materials. Upon shining a high-energy beam of electrons through a very thin sample, and the interactions between the electrons and the atoms can be analyzed to observe features such as the crystal structure and features in the structure like dislocations and grain boundaries. Chemical analysis can also be performed using TEM. TEM can be used to study the growth of layers, their composition and defects in semiconductors. High resolution can be used to analyze the quality, shape, size and density of quantum wells, wires and dots.

The TEM operates on the same basic principles as the optical microscope but uses electrons as a probe instead of light. Since, the wavelength of electrons is much smaller than that of light, the image resolution attainable for TEM images is several orders of magnitude higher than that from an optical microscope. Thus, TEM images can reveal the finest details of internal structure - in some cases as small as individual atoms.

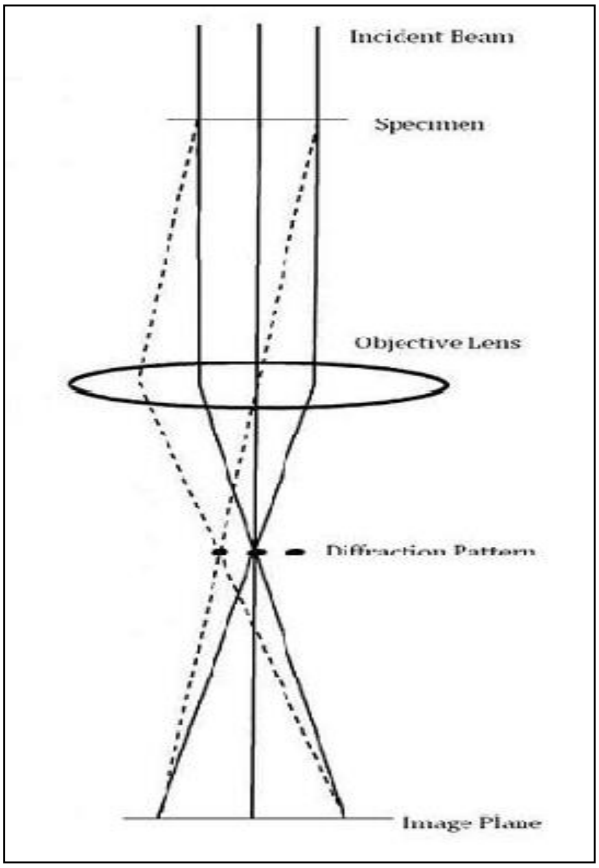

Fig. 2.22: A ray diagram for the diffraction mechanism in TEM

The beam of electrons generated from the electron gun is focused into a narrow, thin, coherent beam using a condenser lens. This beam is restricted by the condenser aperture, which excludes high angle electrons. The beam then strikes the specimen and parts of it are transmitted depending upon the thickness and electron transparency of the specimen. This transmitted portion is focused by the objective lens into an image on phosphor screen or charge coupled device (CCD) camera. Optional objective apertures can be used to enhance the contrast by blocking out high-angle diffracted electrons. The image then passes down the column through the intermediate and projector lenses and is enlarged all the way.

Subsequently, the light beam strikes the phosphor screen and a pattern is generated, allowing the user to see the image. The darker areas of the image represent those regions of the sample where fewer electrons are transmitted through while the lighter regions of the image represent those areas of the sample to which more electrons were transmitted through.

2.2.10. Energy dispersive X-ray spectroscopy:

Energy-dispersive X-ray spectroscopy (EDS, EDX, EDXS or XEDS), or alternatively the energy dispersive X-ray analysis (EDXA) or energy dispersive X-ray microanalysis (EDXMA), is applied for the elemental analysis or chemical characterization of a sample. It relies on the interaction of a particular source of X-ray excitation with the sample under study. Its characterization capabilities are due in large part to the fundamental principle that each element has a unique atomic structure allowing for its characteristic set of peaks on its electromagnetic emission spectrum. This is the main principle behind energy dispersive X-ray spectroscopy.

2.2.11. Electron energy loss spectroscopy:

Electron energy loss spectroscopy (EELS) is a family of techniques that is capable of measuring the change in kinetic energy of electrons after they interact with a specimen. This technique is also applicable for determination of the atomic structure and the relevant chemical properties of a specimen, including: the type and quantity of atoms present, chemical state of atoms and the collective interactions of the atoms with their neighbors.

As the electrons pass through a specimen, they interact with the atoms of the solid and most of the electrons can pass through the thin sample without losing energy. A fraction will undergo inelastic scattering and lose energy as they interact with the specimen. This leaves the sample in an excited state. Subsequently, the material can be de-excited by releasing energy typically in the form of visible photons, x-rays or Auger electrons.

As the incident electron interacts with the sample, it causes a change in both its energy and momentum. As a result, the scattered incident electrons can be detected in the spectrometer and this gives rise to the electron energy loss signal. The sample electron (or collective excitation) carries away this additional energy and momentum.

Core-loss excitations may happen when the tightly bound core electrons are promoted to a higher energy state by the incident electron. The core electron can only be promoted to an energy that is an empty state in the material. These empty sates can be bound states in the material above the Fermi level (so called anti-bonding orbitals in the molecular orbital picture). The states can also be in free electron states above the vacuum level. It is the sudden turn-on of the scattering at the Fermi energy and the probing of empty states which makes the EELS signal sensitive to both the atom type and its electronic state.

Further details regarding the analysis of electron energy loss spectra will be discussed with considerable detail in the next chapter.

CHAPTER 3

Chapter 3

Electrochemical co-deposition of Mn_2O_3-Au composite film

3.1 Introduction:

Composite materials can be defined as being multiphase structures, comprising of significant portions of each component phase. The design perspective of composites, generally take into account the need to tune one or more specific material properties which are a function of the constituent phases and their relative amounts.

The mechanical, electrical, thermal, optical, electrochemical, and catalytic properties of composites may be markedly different from that of their constituent materials. Composites having hierarchical structures are considered as one of the most commonly studied materials for electrochemical applications, due to their complex architecture, which provides a large internal surface area, thereby, enabling synergistic effects for promoting electrochemical reactions at the interface. The development of novel nanoscale materials exhibiting large scale processability has the potential to provide a variety of applications for energy storage, energy conversion, and environmental monitoring.

This chapter presents a systematic study on the synthesis and detailed morphological and structural analysis of manganese oxide-gold (Mn_2O_3-Au) composite thin film prepared by a novel one step electrochemical co-deposition technique. The synthesis was carried out using CV by choosing a suitable potential range in an electrolyte precursor mixture comprising of manganese acetate and aurocholoric acid with sodium sulphate as the supporting electrolyte. It was observed that the morphologies of the films were dependent on the concentration of the electrolyte precursor solutions. The electrodeposition process was performed for two sets of electrolyte concentrations, and in one of them, the molar concentration of manganese acetate was increased by ten times (i.e. from 0.01 M to 0.1 M). In all, a total of four samples were prepared, two each for a given set of electrolyte parameters corresponding to the composite Mn_2O_3-Au thin film and pristine Mn_2O_3 film. A study of co-electrodeposition for two sets of electrolyte parameters presents a thorough understanding of the synthesis process and the key factors which govern the morphology and structure of the co-electrodeposited film. Based on a step by step electrochemical and microscopic analysis, a series of electrochemical reactions were proposed to explain the synthesis mechanism of the co-electrodeposited Mn_2O_3-Au film. For samples corresponding to both the sets of electrolyte parameters, an extensive structural and materials characterization was performed to compare the properties of the composite and pristine electrodeposited films.

3.2 Experimental set up and Materials required:

Fig.1 represents the schematic of the electrochemical set up used in the process of electro-deposition which was conducted in a three-electrode arrangement. The bath temperature of the electrolyte was maintained at 50 ^{o}C for both the cases. Indium tin oxide coated glass sheet (ITO) was obtained from Sigma Aldrich and used as substrates for synthesis. Manganese acetate and sodium sulphate were obtained from Merck India Ltd. and $HAuCl_4.3H_2O$ was procured from Sigma Aldrich. All chemicals were analytical grade and used as obtained without further purification. Millipore water (18Mohm-cm) from Merck Millipore purification system was used during the entire synthesis and electrochemical characterization processes.

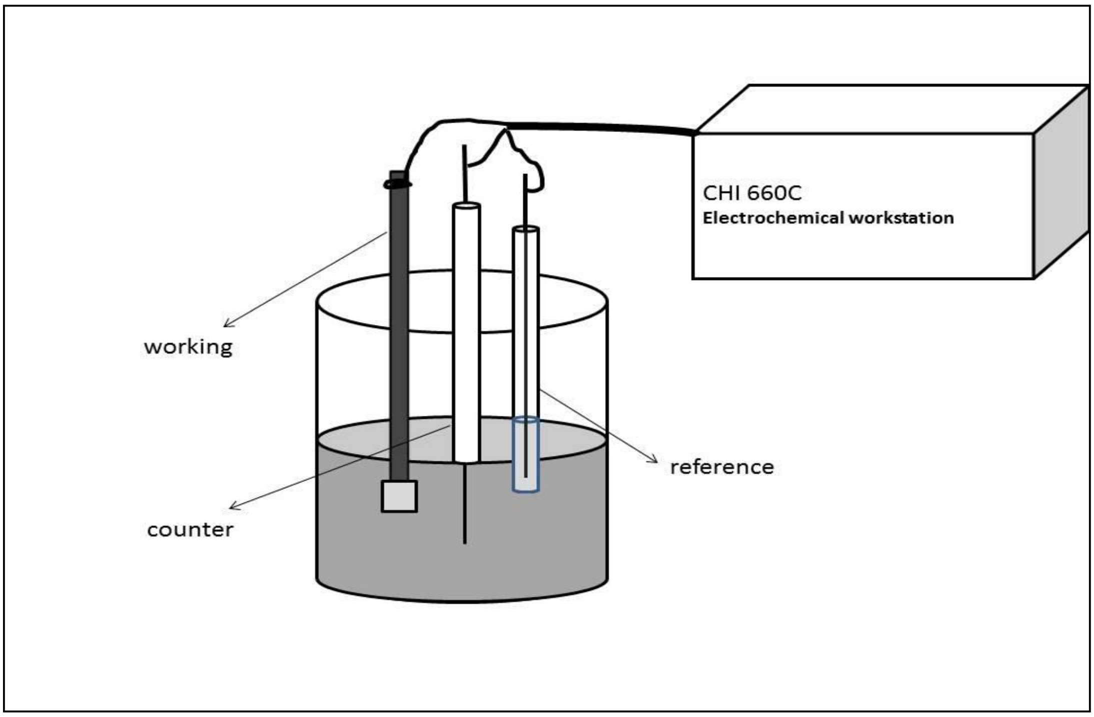

Fig.3.1: Schematic of set-up used in electrochemical deposition and analysis

Prior to deposition, ITO sheets (1 cm X 1 cm) were cleaned by sonication in acetone, ethanol, and distilled water for 10 minutes each and dried in air. Electrodeposition was carried out in a conventional three-electrode set up with ITO sheet used as working electrode, platinum wire as counter electrode and Ag/AgCl as reference electrode. The samples were fabricated by CV technique within a potential range from -1.2 to 1 V at a scan rate of 50 mV/s for 4 cycles using CHI 660C (CH Instruments, USA) electrochemical workstation. For the first set of synthesis, an aqueous solution comprising of 10 mM manganese acetate ($Mn(CH_3COO)_2$), 0.1 M Na_2SO_4 and 1 mM $HAuCl_4.3H_2O$ was used as the electrolyte and in the second case, the molar concentration of $Mn(CH_3COO)_2$ was increased to 0.1 M. The CV plots corresponding to the two sets of concentration will be presented subsequently.

For the comparison of morphological and structural properties, and to understand the influence of incorporated gold nanostructures on morphological and structural aspects, pristine Mn_2O_3 films were fabricated in the absence of $HAuCl_4$ in the electrolyte mixture, keeping all other conditions unchanged. Finally, after deposition, the samples were washed with distilled water, dried in air, and stored at room temperature for further characterizations.

Surface morphologies of all the samples were studied with both scanning electron microscopy (FESEM, FEI, INSPECT F50) and transmission electron microscopy (TEM, FEI, TF30, ST microscope operating at 300 kV) techniques. The TEM is equipped with a scanning unit and a high angle annular dark field detector from Fischione (model: 3000). Energy dispersive X-Ray spectroscopy (EDX) was used to identify the elements present in the samples. XRD (Bruker AXS D8), EELS (post column Gatan Quantum SE, model: 963 SE), XPS (Omicron Multiprobe Electron Microscopy System) with monochromatic Al Kα X-ray source (1486.7eV, model: XM 500) and Raman Spectroscopy (Microscope model: Olympus BX 41, TRIAX 550 JY spectrometer equipped with peltier cooled CCD detector Synapse, Horiba, JY) were performed at laser excitation wavelength of 488 nm for the identification of oxidation state of the Mn ions and the subsequent determination of the phase of the samples.

3.3 Co-electrodeposition (First Case): Results and Discussion

3.3.1. Structural characterizations:

3.3.1.1. X-Ray Diffraction:

X ray diffraction and its analyses was performed for the pristine and the composite samples to determine their phase. Fig.2. shows the comparative plot of the XRD patterns for the bare ITO sheet, pristine Mn_2O_3, and Mn_2O_3-Au composite, respectively. The diffraction peaks for ITO have been indexed, and are in good agreement with an earlier report [56]. The characteristic peak for Mn_2O_3 phase for the (222) plane [57] can be observed for the pristine and composite samples at about $2\theta \sim 33^o$. This is absent in the bare ITO sample, clearly indicating the formation of Mn_2O_3 phase in both the pristine and composite samples.

However, since no other characteristic peak could be observed, additional materials characterizations were necessary for confirming structural information about the samples. They have been discussed in the following paragraphs.

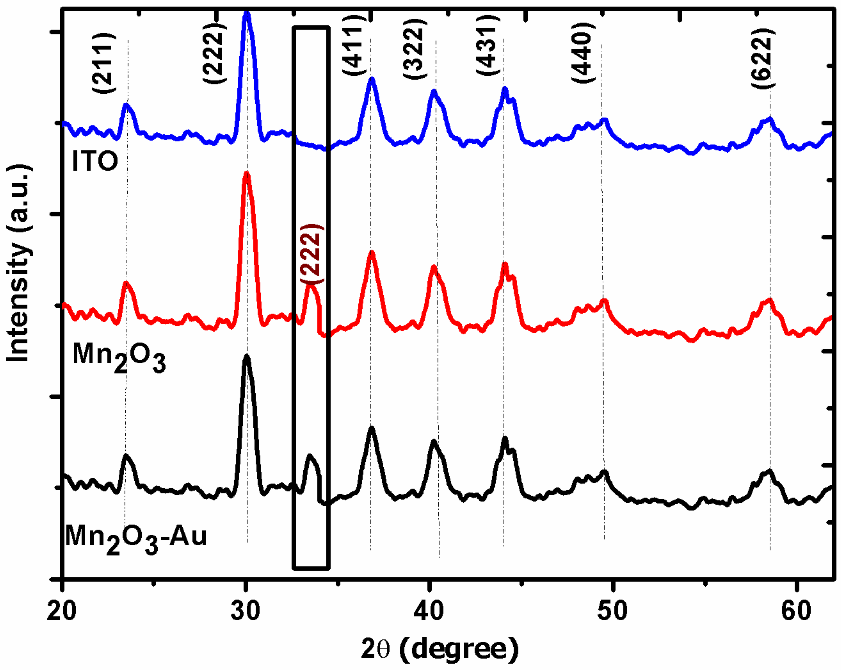

Fig.3.2: XRD patterns of bare ITO, pristine Mn_2O_3 and Mn_2O_3-Au composite

3.3.1.2. Electron Energy Loss Spectroscopy:

Electron energy loss spectroscopy (EELS) measurements were performed to determine the oxidation state of the Mn ions of the pristine and the composite samples. This technique is based on calculating the ratio of white line intensities corresponding to the $Mn\text{-}L_{2,3}$ edges ($I(L_3)/I(L_2)$) which depends on d electron occupancy and varies inversely with increasing oxidation state for Mn ions [58, 59]. From Figs.3.3(b) and 3.4(b) one can observe two sets of peaks in the plots corresponding to the oxygen-K (*O-K*) and manganese–$L_{2,3}$ ($Mn\text{-}L_{2,3}$) edges. The set of peaks for the $Mn\text{-}L_{2,3}$ edges, correspond to the transitions between $2p_{1/2}$ and $2p_{3/2}$ to the empty 3d orbitals. Among the various methods available for intensity ratio calculation, the one described by Pearson is followed for our analyses [60]. The intensity ratio values for the $Mn\ L_{2,3}$ edge of the pristine and the composite samples as obtained from Pearson method is listed in Table 1.

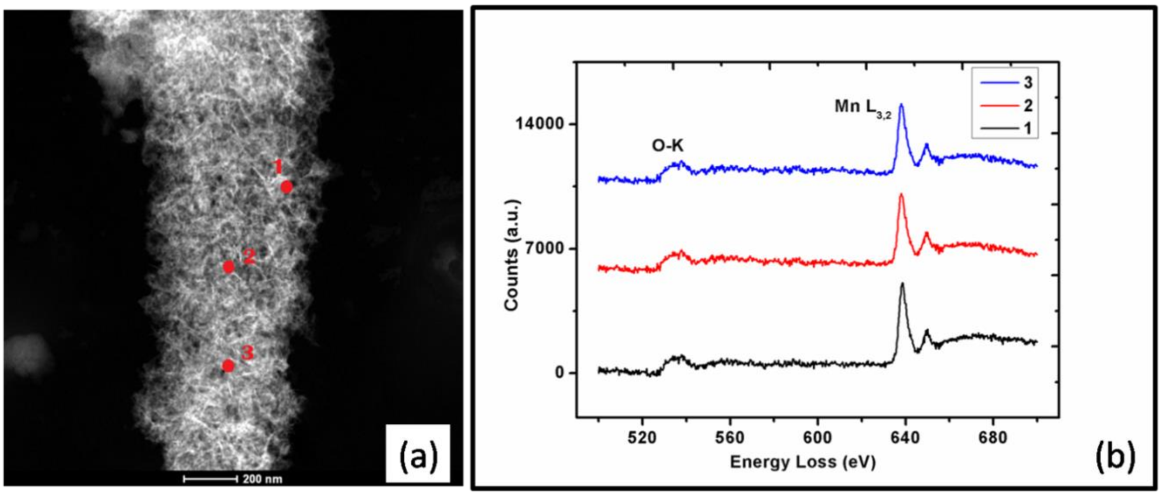

Fig.3.3: (a) STEM HAADF image of pristine Mn_2O_3 (b) corresponding EEL spectra of Mn_2O_3 at different probe points (1, 2, 3) as shown on the HAADF image.

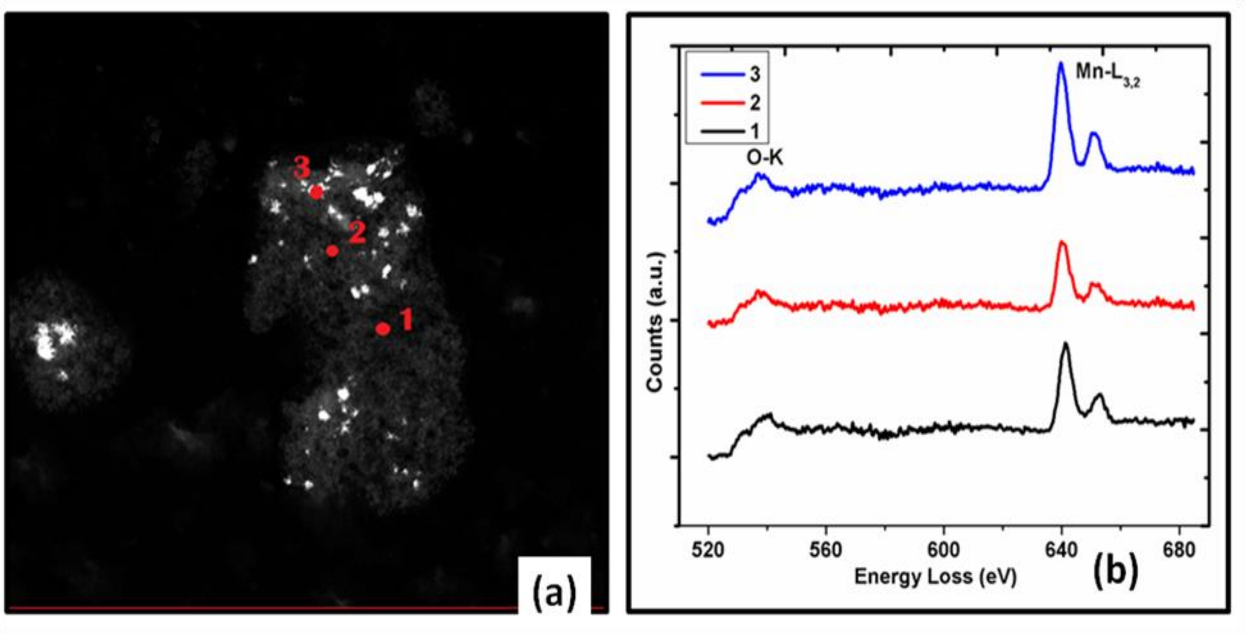

Fig.3.4: (a) STEM HAADF image of pristine Mn_2O_3-Au composite (b) corresponding EEL spectra of Mn_2O_3 at different probe points (1, 2, 3) as shown on the HAADF image.

Table1: EELS white line intensity ratios for pristine Mn_2O_3 and Mn_2O_3-Au composite

EELS Probe Position	$I(L_3)/I(L_2)$ for Mn_2O_3	$I(L_3)/I(L_2)$ for Mn_2O_3-Au
1	2.34	2.35
2	2.3	2.33
3	2.33	2.23

Upon comparison with the earlier reported values of white line intensity ratios of *Mn* $L_{2,3}$ [61, 62] the oxidation state of Mn ions matches reasonably well with that of Mn_2O_3 for both the pristine and composite samples.

3.3.1.3. X-Ray Photoelectron and Raman Spectroscopy Studies:

As an additional confirmation of the oxidation sate of the Mn ions in the two samples X-ray photoelectron spectroscopy (XPS) was conducted. Fig. 3.5 depicts the XPS core level spectra of Mn 2p and Mn 3s transitions. In the Mn 2p spectra of the pristine and the composite samples (Figs. 3.5(a) and (c)), the two peaks observed correspond to the Mn $2p_{3/2}$ and Mn $2p_{1/2}$ and their energy splitting value (ΔE) are obtained as 11.66 eV and 11.71 eV, respectively. These are in accordance with the values previously reported for Mn_2O_3 [61, 62]. However, this information is not entirely conclusive for confirming the oxidation state of the Mn ions [63] and therefore, Mn 3s core level spectra were analysed. The splitting in the Mn 3s spectra arises from the exchange interaction between the core 3s and unpaired 3d valance electrons causing photoelectron ejection [64]. The ΔE values of 5.4 eV and 5.44 eV for the Mn 3s splitting of the pristine and composite samples as shown in Fig 3.5(b) and 3.5(d) matches well with that of Mn_2O_3 [65, 66]. This further supports our previous conclusion that both the pristine as well as the composite samples are formed as Mn_2O_3.

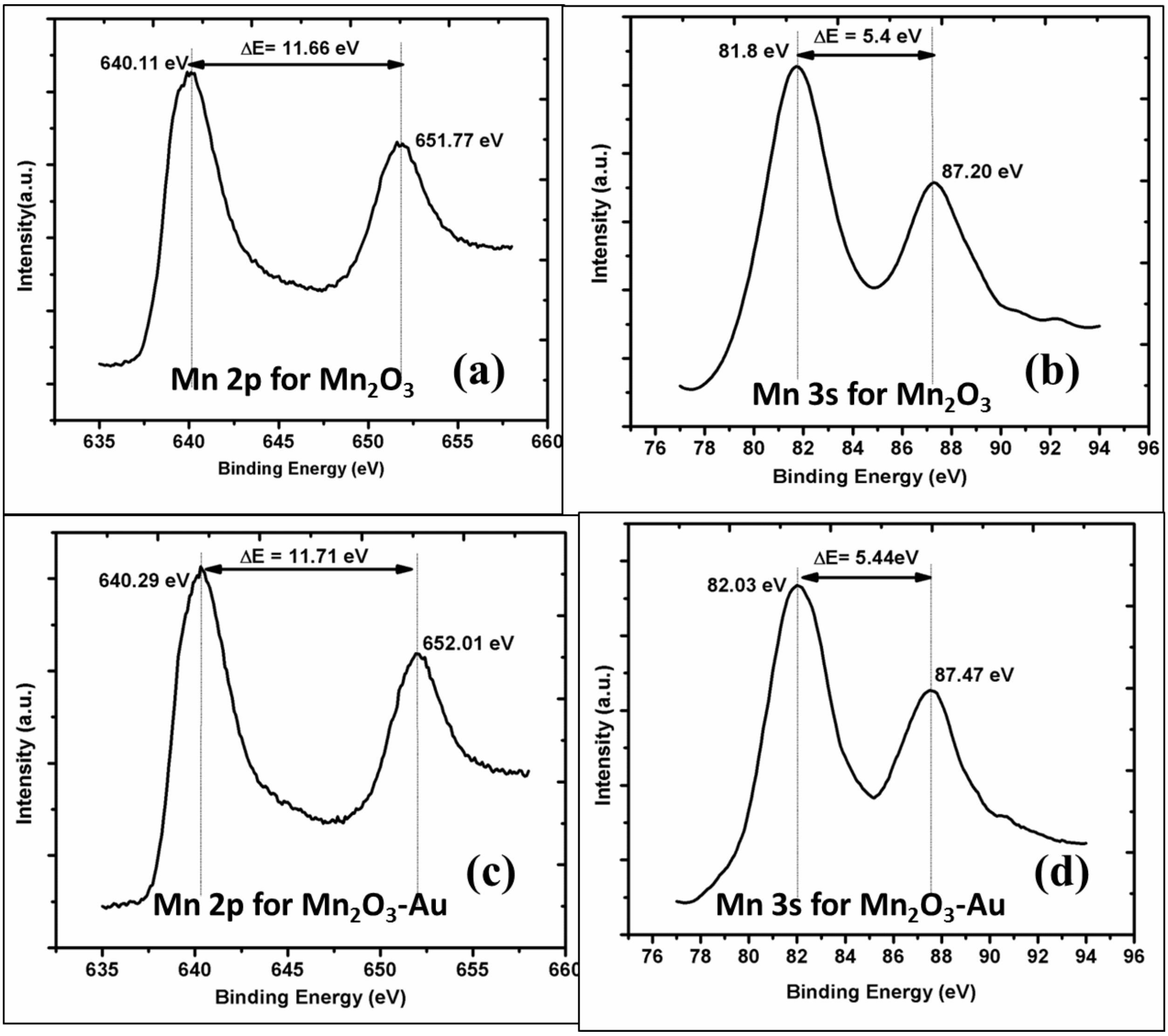

Fig.3.5: (a, c) Mn 2p and Mn 3s (b, d) X-ray photoelectron spectra of pristine Mn_2O_3 and Mn_2O_3-Au composite

Finally, Raman spectroscopy was performed (Fig. 3.6) for both the samples as a verification of all the previous results. The two peaks observed in the ranges 450-563 cm^{-1} and 630-647 cm^{-1} are characteristic of the asymmetric stretching of the bridge oxygen species (Mn-O-Mn) and symmetric stretching of the Mn_2O_3 groups respectively [67]. Hence, from the Raman analyses as well it is established that both the samples are formed with Mn_2O_3 phase.

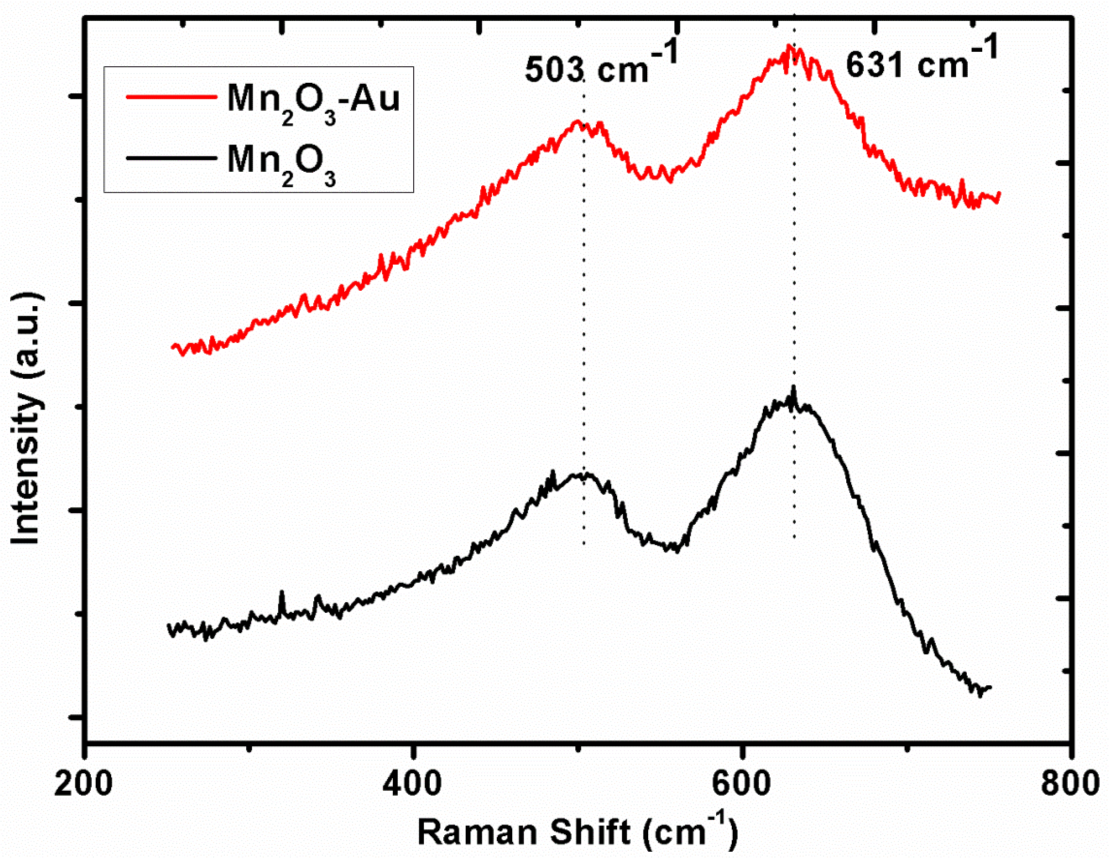

Fig.3.6: Raman Spectra of pristine Mn_2O_3 and Mn_2O_3-Au composite.

3.3.2. Morphological Characterization and EDX analysis:

The SEM images of both pristine Mn_2O_3 and Mn_2O_3-Au composite samples are shown in Fig.3.7(a)-(f). From the images of Figs.3.7(a)-(c), it is observed that Mn_2O_3 is deposited with a spongy mat like nanostructure on ITO while the SEM images of composite sample shown in Fig.3.7(d)-(f) depict microspheres of different sizes grown at certain places on the substrate. This feature is distinctly different from the pristine Mn_2O_3 samples which were electrodeposited in the absence of $HAuCl_4$ keeping all other conditions unchanged. Hence, it is evident, that incorporation of $HAuCl_4.3H_2O$, has a significant influence on the morphology of the electrodeposited manganese oxide film. However, since the SEM images were captured with gold coated samples, the corresponding EDX spectra would not be useful for investigating the presence of gold. For this purpose, detailed transmission electron microscopy (TEM) analysis along with energy dispersive X-ray (EDAX) studies were carried out.

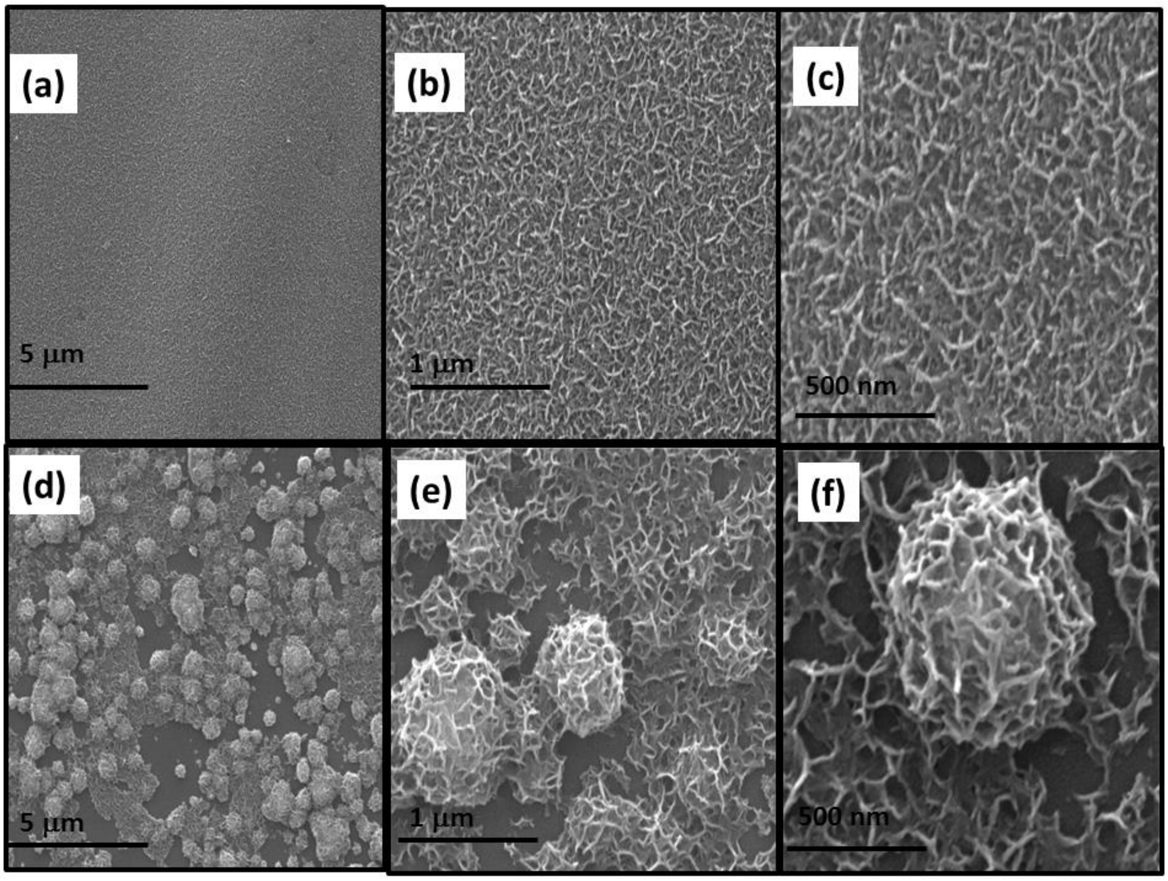

Fig.3.7: SEM images of pristine Mn_2O_3 spongy mat(a-c), and Mn_2O_3-Au nanocomposite(d-f)

Fig.3.8 depicts the STEM HAADF (high-angle annular dark-field scanning transmission electron microscopy) image of pristine Mn_2O_3 sample (a) and the corresponding EDX spectrum measured in the TEM mode (b). The presence of the elements Mn, O along with C, and Cu from the carbon coated copper grid are observed. Trace amounts of impurities i.e. Si, S, K, and Cl are also seen.

The EDX spectrum of the Mn_2O_3-Au composite microsphere, for the corresponding demarcated areas are shown in Figs. 3.9 (a) and (b). The presence of gold in the composite sample is clearly indicated with the measurement performed across the marked area. To confirm the homogeneity of the composite samples and verify the presence of gold in other

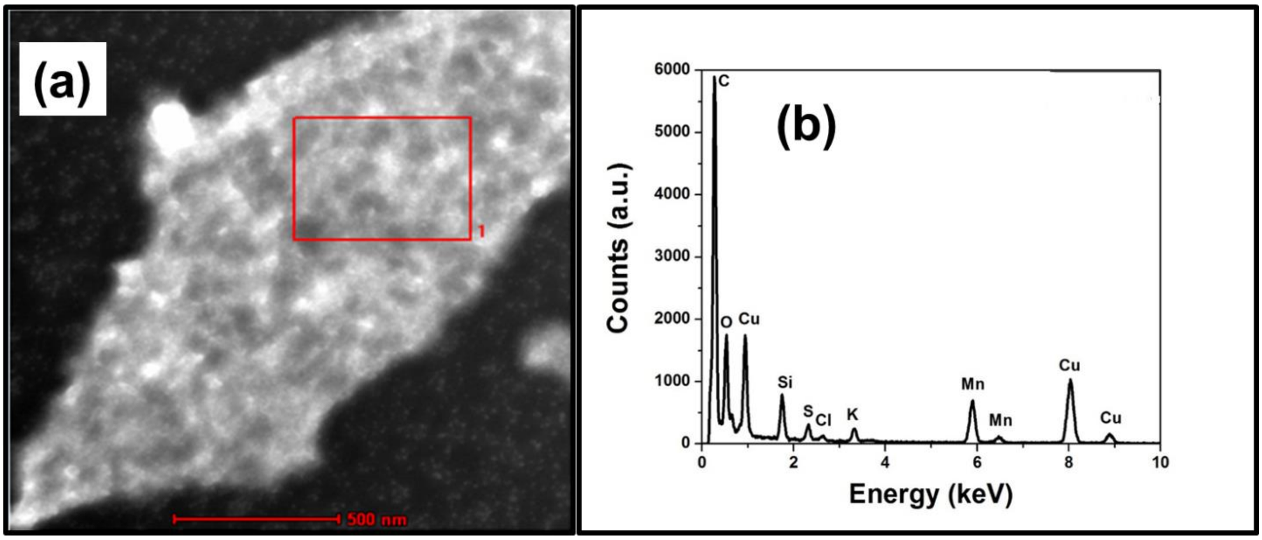

Fig.3.8: (a) STEM HAADF image of pristine Mn_2O_3 (b) selected area EDX of area marked

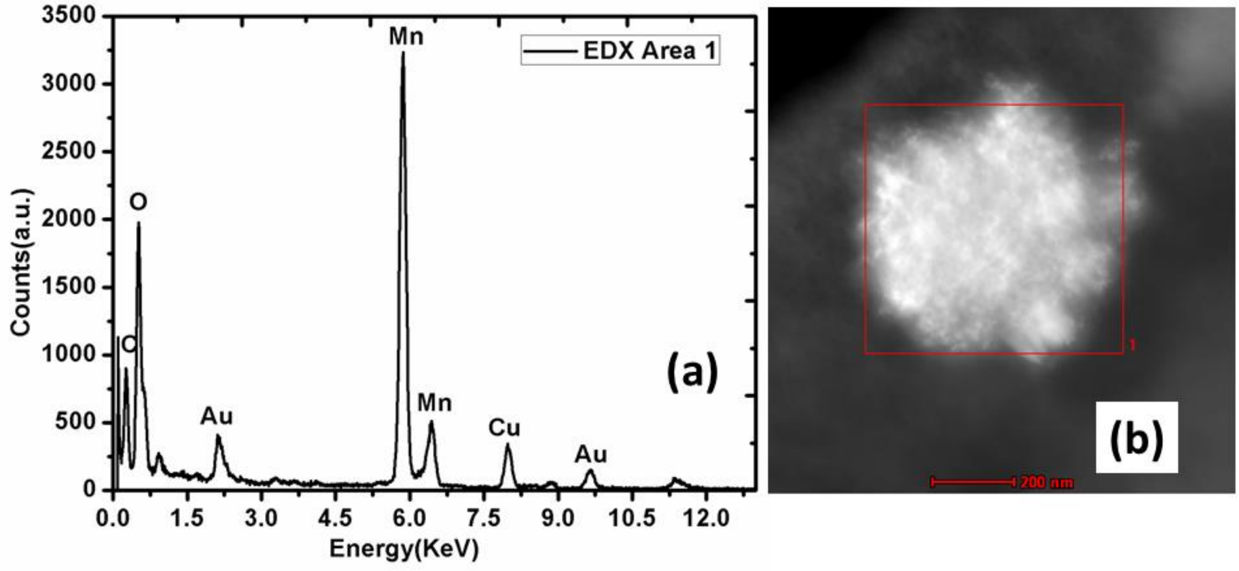

Fig.3.9: EDX spectrum of Mn_2O_3-Au microsphere (a) corresponding to area in STEM-HAADF image (b)

areas on the electrodeposited film, STEM-HAADF measurements along with EDX measurements performed on other locations of the electrodeposited composite film.

Fig. 3.10 depicts the STEM-HAADF images of two composite microspheres formed close to each other. It can be observed that these structures are slightly elliptical in shape indicating that the spherical microstructures formed on the co-electrodeposited composite film, are not of uniform shape across different locations on the sample surface. This inhomogeneity can be attributed to the variations in the morphology of the electrodeposition substrate.

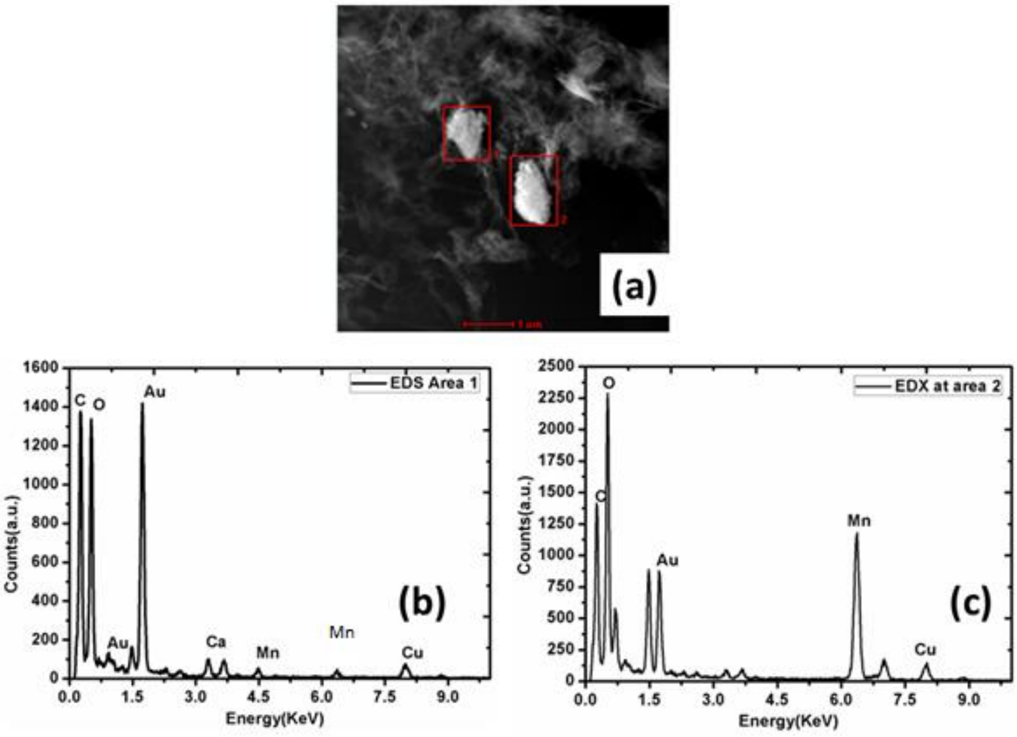

Fig.3.10: STEM-HAADF image of Mn_2O_3-Au composite (a) and EDX spectra (b & c) corresponding to the two regions marked for the composite microspheres

The STEM-HAADF image of Mn_2O_3-Au composite film depicting the two spherical structures are shown in Fig. 3.10 (a). The EDX spectra corresponding to the two regions marked in Fig. 3.10 (a) have been shown in Figs. 3.10 (b) and (c).

These measurements corresponding to the EDX spectra for the areas marked in Fig. 3.9 (b) and Fig. 3.10 (a) indicate the presence of gold on the spherical structures formed on the composite film. However, these images do not reveal whether the gold is present homogeneously within the spherical structure. To ascertain that, EDX measurement was performed at an arbitrary point on one of the spherical structures as shown in the STEM-HAADF of Fig.3.11 (b).

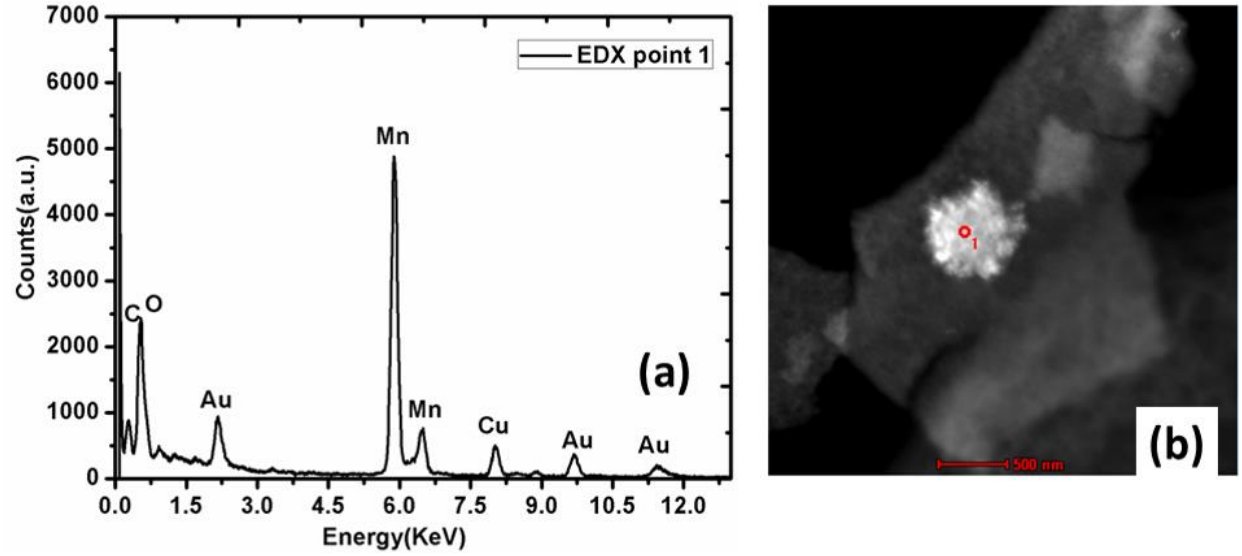

Fig.3.11: EDX analysis at a point on the composite sphere (a) and the corresponding STEM-HAADF image (b) (The Cu signal arises from the Cu TEM grid)

The EDX measurement shown in Fig. 3.11(a) corresponding to the point on the composite sphere as shown in Fig. 3.11(b) indicates the presence of gold at the specific point. This suggests that gold is present homogeneously in the composite sample on the spherical region. Furthermore, to determine about the presence of gold on regions outside the spherical structures, EDX measurement was performed as depicted in Fig.3.12. The STEM-HAADF image of Fig. 3.12(b) shows the point (outside the spherical microstructure) where the EDX measurement was performed. The EDX spectrum in Fig. 3.12(a), confirms the absence of gold outside the composite microsphere. This suggests, that perhaps the microspheres have been deposited around the gold nanostructures that were electrodeposited on the film.

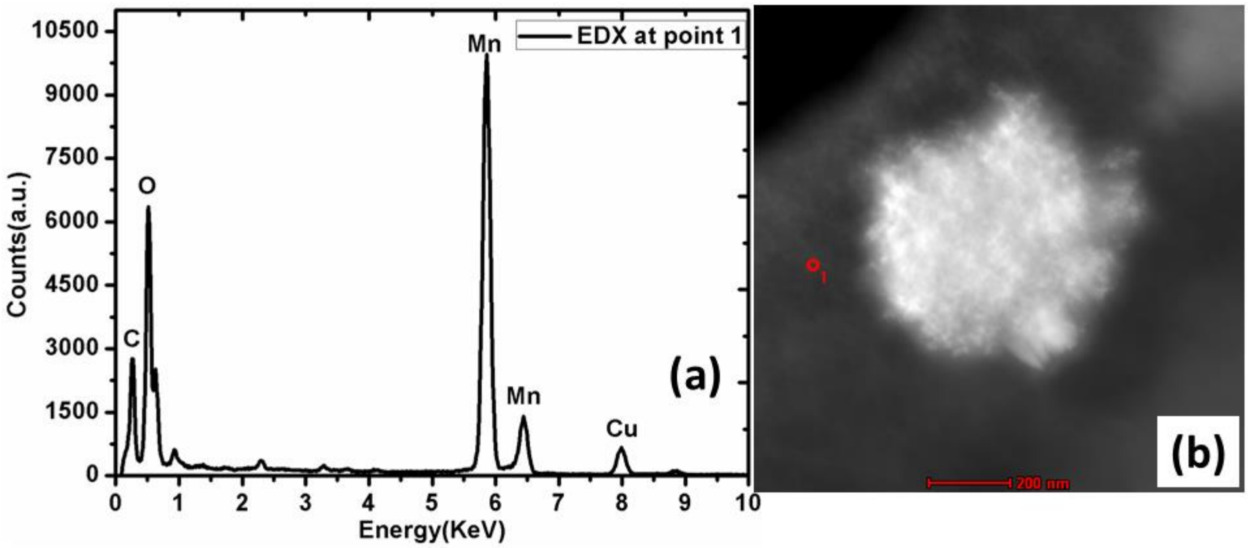

Fig.3.12: EDX analysis at a point outside the composite sphere (a) and the corresponding STEM-HAADF image (b) (The Cu signal arises from the Cu TEM grid)

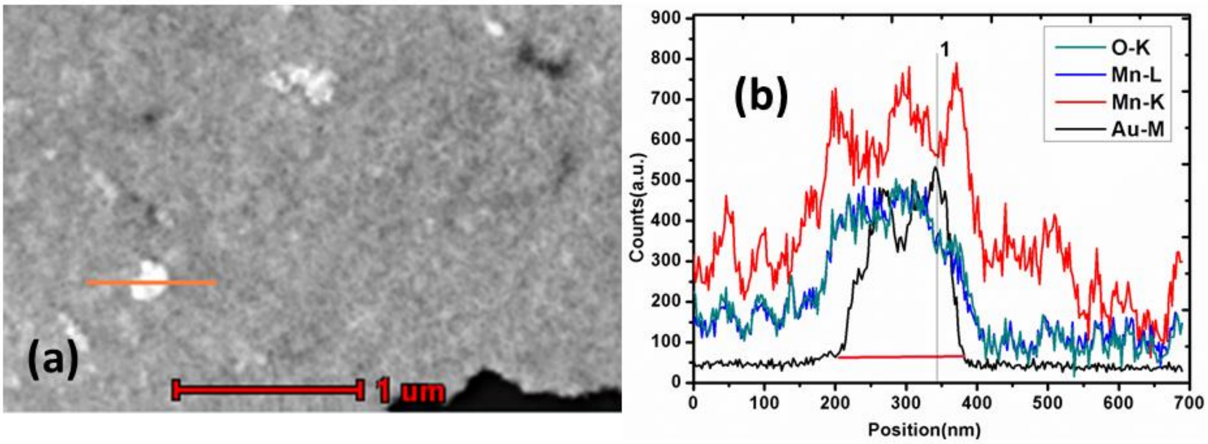

Fig.3.13: STEM -HAADF image for demarcating line profile (a) and the corresponding EDX line profile (b)

Additionally, an EDX line profile measurement was performed along the line marked in the STEM-HAADF image, i.e. Fig. 3.13(a). The EDX line profile as depicted in Fig. 3.13(b), indicates the presence of the elements along the line of scan. It can be seen, that the presence of manganese and oxygen is significant all along the line, even though, the signal is much stronger on the microsphere itself. In the case of gold, as the scan region deviates from the microsphere, the signal on the EDX line profile is completely diminished as indicated in Fig. 3.13 (b).

These detailed microscopy analyses performed with TEM, suggests that besides a distinct morphological difference between the pristine Mn_2O_3 and co-electrodeposited Mn_2O_3-Au composite sample, the presence of gold in the composite thin film is confined to the spherical microstructures.

Based on this conclusion, a systematic step by step study was performed to analyse the formation mechanism of these microsphere structures. Experiments were performed by conducting co-electrodeposition CV at different voltage ranges, and recording the SEM images of the co-electrodeposited samples obtained for the corresponding voltage ranges.

3.3.3. Formation Mechanism of Mn_2O_3-Au composite sphere:

To obtain a basic understanding of the co-electrodeposition process, let us look at the comparative CV plots for the pristine and co-electrodeposited samples as shown in Fig.3.14. Fig. 3.14 (a) shows a plot of the two voltammograms, the black one corresponding to the deposition of pristine manganese oxide and the red curve corresponds to the manganese oxide-gold co-electrodeposited sample. After a careful investigation of the two deposition CVs one can identify the difference of the CV curves between -1.2 to -0.5 V (shown separately in Fig.3.14(b)) while the rest of the plots being nearly identical. Hence, it can be concluded that this region corresponds to the deposition of gold in the co-electrodeposition process. In the potential region between -0.2 to 1 V, the two anodic and cathodic peaks are observed. The two anodic peaks in Fig. 3.14(a) are attributed to the oxidation of Mn^{2+} to Mn^{3+} and Mn^{3+} to $Mn(OH)_3$. With the increase in the scan number, the steady increase in the current densities corresponding to the two oxidation peaks indicates the formation of an Mn_2O_3 film. The details of the reactions involved in Mn_2O_3 formation can be proposed through an electron transfer–chemical reaction–electron transfer (ECE) mechanism as expressed in eqn (1)–(6). A similar ECE mechanism was reported in the case of MnO_2 formation [64]. In the CV plot of co-electrodeposition, the region near the initial negative voltage scan corresponds to the onset of gold nucleation. The peak at -0.67 V could be due to the oxidation of the as deposited Au particles. However, the Au deposition further takes place in the reduction cycle near -1.1 V which is consistent with our previous report [65]. There is an increase in the reduction current near -1.1 V during the successive scans, whereas, the same potential region of the electrodeposition CV of pristine Mn_2O_3 (black curve) is flat and almost overlaps with the successive CV scans. Increase in current during successive CV scans (four cycles) is in agreement with both, the cathodic deposition of gold (green arrow in Fig.3.15(c)) and anodic deposition (shown by two upward arrows in Fig.3.15(b)) of Mn_2O_3 on the ITO substrate. These aspects have been explained in detail in the following paragraph along with the schematic.

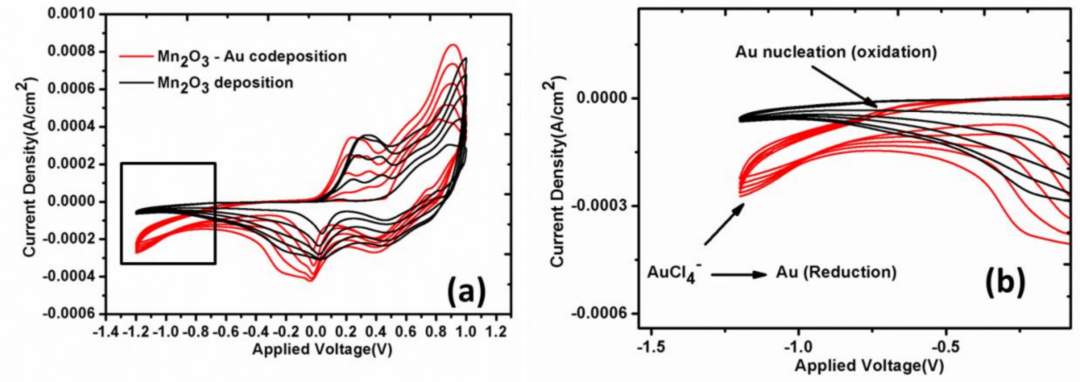

Fig.3.14: (a) Comparative CV of electrodeposition of Mn_2O_3 and Mn_2O_3-Au between -1.2 to 1 V at scan rate of 0.06V/s, (b) enlarged image highlighting Au deposition

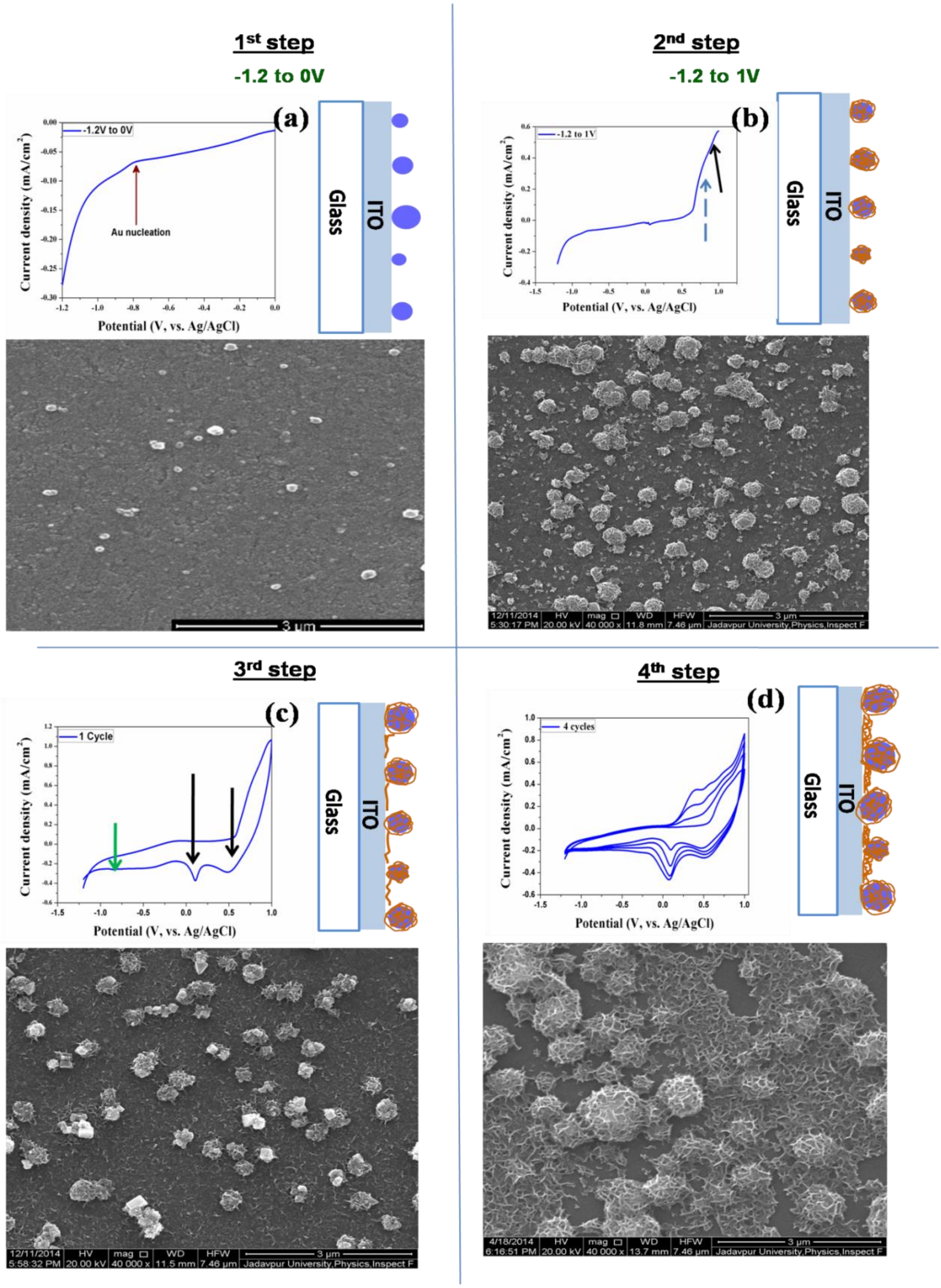

Fig.3.15: Formation Mechanism of composite microsphere and stepwise co-electrodeposition CV along with corresponding SEM images for the voltage ranges (a) -1.2 to 0 V, (b) -1.2 to 1 V, (c) one complete cycle from -1.2 to 1 V, (d) entire deposition process for 4 cycles between -1.2 and 1 V

The mechanism behind the formation of the composite sphere is demonstrated schematically in Fig.3.15. Herein, we have introduced a step by step formation schematic of the composite sample. Additionally, we have incorporated the SEM image at each step. The detailed growth study of Mn_2O_3-Au composite sample has been described in four steps performed by CV technique at three potential ranges (-1.2 to 0 V, -1.2 to 1 V and one full cycle starting from -1.2 V). Each step of the schematic corresponds to the study of the growth of the composite in the respective potential range. When potential scan starts from -1.2 V and goes up to 0 V (at 1st step of schematic) for the CV shown in Fig.3.15(a), the onset of Au nucleation begins at negative potentials, and a small peak at around -0.6 V may correspond to the oxidation of the as deposited Au particles, as indicated with the arrow in Fig.3.15(a), even though the deposition proceeds at more negative potentials (during the reduction segment, Fig 3.15(c)).In the corresponding SEM image of the Fig.3.15(a), we observe some Au particles on the ITO substrate.

During the 2nd step (-1.2 to 1 V), transformation of Mn^{2+} to Mn^{3+} occurs first through electron transfer reaction which is indicated in the CV by the blue dashed upward arrow in Fig. 3.15(b). Subsequently, these Mn^{3+} ions are oxidized and form Mn_2O_3 (solid arrow) which aggregate and deposit predominantly on Au particles resulting in the sphere formation (as clearly seen in the SEM image of 2nd step) driven by the minimization of total surface energy. A possible sequence of chemical reactions resulting in the formation of Mn_2O_3 (2nd step) is proposed as follows:

$$Mn^{2+} \longrightarrow Mn^{3+} + e^{-} \text{ (blue dashed arrow)} \qquad (1)$$

$$Mn^{3+} + 3H_2O \longrightarrow Mn(OH)_3 + 3H^{+} + 3e^{-} \text{ (black solid arrow)} \quad (2)$$

$$2Mn(OH)_3 \longrightarrow Mn_2O_3 + 3H_2O \qquad (3)$$

Moreover, Mn_2O_3 flakes are also observed outside the sphere in SEM image of Fig.3.15(c). In the cathodic cycle, (i.e. 1 to -1.2 V) two events happen consecutively: first, reduction of some of the Mn_2O_3 (shown clearly by black downward arrow in the CV of 3rd step, Fig.3.15(c)) particles and cathodic deposition (indicated by green color downward arrow) of Au. Consequently, one can distinguish the morphological change of Mn_2O_3-Au composite sample by two SEM images which were captured before (at 2nd step) and after reduction (at 3rd step) of Mn_2O_3. By observing the SEM image in 3rd step, some indication of Mn_2O_3 sheet formation is observed. This entire process (1st, 2nd and 3rd step) takes place within one complete cycle of the CV.

The possible reaction mechanisms occurring during the cathodic cycle of the 3rd step are proposed as follows:

$$Mn_2O_3 + 3H_2O \longrightarrow 2Mn(OH)_3 \quad (4)$$

$$Mn(OH)_3 + 3H^+ + 3e^- \longrightarrow Mn^{3+} + 3H_2O \text{ (blue dashed arrow)} \quad (5)$$

$$Mn^{3+} + e^- \longrightarrow Mn^{2+} \text{ (black solid arrow)} \quad (6)$$

$$AuCl_4^- + 3e^- \longrightarrow Au + 4Cl^- \text{ (green arrow)} \quad (7)$$

At the 4th step, the composite sample is allowed to grow in the same manner for four CV cycles and we obtain the resulting Mn_2O_3-Au composite sphere on Mn_2O_3 sheet as shown in SEM image of Fig.3.15 (d).

3.4 Co-electrodeposition (second case): Results and Discussion

For the second set of co-electrodeposited samples, the pristine Mn_2O_3 was deposited using aqueous 0.1 M manganese acetate ($Mn(CH_3COO)_2$) and 0.1 M sodium sulfate (Na_2SO_4) solution while Mn_2O_3-Au was grown by adding 1 mM aurochloric acid ($HAuCl_4$) to the above electrolyte mixture. The pH of the mixed electrolyte was maintained to be the same (~7) and the same growth condition was maintained during the synthesis of both pristine Mn_2O_3 and composite Mn_2O_3-Au samples.

Fig. 3.16 shows the typical CV curves of both Mn_2O_3 and Mn_2O_3-Au, electrodeposited on ITO. The CV curves corresponding to 4 cycles of deposition process of pristine Mn_2O_3 on the ITO surface immersed in electrolyte mixture (pH~7) containing aqueous Na_2SO_4 and $Mn(CH_3COO)_2$ is depicted in Fig. 3.16(a). Similar to the co-electrodeposition for the first set of electrolyte concentration, in this case the two anodic peaks ($P1_a$, $P2_a$) in Fig. 3.16(a) are attributed to the oxidation of Mn^{2+} to Mn^{3+} and Mn^{3+} to $Mn(OH)_3$. With the increase of scan number, the successive increase in the oxidation peak current values, indicates the formation of Mn_2O_3 film. Since, the structure of the pristine and composite films of manganese oxide are both Mn_2O_3 (as will be discussed subsequently), the previously discussed set of chemical reactions can be applicable in the present case as well.

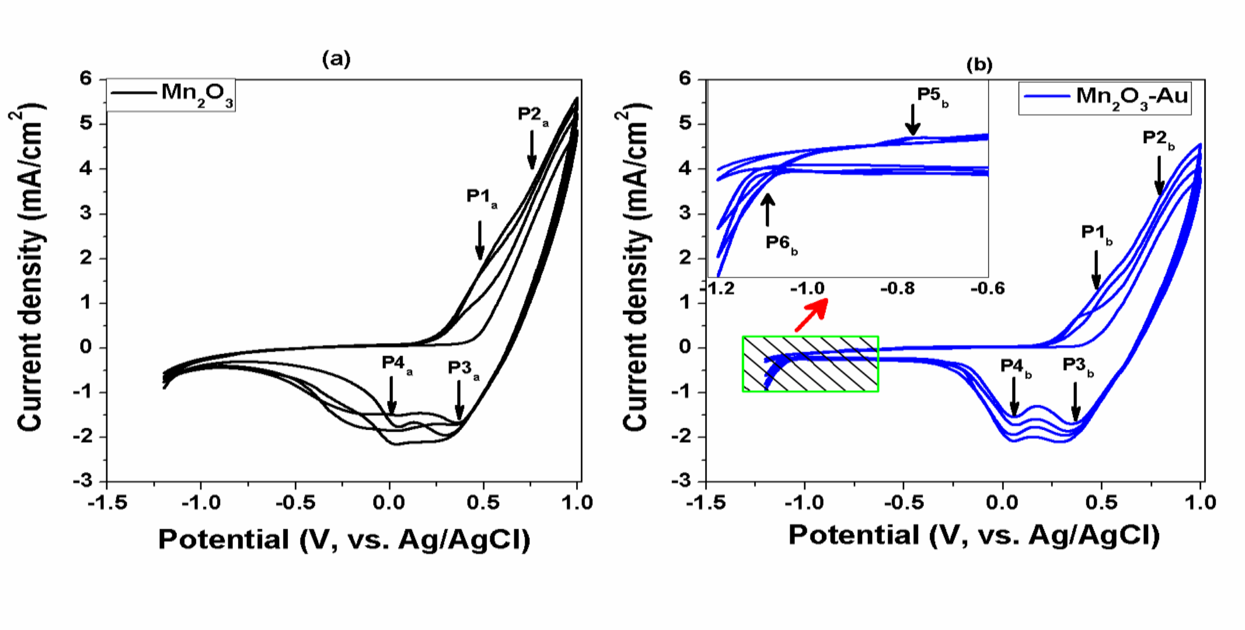

Fig.3.16: Comparative CV graphs for the electrodeposition of both (a) Mn_2O_3 and (b)Mn_2O_3-Au

3.4.1. Morphological and Elemental Analysis:

Fig. 3.17(a) and 3.17(b) show the scanning electron microscopy (SEM) images of both pristine Mn_2O_3 and Mn_2O_3-Au samples grown in same pH of the electrolyte. It can be seen from SEM images that the morphology of both the samples are distinctly different. From Fig. 3.17(a) we can say that the Mn_2O_3 film has smooth wrinkles whereas, rough wrinkles and more porous film is observed in Fig. 3.17(b) for the Mn_2O_3-Au sample. One can clearly observe, that the morphologies of the pristine and the composite sample are entirely different from the first set of samples (as shown in Fig. 3.7). The disappearance of the microspheres from the composite film can be noted. This suggests the significance of the molar concentration of electrolyte precursors in the electrodeposition process. These aspects have been discussed later in this chapter.

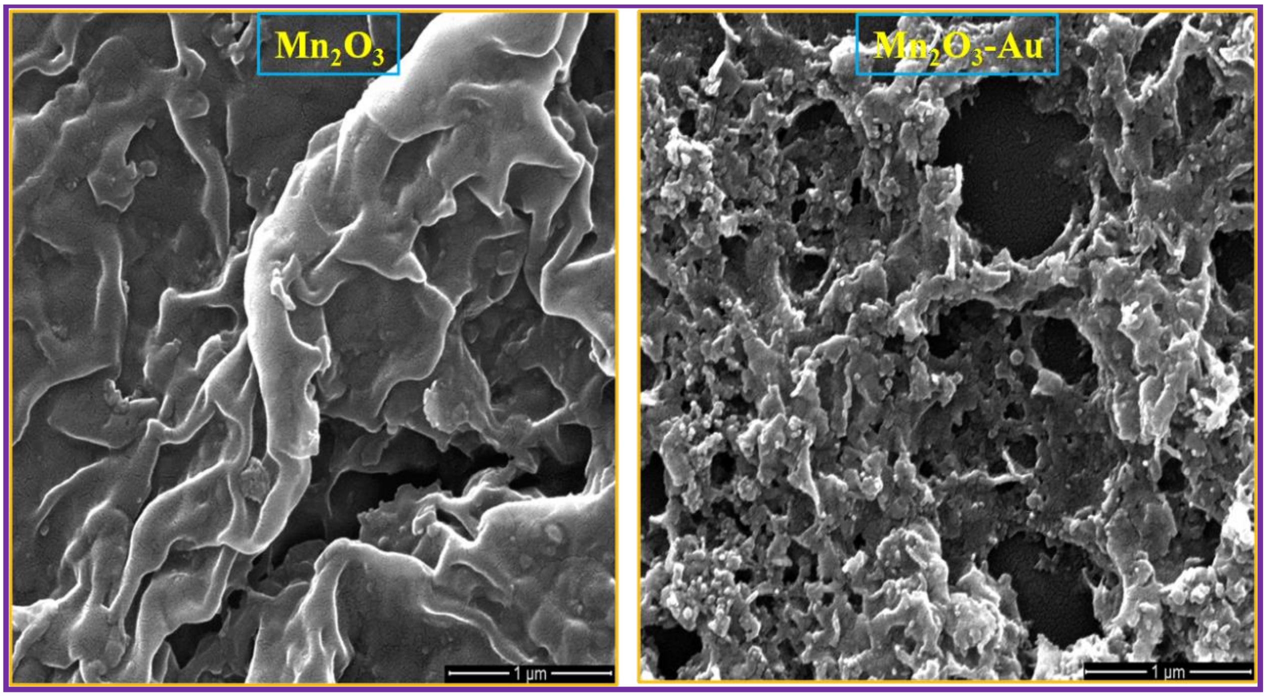

Fig. 3.17: SEM image of (a) Mn_2O_3 (b) Mn_2O_3-Au composite sample

However, from the secondary electron image (Fig. 3.17(b)) it was hard to find any evidence of Au on the surface of Mn_2O_3. The probable reason of this might be the Au embedded inside the Mn_2O_3 matrix owing to the higher concentration of manganese acetate (0.1 M) used in this co-electrodeposition process. To investigate this aspect further, detailed morphological, structural, and crystallinity information of the samples were analyzed using transmission electron microscopy (TEM). By applying EELS measurement, the spectroscopic analyses of the samples were performed, in the TEM mode. Figs. 3.18(a)-(c) and Fig. 3.19(a)-(e) represents the TEM analysis of as prepared pristine Mn_2O_3 and Mn_2O_3-Au composite samples respectively. Fig. 3.18(a) is the TEM image and Fig. 3.18(b) represents STEM-HAADF image of Mn_2O_3. Electron diffraction pattern of pristine Mn_2O_3 is shown in the inset of Fig. 3.18(a), which shows the presence of nano-crystallites and the diffraction planes of the sample are indexed on the inset SAED pattern (see inset). Indeed, the high-resolution TEM image of Fig. 3.18(c) shows such crystallites besides the presence of high rippling and the edge of ripple can also be observed in the HRTEM image. Fig. 3.19(a) corresponds to the TEM image of Mn_2O_3-Au composite sample. The presence of urchin like gold nanostructure embedded in Mn_2O_3 matrix can be clearly observed. EDX spectrum from area '1' of the STEM-HAADF image of Fig. 3.19 (b) is shown in Fig. 3.19(c) confirms the elemental composition of the same sample. Cu and C signal in EDX spectrum is due to carbon coated Cu grid used for TEM study. Chemical mapping using STEM-HAADF-EDX technique of individual component of Mn_2O_3-Au composite sample from area 2 (see Fig. 3.19(b)) is shown in the Fig. 3.19(d).

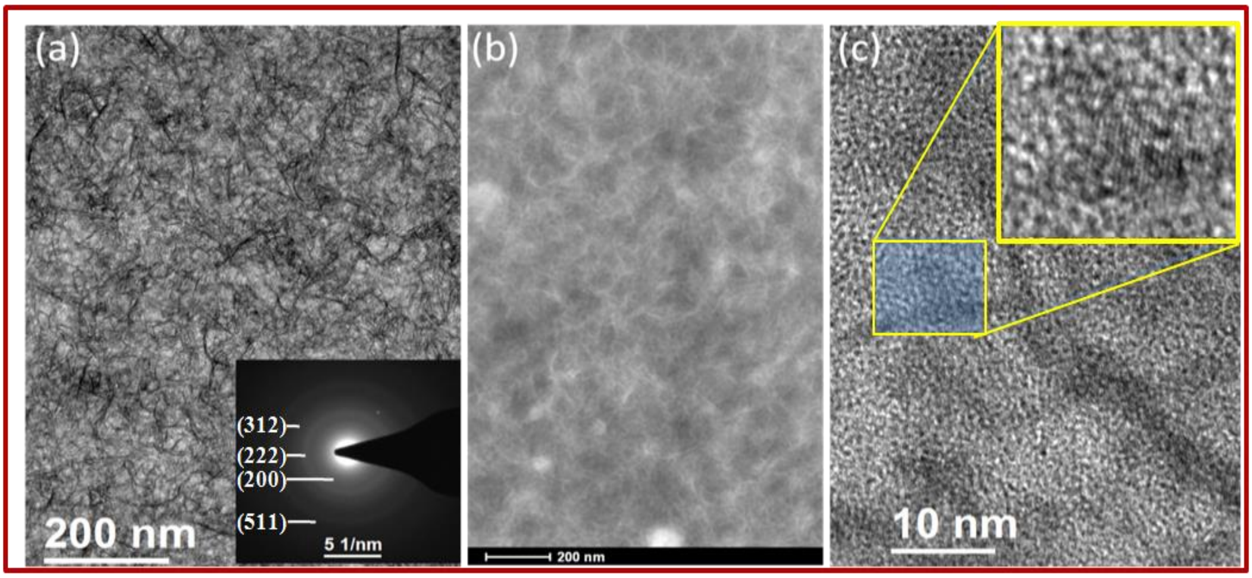

Fig. 3.18: (a) Bright-field TEM image, (b) STEM-HAADF image (c) HRTEM image of Mn_2O_3 *sample and in the inset showing nanocrystals.*

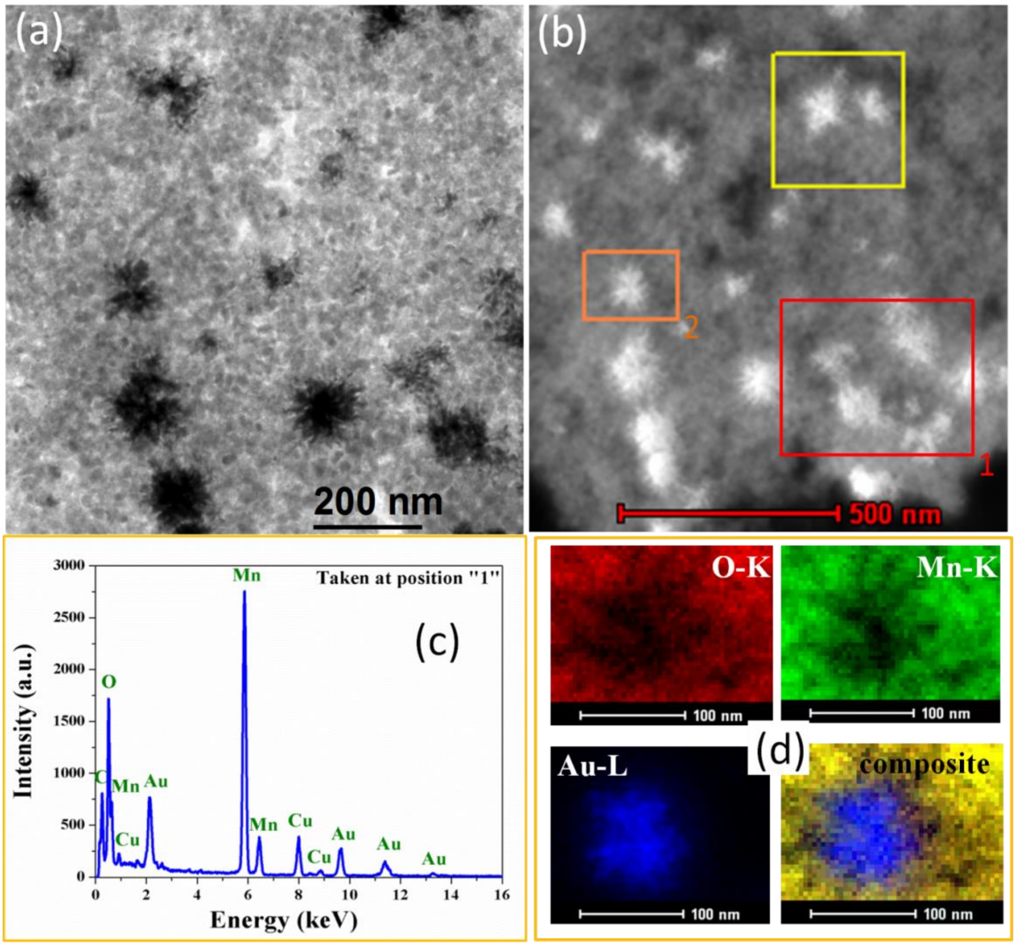

Fig. 3.19: (a) TEM image (b) STEM-HAADF image, (c) EDX spectrum, (d) Elemental mapping. (The Cu signal arises from the Cu TEM grid)

Both electron diffraction pattern and HRTEM image of individual Mn_2O_3 matrix (marked with red dotted circle ‘1’) and Au with Mn_2O_3 (marked with red dotted circle ‘2’) is depicted in Fig. 3.20. HRTEM of Mn_2O_3 matrix confirms that crystals are formed and well-defined electron diffraction pattern is ascribed. Same observation is also found in the case of Au nanostructures embedded Mn_2O_3 samples. Both electron diffraction pattern and HRTEM image of individual Mn_2O_3 matrix (marked with red dotted circle ‘1’) and Au with Mn_2O_3 (marked with red dotted circle ‘2’) is depicted in Fig. 3.20. HRTEM of Mn_2O_3 matrix confirms the crystals are formed and well-defined electron diffraction pattern is ascribed. Same observation can be made in the case Au nanostructures embedded Mn_2O_3 sample. The diffraction spots can be indexed as (200), (222), (312), and (511) reflections of cubic α-Mn_2O_3 (JCPDS 71-0635) from dotted circle ‘1’ whereas diffraction spots can be indexed as (200), (122), (222), and (312) reflections of cubic α-Mn_2O_3 (JCPDS 71-0635) from dotted circle ‘2’ with Au (111) spot. The HRTEM images show the presence of such nanocrystals. The inter planer spacing (d-spacing) 4.71 Å in Fig. 3.20- ii could be attributed to (200) of α-Mn_2O_3 and d-spacing of 2.31 Å in Fig.3.20- iii due to (111) of Au (d_{200} for α- Mn_2O_3 is 4.70 Å and d_{111} for Au is 2.35 Å.).

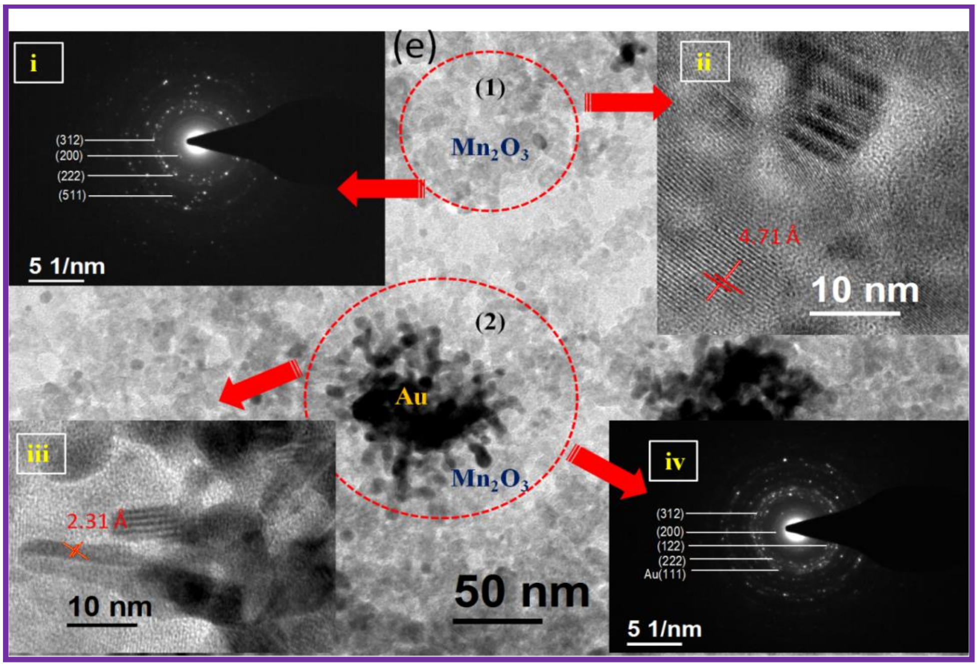

Fig. 3.20: SAED and HRTEM images from different area of Mn_2O_3-Au composite sample

3.4.2. Structural analysis of pristine Mn_2O_3 and Mn_2O_3-Au composite:

XRD analysis of the as deposited samples (both pristine Mn_2O_3 and Mn_2O_3-Au composite) including bare ITO is shown in the Fig. 3.21. Though both the samples are thin films (thickness~400 nm), the corresponding diffraction peak of the materials itself is not so prominent. A small peak around $2\theta \sim 33^o$ (encircled with dotted rectangular region) is attributed to the main characteristic feature of (222) plane of Mn_2O_3 phase of the sample. The same feature has also been reported in the recently published article by A. Ramírez et al. [57]. Both pristine and composite sample were grown in the same phase as confirmed by the (222) plane of XRD analysis. This aspect matches with observation made in the case of the pristine and composite samples for the first set of co-electrodeposition.

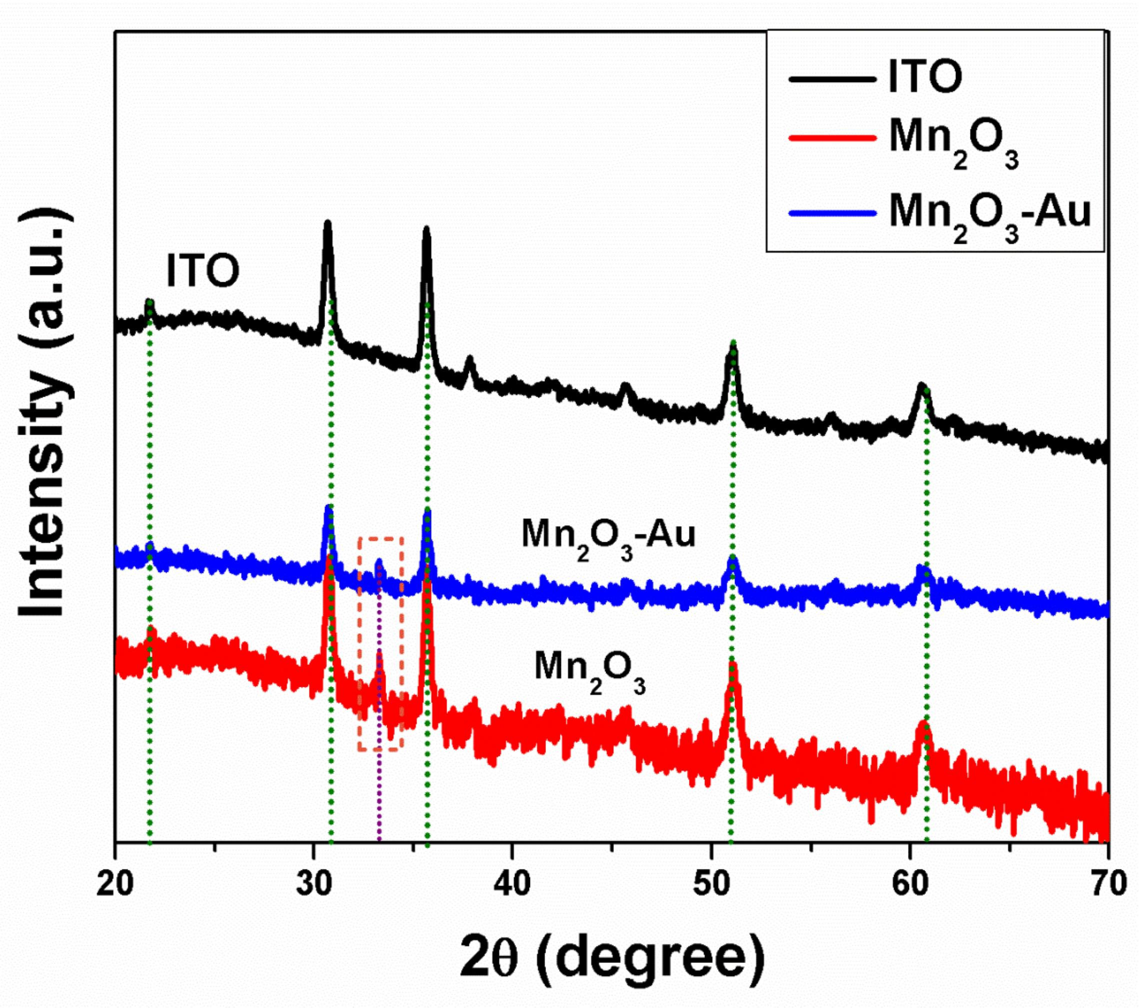

Fig. 3.21: XRD analysis of both pristine Mn_2O_3 and Mn_2O_3-Au composite sample

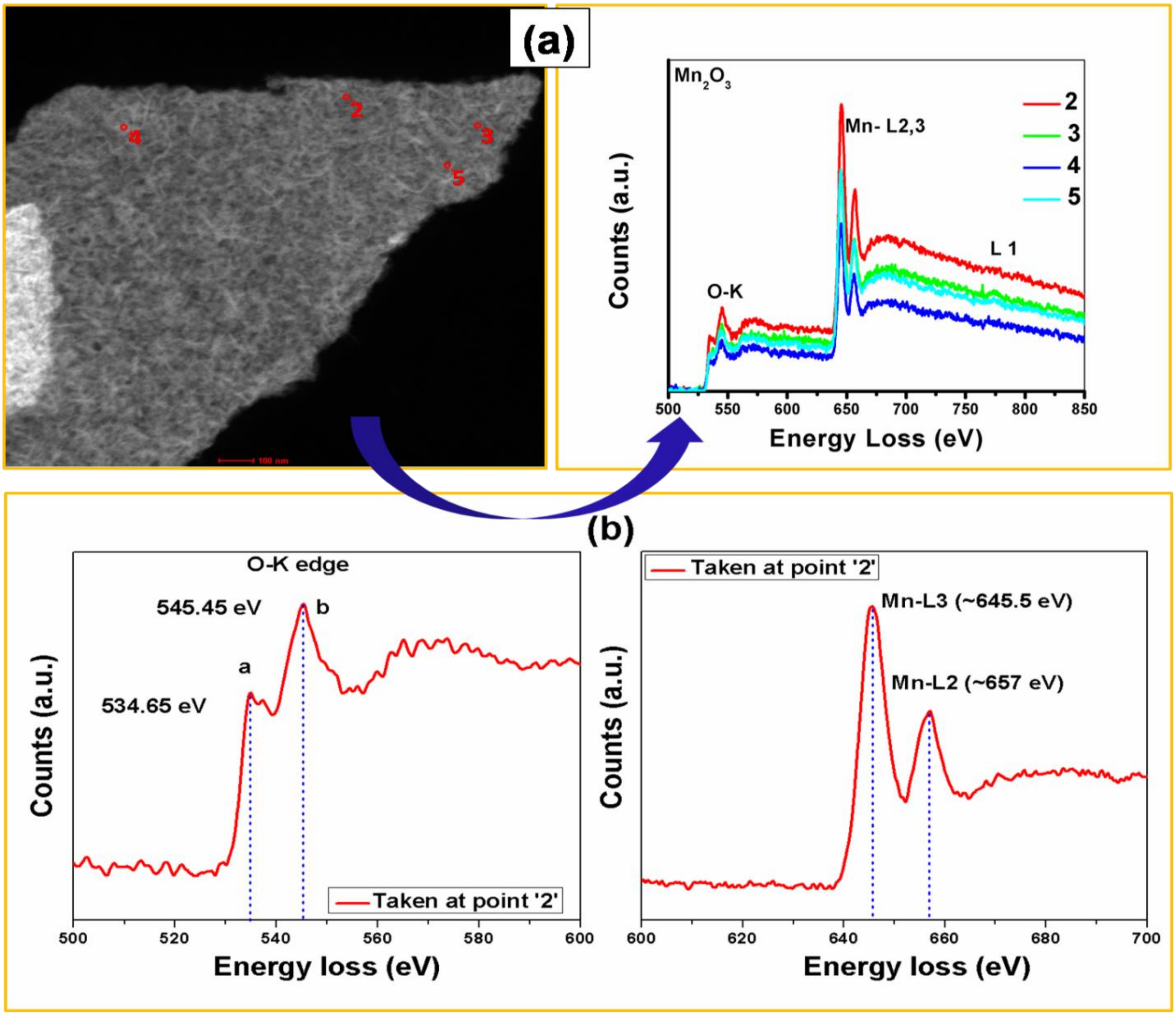
(a)
2
3
4
5
100 nm
Mn_2O_3
Mn- L2,3
L 1
O-K
2
3
4
5
Counts (a.u.)
Energy Loss (eV)
500
550
600
650
700
750
800
850
(b)
O-K edge
545.45 eV
b
a
534.65 eV
Taken at point '2'
Counts (a.u.)
Energy loss (eV)
500
520
540
560
580
600
Taken at point '2'
Mn-L3 (~645.5 eV)
Mn-L2 (~657 eV)
Counts (a.u.)
Energy loss (eV)
600
620
640
660
680
700

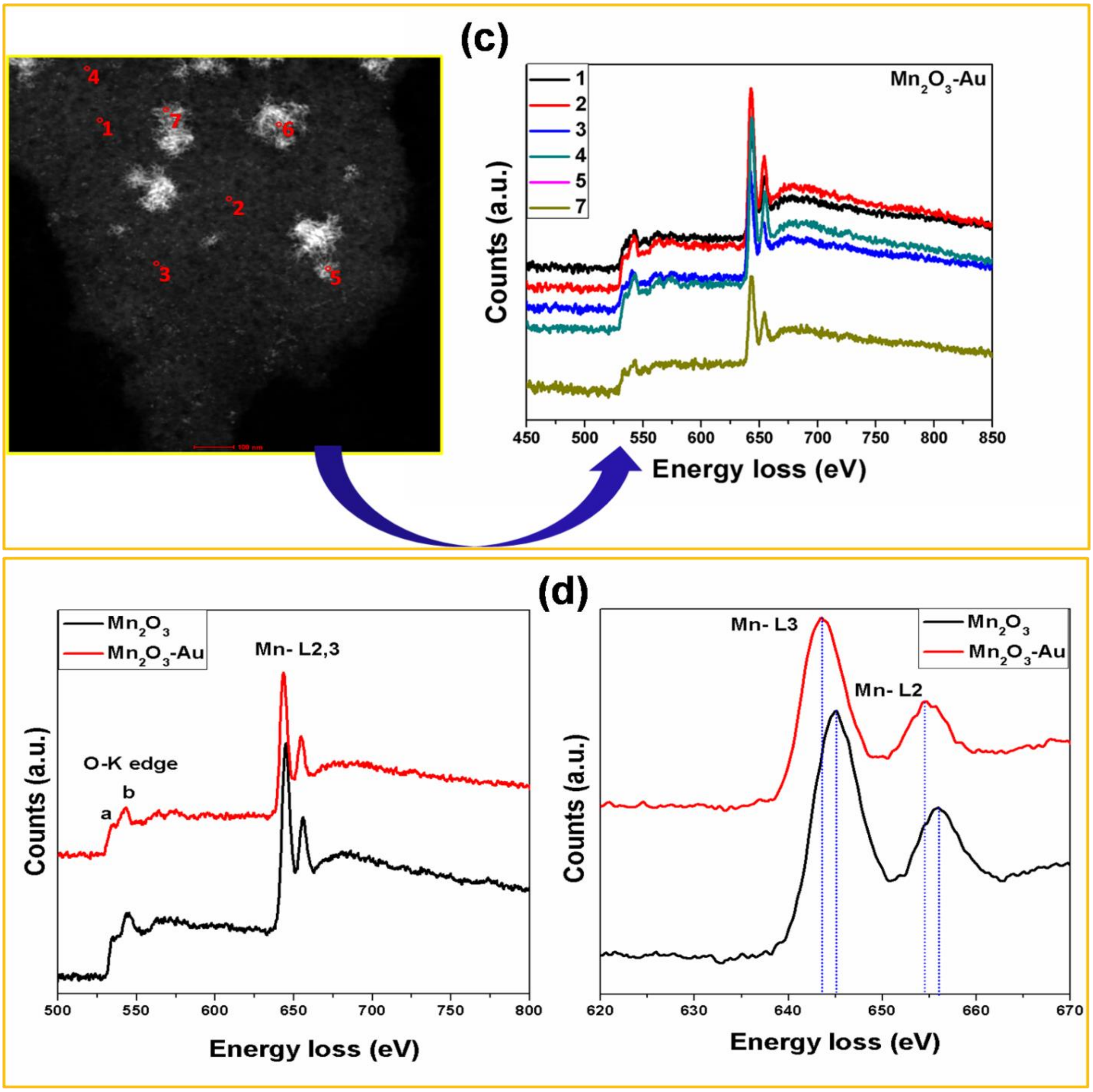

Fig. 3.22: (a) HAADF image (left) and corresponding EELS spectra of pristine Mn_2O_3 at different probe points (b) separate O-K edge and Mn $L_{2,3}$ graph of EELS of single probe point '2' (c) HAADF image (left) and corresponding EELS spectra of at different probe points Mn_2O_3-Au and (d) Comparative analysis of EELS spectra of both pristine Mn_2O_3 and Mn_2O_3-Au (left) and Mn-L2,3 edges (right).

Similar to samples obtained from the first set of co-electrodeposition, in the present case as well, EELS technique has been used to determine the oxidation state. The EEL spectra of the pristine Mn_2O_3 on different points (probe size ~ 1 nm) on the sample surface are shown in Fig. 3.22 (a).

Spectra from different points indicate that the pristine sample is grown with same phase all over the surface. EEL spectra were collected from 400 to 920 eV region using energy dispersion of 0.1 eV. Spectrum from this region shows two distinct edges, one for Mn-$L_{2,3}$ edge (640 eV) and other for O-K edge (532 eV). The latter gives information on the transition of oxygen 1s electrons to 2p bands, which are oxidized with empty Mn 3d orbital. Separate plot of both Mn-$L_{2,3}$ and O-K edge is shown in Fig. 3.22 (b). The sharp edge of Mn-$L_{2,3}$ consists of two peaks related to the electron transitions from $2p_{3/2}$ (L_3 edge) and $2p_{1/2}$ (L_2 edge) core states to the unoccupied 3d states. The position of the oxygen K and manganese $L_{2,3}$ edges and the intensity ratio of “white-lines” (WL) [23] $I(L_3)/I(L_2)$, are characteristics of determination of the oxidation state of manganese [66]. The two main characteristic peaks of oxygen K edge can be described in terms of transition processes governed by the dipole selection rule. The peak ‘a’ around 535 eV has been ascribed to the electron transition from the 1*s* oxygen core state to the 2*p* state hybridized with manganese 3*d* orbital [67]. The second peak ‘b’ is related to the probable unoccupied oxygen 2p states mixed with the manganese 4sp. The position (at ~535 eV) of peak ‘a’ in the EELS spectra corresponds to the Mn_2O_3 phase of the material. This result is also consistent with earlier reports [66, 67]. The energy separation between the peak ‘a’ and peak ‘b’ of is ~10.8 eV which also confirms the Mn_2O_3 phase [66]. For calculating the WL intensity ratio $I(L_3)/I(L_2)$ there are many methods which have been previously reported [68]. Among these, the Pearson method [69] is the most popular and accurate to extract information on the WL ratio. According to the Pearson model, the experimental edge difference region is approximated by two steps functions in the Mn-L edge i.e. the energy difference between Mn-

L_3 and Mn-L_2. The details of the extraction method is described in the references [66, 69]. Using Pearson extraction method we obtained the WL ratio of our sample is about 2.35 to 2.4 (depending upon fitting accuracy) which is in exact agreement with earlier reported value ~2.44 [66] and 2.32 [70].

EELS spectra of Mn_2O_3-Au sample at different probe points (numbered in white red color on the HAADF image of the same sample) are also shown in Fig. 3.22(c). The probe points were on both Au nanostructures as well as on the Mn_2O_3 matrix. The EELS spectrum taken at all probe points on Mn_2O_3 is almost the same, constituting the same phase of the material, while the shift of Mn-$L_{2,3}$ peaks towards lower energy losses was observed in case of Mn_2O_3-Au,as seen in Fig. 3.22(d). This suggests a bond formation between Mn_2O_3 and Au. These results manifest the changes in bonding structure and electronic properties of the conjugated thin films, implying the formation of hetero-structured Mn_2O_3-Au thin film.

3.5 Conclusions:

A series of pristine Mn_2O_3 and co-electrodeposited Mn_2O_3-Au composite films were synthesized by choosing an appropriate voltage range using cyclic voltammetry technique for two sets of electrolyte parameters. A thorough comparative analyses of their deposition voltammograms along with detailed microscopy analyses revealed the influence of electrodeposited gold nanostructures on the morphology of composite films. Furthermore, in the case of the pristine Mn_2O_3 films, it was observed that the concentration of manganese acetate had a significant influence on the morphologies. All the samples were extensively characterized to understand their phase and structure.

This comparative analysis of co-electrodeposited Mn_2O_3-Au composite thin films indicate that, the morphology of the composite films are influenced by the incorporation of gold nanostructures along with the molar concentration of manganese acetate. Detailed structural characterizations showed, that, the phase and crystal structures of the pristine and composite films were independent of the difference in molar concentration of manganese acetate used.

Based on the detailed electron microsopic analysis of the co-electrodeposited composite film and a careful evaluation of the stepwise cyclic voltammogram, a probable formation mechanism and a series of chemical reactions for the formation of co-electrodeposited Mn_2O_3-Au composite sphere has been proposed. A schematic of the formation mechanism accompanied by corresponding scanning electron micrographs and voltammograms has been presented. As is evident in the case of the second co-electrodeposition, the same set of electrochemical reactions are applicable as discussed in the case of the co-electrodeposited microspheres. However, the morphologies of the pristine and the composite samples are entirely different from the first coelectrodeposition case. Furthermore, it is clearly visible that in the second case of coelectrodeposition, the microsphere like structure is absent in the composite film. This can be attributed to the higher molar concentration (0.1 M) of manganese acetate used in this case, leading to a higher rate of deposition of Mn_2O_3 as opposed to the preferential growth of Mn_2O_3 on the electrodeposited Au structures.

The samples obtained from the first and second sets of electrolyte precursor have been further applied for electrochemical sensing and electrochemical charge storage, respectively and the reason for this is described as follows. The current density in the cyclic voltammogram is much higher for the second co-electrodeposited sample suggesting a higher capacitance as compared to the samples obtained from the first set of co-electrodeposition. However, when the first co-electrodeposited Mn_2O_3-Au composite microsphere sample was tested for electrochmical hydrogen peroxide sensing, it revealed acceptable results.

The details of the electrochemical hydrogen peroxide sensing and electrochemical charge storage studies of the as obtained samples have been discussed elaborately in Chapters

4 and 5, respectively.

This method of co-electrodeposition depicts an easy, fast, and one step synthesis technique, for fabricating gold nanostructure incorporated manganese oxide thin films. The main advantage of this fabrication process is its simplicity and lack of requirement of complex deposition set ups such as those required in vapor deposition techniques. Electrodeposition method is advantageous, because, a composite sample can be fabricated directly, on a conducting substrate and may be applied in other applications. By carefully choosing the voltage range for cyclic voltammetry, this technique may be extended to other materials such as different kinds of oxides or for multicomponent hierarchical nanostructures.

CHAPTER 4

Chapter 4

Electrochemical hydrogen peroxide sensing with Mn_2O_3-Au composite

4.1 Introduction:

4.1.1 Importance of Hydrogen Peroxide Sensing:

Hydrogen peroxide (H_2O_2) is a colourless chemical compound whose viscosity is slightly higher than water. It is one of the simplest peroxide compounds, which can be used as an oxidizer, bleaching agent, and disinfectant. Thermodynamically, it is known to be unstable and may decompose to form water and oxygen. The rate of decomposition tends to increase with rising temperature, concentration, and pH, wherein, cool, dilute, acidic solutions of hydrogen peroxide show the highest stability.

Application of H_2O_2 in waste-water treatment processes to remove organic contaminants is of great importance [71]. H_2O_2 has several cosmetic applications as well such as in bleaching, tooth whitening [73] and in skin treatments. High-concentration H_2O_2 can be used either as a monopropellant (without mixing with fuel) or as the oxidizer component in a bipropellant rocket in rocket applications. The disinfecting property of hydrogen peroxide finds various domestic uses, primarily as a cleaning and disinfecting agent. Hydrogen peroxide reacts with certain di-esters, such as phenyl oxalate ester (cyalume), to produce chemiluminescence; this application is most commonly encountered in the form of glow sticks [73]. Some horticulturalists suggest the use of dilute H_2O_2 solution in watering solutions. Its spontaneous decomposition releases oxygen that enhances a plant's root development and helps to treat root rot (cellular root death due to lack of oxygen) and a variety of other pests.

Despite the abovementioned advantages, H_2O_2 in its pure or diluted form, can pose several risks, the main one being that it forms explosive mixtures upon contact with organic compounds [74]. Highly concentrated H_2O_2 solutions tend to be unstable and can cause expanding liquid vapour explosion in the container that holds the liquid. As a result, distillation of hydrogen peroxide at normal pressures is extremely dangerous. Due to its corrosive nature, precautionary steps must be followed while handling even dilute concentrations of H_2O_2, while avoiding its direct contact with eyes, mucous membranes, and skin.

Considering the wide variety of applications of hydrogen peroxide, researching on the development of novel materials towards the application of low cost, easy to synthesize materials for hydrogen peroxide sensing continues to be of tremendous importance in the area of materials science. In electrochemistry, H_2O_2 can either be oxidised or reduced, directly at ordinary solid electrodes. However, in analytical applications, these techniques suffer from slow electrode kinetics and high overpotential, which may be detrimental for obtaining a good sensing performance and may incur large interferences from other electroactive species such as, ascorbic acid, uric acid which may co-exist in the solution. Even though, conventional techniques such as fluorimetry, chemiluminescence, fluorescence, and spectrophotometry have been traditionally used for sensing purposes, they involve complex procedures of experimental set up, which are generally costly and time consuming. In comparison to these, electrochemistry offers simple, rapid, cost effective means for detection of a variety of analytes.

4.1.2. An overview of materials used for electrochemical hydrogen peroxide sensing:

The current motivation of research in electrochemical sensing revolves around the modifications of ordinary electrode surfaces with the view to improve electron transfer kinetics and decreased redox overpotential. Different kinds of nanomaterials such as redox proteins, transition metals and their oxides, metal pthalocyanines, porphyrines, redox polymers, carbon nanotube, and graphene have been used to design effective hydrogen peroxide sensing platforms [74]. Enzymes used for the decomposition of H_2O_2 are classified as peroxidases and catalases.

Since the reduced form of ferric hexacyanoferrate also known as Prussian blue (PB), can catalyze the reduction of H_2O_2 at low potentials (50 mV (vs. Ag/AgCl)) analogous to peroxidases, it is commonly known as artificial peroxidase [75]. Owing to the polycrystalline structure of PB it allows the penetration of small molecules into its lattice, while excluding larger molecules such as ascorbic acid (AA), uric acid (UA), and para-acetylaminophenol (APAP), PB offers good catalytic specificity towards H_2O_2 [75]. Consequently, PB or PB-based composites have been intensively studied and widely used in biosensor constructions [75]. The major drawback of PB in sensing applications is the lack of operational stability in neutral and alkaline solutions because the reduced the form of PB, Prussian white, can be dissolved in the presence of hydroxide ions [76].

Heme proteins, such as horseradish peroxidase (HRP), catalase (CAT), cytochrome c (Cyt c), hemoglobin (Hb), microperoxidase (MP), and myoglobin (Mb) are a category of metalloproteins containing iron centered porphyrin as their prosthetic groups. The iron present in the heme can easily undergo oxidation and reduction over a wide range of potentials which are varied by the protein environment around heme groups [77]. Due to the redox capability of heme proteins, they have the great potential to be used in bio-electrochemical applications. Though HRP, Hb, CAT, Mb, and Cyt c have been used to successfully construct the third-generation biosensors, their differences in direct electrochemistry remain.

CNTs have been widely used for chemical and biological sensing applications owing to the possibility of surface functionalization provides tremendous scope in tuning their electro-catalytic activity [78]. Studies have shown that CNTs can electro-catalyze both the oxidation and reduction of H_2O_2.

Transition metals are known as good catalysts because of their ability to adsorb other substances onto their surface and activate them in the process and their compounds exhibit the tendency to adopt multiple oxidation states, resulting in favourable electrocatalytic properties. Nano-sized metals can display unique advantages of enhanced mass transport, high effective surface area, size controlled electrical, chemical, and optical properties and effective utilization of expensive materials. A wide range of transition metals including platinum, palladium, copper, rhodium, iridium and iron have been successfully used for electrocatalyzed H_2O_2 determination [79].

Metal oxides such as manganese oxide, cobalt oxide, titanium dioxide, copper oxide, and iridium oxide have been reported to show electrocatalytic activity towards H_2O_2 detection. In the past, some groups have reported H_2O_2 sensors based on MnO_2 [80]. For example, Taha and Wangever reported a glassy carbon electrode (GCE) modified by a film of MnO_2 in $MnCl_2$/NaOH solution, which showed a low detection limit of 80 pg (about 1.5×10^{-7} M) but the detection was conducted in strong alkaline solution [81]. Yao et al. [82] reported a hydrogen peroxide amperometric sensor based on MnO_2 nanoparticles and dihexadecyl hydrogen phosphate composite film. Lin et al. [83] synthesized nanostructured cryptomelane-type manganese oxide for chemical sensing H_2O_2 with a lower detection potential (+0.3 V vs. SCE).

All these studies are based on the strong catalytic oxidation property of MnO_2 nanoparticles-modified electrodes.

In the case of MnO_2 nanoparticle and dihexadecyl hydrogen phosphate composite film modified electrode was used for H_2O_2. determination at an applied potential of +0.65 V (vs. saturated calomel electrode (SCE)) [83]. A TiO_2/MWCNT (multi-walled carbon nanotube) modified electrode has been reported to detect H_2O_2 at an applied potential of +0.4 V (vs. Ag/ AgCl) [84]. Xu et al. reported the MnO_2/MWCNT modified electrode for H_2O_2 determination which showed high anti-interference property without any permselective membranes against AA, citric acid, and UA in spite of the high operation potential of 0.45 V (vs. Ag/AgCl) [85]. Bai et al. discovered that MnO_2 nanoparticle modified electrodes show bi-direction electro-catalytic ability towards the reduction/oxidation of H_2O_2 [86]. In the present case, we investigate the electrochemical sensing performance of the co-electrodeposited Mn_2O_3-Au composite microsphere electrode towards H_2O_2 sensing. A thorough survey of literature suggests that utilization of Mn_2O_3-Au co-electrodeposited composite for electrochemical H_2O_2 sensing is the first of its kind.

4.2 Results and Discussion:

As discussed in chapter 3, the spherical Mn_2O_3-Au nanocomposite network was synthesized on indium tin oxide coated glass (ITO) by means of a one-step co-electrodeposition technique. The details of the co-electrodeposition process along with the extensive materials characterization of the sample have been discussed in Chapter 3. The sample corresponding to the first set of co-electrodeposition has been tested for its H_2O_2 sensing capability.

4.2.1 Electrochemical Impedance Spectroscopy Studies:

To investigate the charge transfer properties at the electrode-electrolyte interface, EIS was performed in the frequency range from 0.1 Hz to 100 KHz for the pristine Mn_2O_3 and the Mn_2O_3-Au composite sample. In the context of electrocatalytic behavior, charge transfer properties of the participating electrode are more relevant as compared to the contribution from diffusion of ions in the electrolyte [87]. To investigate this charge transfer behavior, a redox probe i.e. an equi-molar mixture of potassium ferrocyanide and potassium ferricyanide (5mM) ($Fe(CN)_6^{3-/4-}$) in 0.1 M KCl was employed. As discussed elaborately in Chapter 2, the semi-circular portion corresponding to the high frequency region represents an electron transfer limited process, while the linear region at low frequencies corresponds to diffusion limited processes.

For correlating the EIS data with the interfacial phenomena, the experimental data (Fig.4.1(a)) were fitted with a suitable Randle's circuit as shown in Fig.4.1(b) and Fig.4.1(c). The diameter of the semicircle which is a measure of the charge transfer resistance (R_{ct}) at the electrode-electrolyte interface, has a much smaller value for the Mn_2O_3–Au sample, as evident from the EIS plot and from the parameters obtained by fitting the equivalent circuits. The R_{ct} for Mn_2O_3 is 2821 Ω whereas the composite sample shows an R_{ct} of 312.3 Ω, indicating a drastic reduction, suggesting an improved electron transfer property. Moreover, the surface resistance (R_s) of the Mn_2O_3-Au composite sample is also lower than that of pristine Mn_2O_3. Hence, the combined effect of the reduction in R_{ct} and R_s of the Mn_2O_3-Au composite system leads to an improvement in its electrochemical charge transfer property, which is crucial for improving electrochemical sensing. The results obtained from the charge transfer studies clearly demonstrate the role of incorporation of gold in improving the sensing capability of the pristine Mn_2O_3 film due to the improvement of charge transfer through faradaic redox reaction in Mn_2O_3-Au sample. The presence of Au acts as a source of extra free charge in the composite sample (active electrode material).

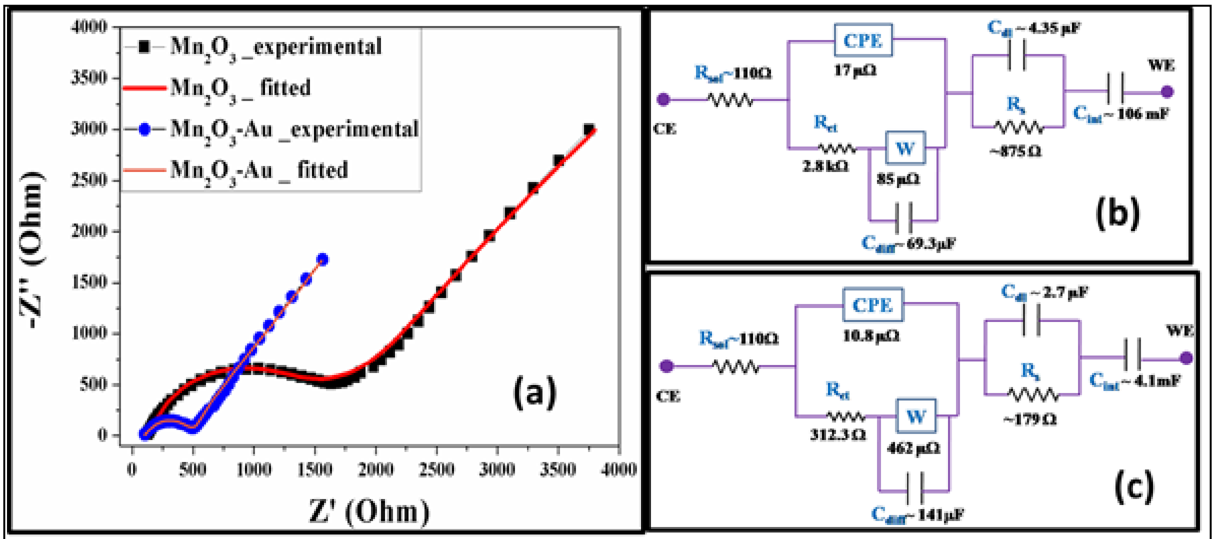

R_{sol}: solution resistance, R_{ct}: Charge transfer resistance, CPE: constant phase element,
W: Warburg impedance, C_{diff}: diffusion capacitance, C_{dl}: double layer capacitance, R_s: surface resistance,
C_{int}: Interfacial Capacitance

Fig.4.1: (a) EIS spectra and fitted impedance data of Mn_2O_3 and Mn_2O_3-Au composite conducted in $K_3Fe(CN)_6/K_4Fe(CN)_6$ (1:1 mixture) in 0.1M KCl from 0.1Hz to 100 KHz at perturbation voltage of 5 mV, equivalent Randle circuit corresponding to the fitted data for (b)Mn_2O_3 and (c)Mn_2O_3-Au.

4.2.2. Cyclic Voltammetry Studies

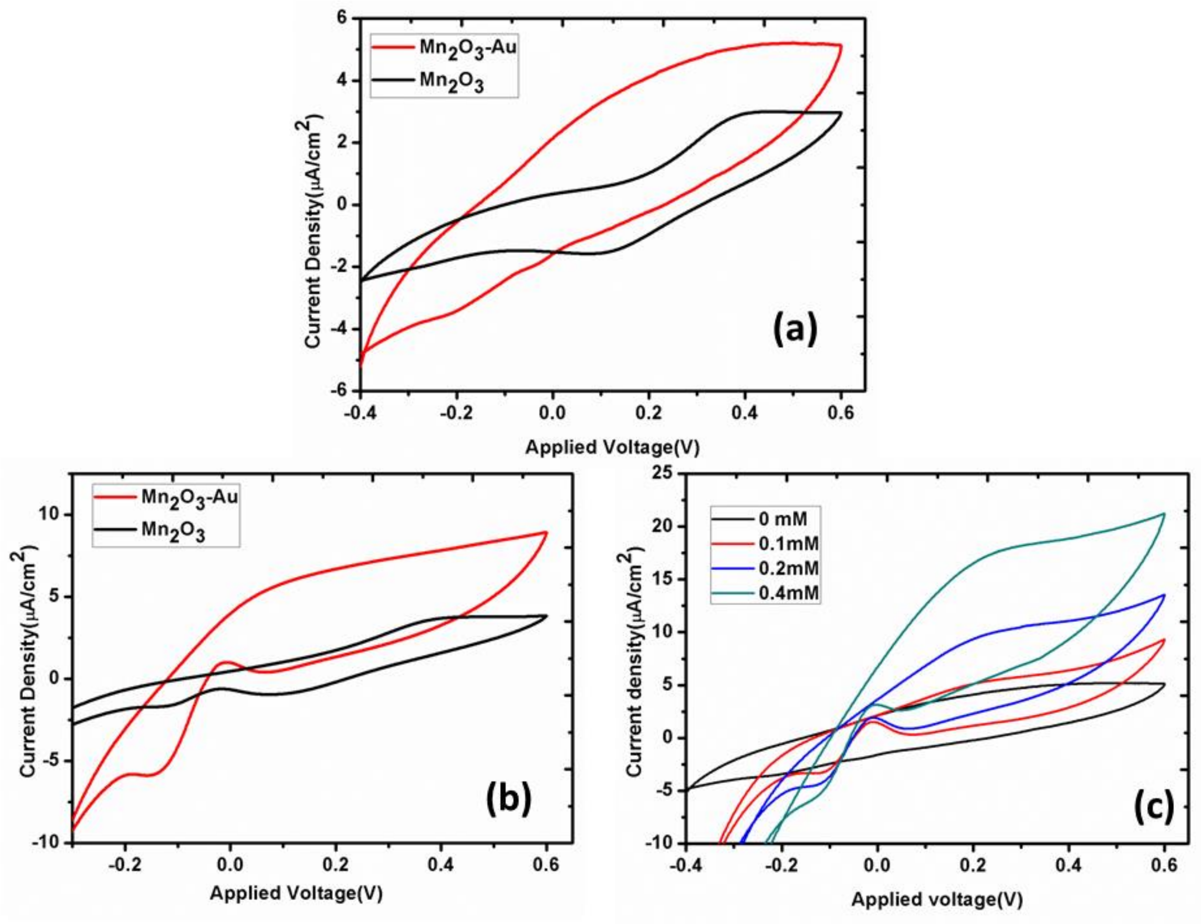

Fig. 4.2: Comparative CV of Mn_2O_3 and Mn_2O_3-Au composite (a) in absence of H_2O_2 and (b) presence of 0.2 mM H_2O_2, (c) Mn_2O_3-Au CV for different concentrations of H_2O_2 conducted in 0.1 M NaOH between -0.4 to 0.6 V at scan rate of 0.05 V/s

The CV responses of the pristine and composite samples conducted in 0.1 M NaOH, in the voltage range between -0.4 to 0.6 V, at a scan rate of 0.05 V/s are shown in Fig. 4.2(a). In the absence of H_2O_2, enhancement in the CV current of the pristine Mn_2O_3 could be correlated with the oxidation of Mn (III) of Mn_2O_3 to Mn (IV) of MnO_2 during the oxidation segment and the reverse reaction in the reduction segment.

A similar process is expected to occur in the composite sample as well. However, due to the oxidation-reduction processes of Au happening at similar potential regions (CV of

Fig.4.8 (a)) the peaks in the composite sample appear to be overlapped as compared to that in the pristine sample. Furthermore, to study the CV behavior in the presence of H_2O_2, CV was conducted in the presence of 0.2 mM H_2O_2 in an alkaline medium of 0.1M NaOH (pH~12) at a scan rate of 0.05 V/s. The corresponding results are depicted in Fig. 4.2(b). As can be observed from the CV plot, with the addition of H_2O_2, the increase in oxidation current is significantly higher than that in the reduction cycle. This is similar to the previously reported behavior of H_2O_2 electrochemistry at manganese oxide electrodes [85]. Furthermore, it is observed that this trend continues with the addition of increasing H_2O_2 concentration, as indicated in Fig. 4.2(c). A possible reason for this could be explained in the following way. In the oxidation cycle of the CV, in the presence of H_2O_2, the following set of reactions are expected to take place:

$Mn_2O_3 + H_2O_2 \longrightarrow 2MnO + H_2O + O_2$, i.e. reduction of Mn_2O_3 from +3 to +2 state and oxidation of H_2O_2 with the formation of water and O_2.

Subsequently, MnO oxidizes back to +3 state

$2MnO + 2OH^- \longrightarrow Mn_2O_3 + H_2O + 2e^-$

Next, in the reduction cycle, the Mn_2O_3 is further electro-reduced to lower states (2 peaks in reduction cycle)

$Mn_2O_3 + H_2O + 2e^- \longrightarrow 2MnO + 2OH^-$

$Mn_2O_3 + 3H_2O + 2e^- \longrightarrow 2Mn(OH)_2 + 2OH^-$

A three-fold increase in the oxidation current density is observed in Fig. 4.2(b) for the Mn_2O_3-Au composite sample, as compared with pristine Mn_2O_3, indicating an improved electrocatalytic property of the composite sample towards H_2O_2 sensing. Fig. 4.2(c) shows the CV response of Mn_2O_3-Au samples upon addition of increasing molar concentrations of H_2O_2.

The current density in the oxidation cycle is observed to increase (with the peak at 0.25 V), with the increasing molar concentrations of H_2O_2.

4.2.3. Amperometry Studies:

The response of Mn_2O_3-Au as an H_2O_2 sensor was further evaluated by amperometric I-t technique and the results are discussed as follows. For comparative analysis, amperometry was conducted at 0.25 and -0.15 V, corresponding to the oxidation and reduction peaks observed in Figs. 4.2(b) and (c). As discussed above, since the electro-oxidation behaviour of H_2O_2 takes place in the oxidation cycle at around 0.25 V, electrochemical sensing is expected to be favourable at the same potential. Correspondingly, it is clear from Figs. 4.3 (a) and (b), that the amperometry studies conducted at 0.25 V show steady increase in step size while the one conducted at -0.15 V depicts a poor response. This further confirms the results derived from the CV of Fig. 4.2.

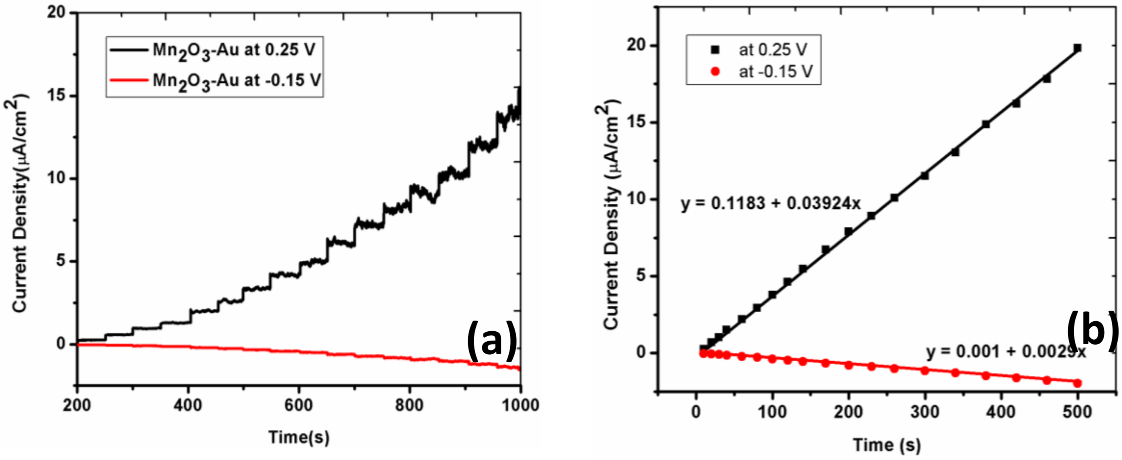

Fig.4.3: Comparative I-t of Mn_2O_3-Au composite sample at 0.25 and -0.15 V

The electrochemical sensing response was further optimized in terms of the operating potential. The results for which are depicted in Fig. 4.4, which shows the amperometry results obtained for different working potentials of the oxidation segment. Based on these studies, 0.25

V was chosen as the operating potential for calibrating the Mn_2O_3-Au composite sensor electrode. Finally, the response was optimized in terms of the molar concentration of NaOH and based on a set of control experiments and 0.1 M NaOH was chosen for the final calibration of the sensing electrode. These results have been depicted in Fig. 4.5.

For the final calibration of the sensing response of the Mn_2O_3-Au sample, amperometry was conducted at a potential of 0.25 V in 0.1 M NaOH under continuous stirring with the addition of fixed amounts of increasing molar concentration of H_2O_2. The corresponding amperometric I-t curve is shown in Fig.4.6 and the corresponding calibration curve is shown in the inset.

The sensitivity towards H_2O_2 detection, obtained from the calibration curve for the linear range corresponding to 10-500 μM is 39.24 μA/mM cm^2 with a correlation coefficient (R^2) of 0.9995 and the limit of detection was obtained as 0.34μM (signal to noise ratio, S/N=3). A comparative plot of the amperometric response between the pristine and composite samples is depicted in Fig. 4.7. As evident from the calibration curve (Fig. 7(a)), the sensitivity of the pristine Mn_2O_3 sample is 14.02 μA/mM/cm^2. This is almost three order lower than the composite sample. Previous reports on electrochemical H_2O_2 detection suggest that clean Au surfaces and Au nanoparticles are excellent candidates for H_2O_2 oxidation and reduction in neutral and alkaline media [89, 90]. Furthermore, some of the pioneering works on enzymatic H_2O_2 sensors based on HRP modified working electrodes have been reported by research groups of Lo Gorton [91, 92], James Rusling [93, 94] and Naifei Hu [95]. A comparison of the parameters of our sensor with some of their notable works has been performed and the results are presented in Table1.

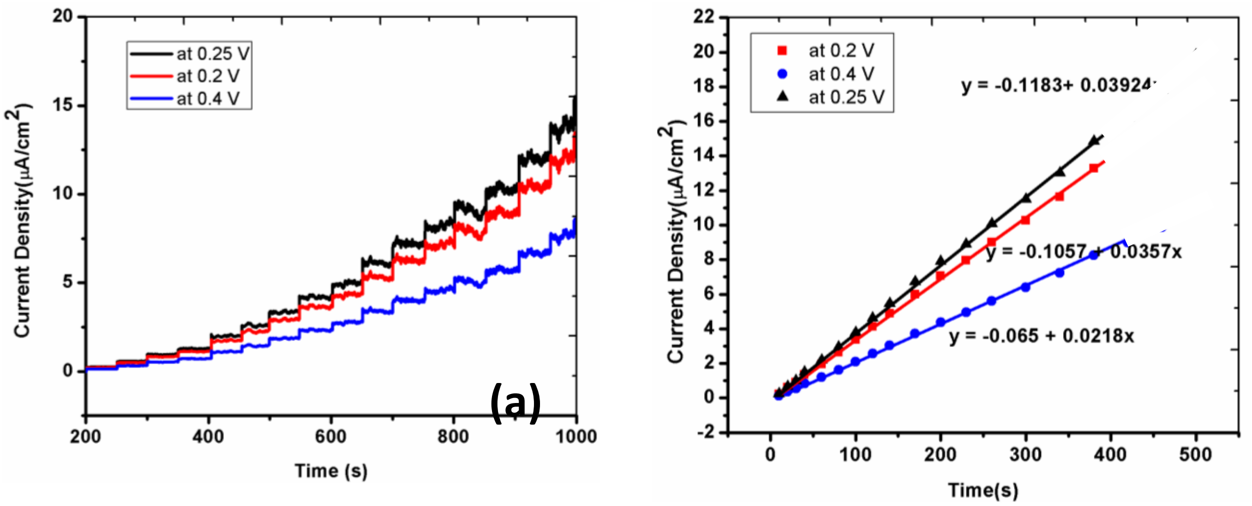

Fig.4.4: Comparasion of I-t at different voltages and corresponding calibration graphs.

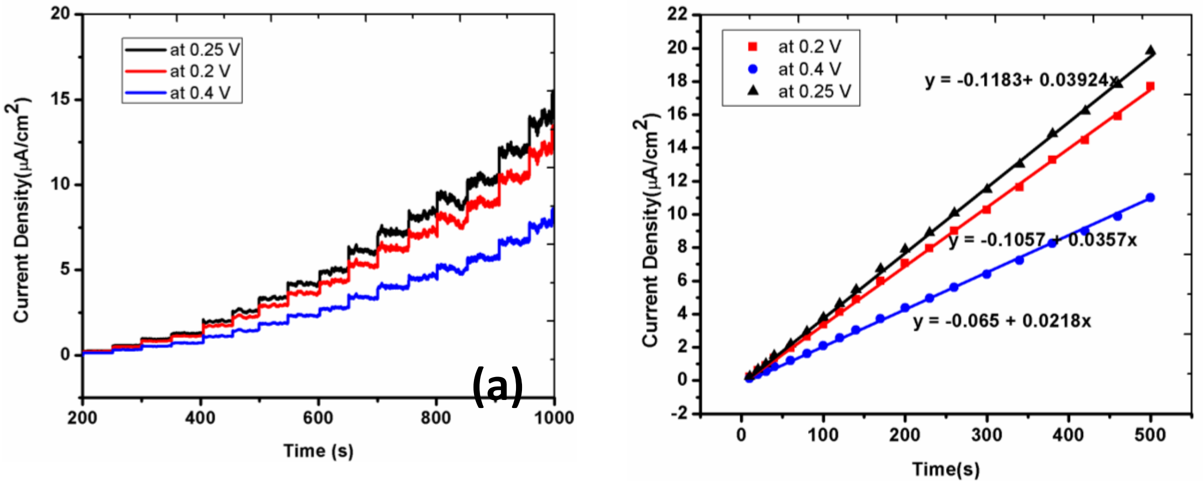

Fig.4.5: Amperometric sensing at different molar concentrations of NaOH and their corresponding calibrtion plots

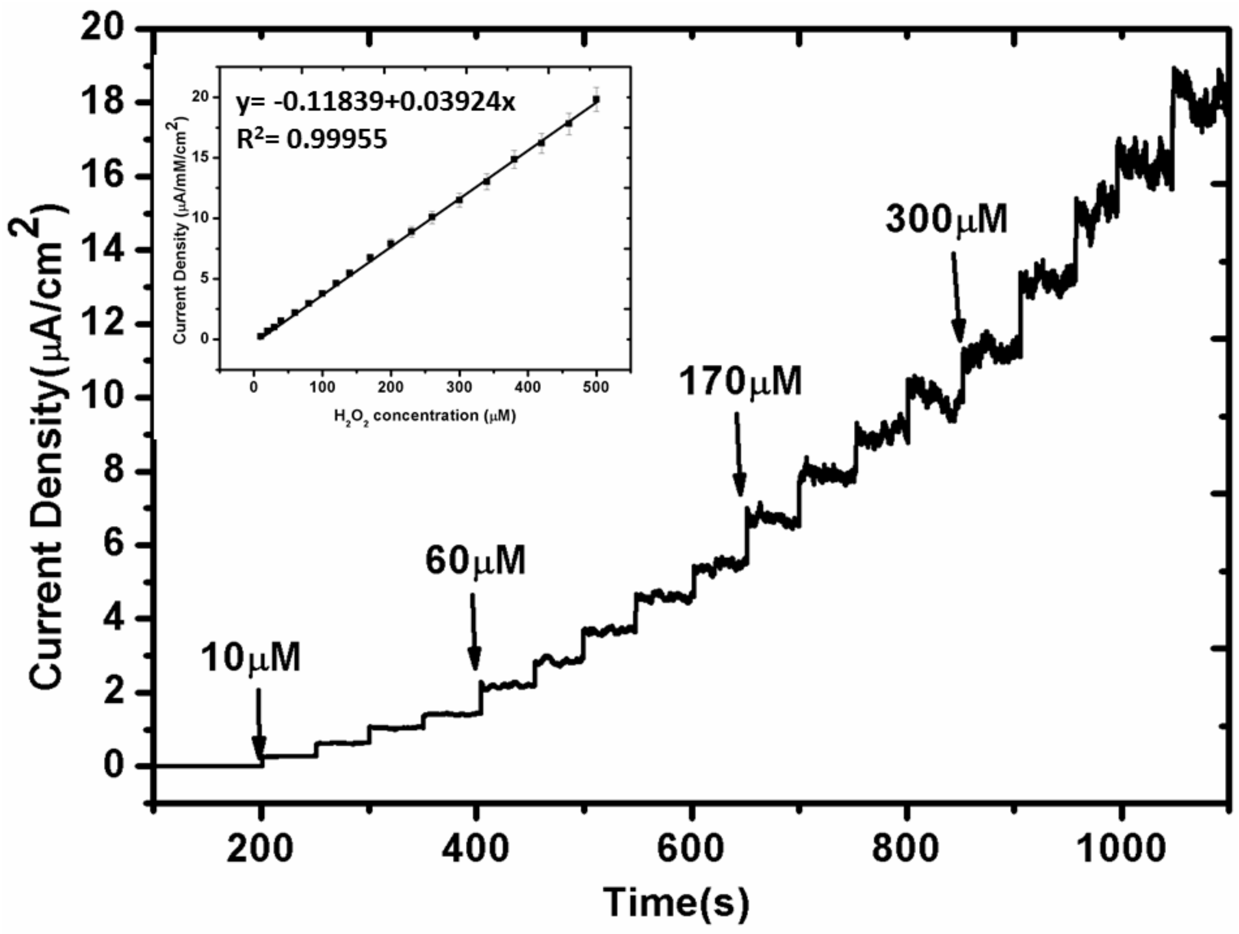

Fig.4.6: Amperometric response of Mn_2O_3-Au composite for successive additions of H_2O_2 stock solutions and corresponding calibration curve (inset) conducted in 0.1M NaOH solution at at applied potential of 0.25 V.

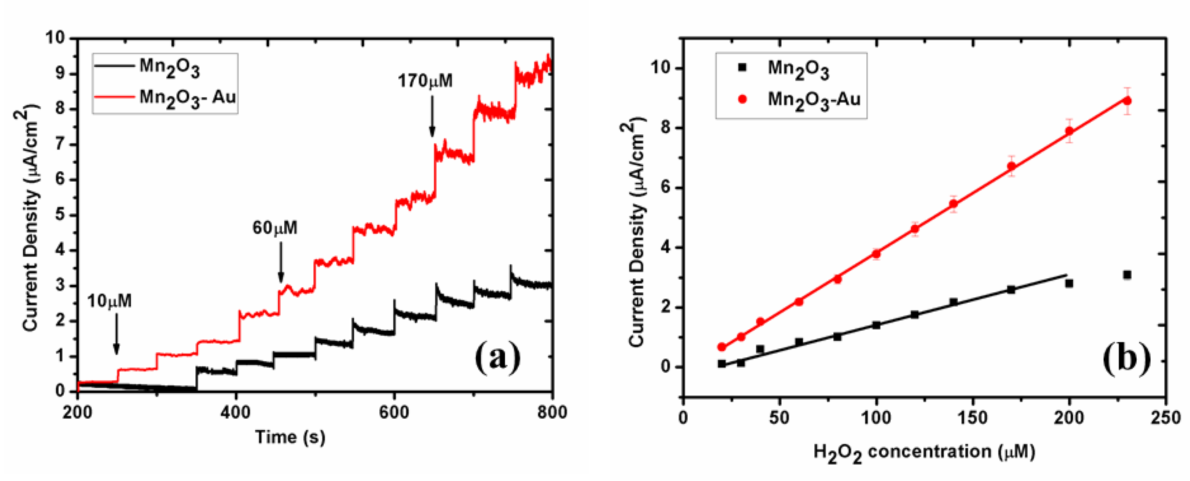

Fig. 4.7: (a) Comparative amperometry and (b) calibration plots of both pristine Mn_2O_3 and Mn_2O_3-Au composite samples.

4.2.4. Interference Studies

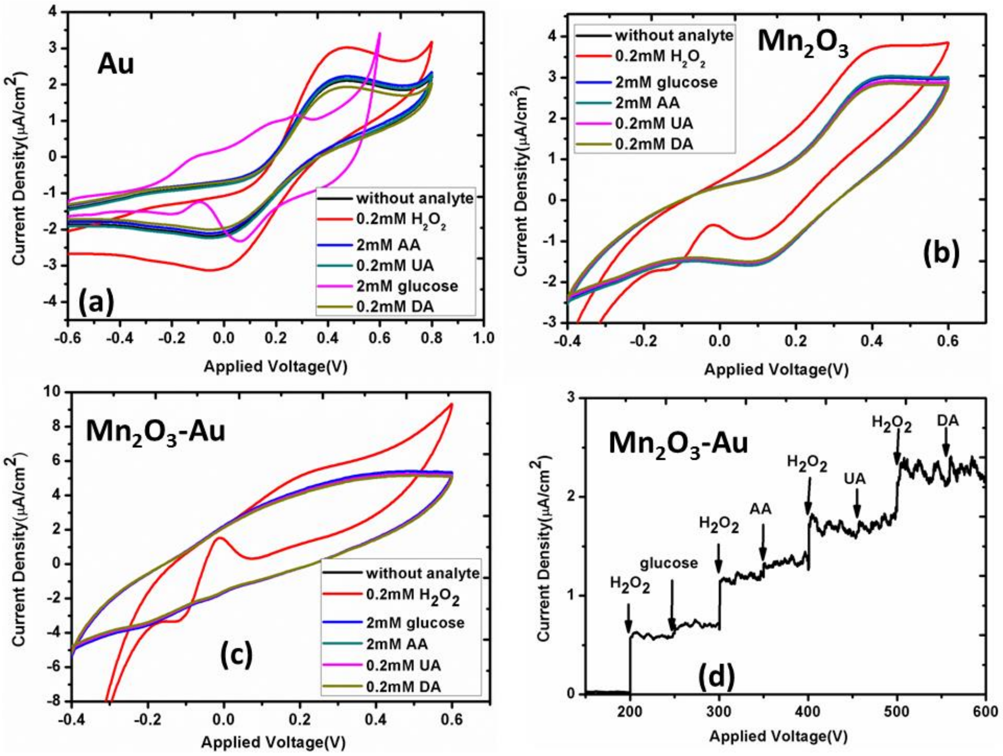

Fig.4.8: (a) Comparative CV of Au, (b) Mn_2O_3, (c) Mn_2O_3-Au for 0.2 mM H_2O_2, 2 mM glucose, 2 mM AA, 0.2 mM UA and 0.2 mM DA. All CVs conducted in 0.1 M NaOH at scan rate of 0.05 V/s (d) amperometric I-t curve of Mn_2O_3-Au at 0.25 V for addition of 20 μM H_2O_2, 200 μM glucose, 200 μM AA, 20 μM UA, 20 μM DA

An important consideration of most non-enzymatic sensing platforms is the effect of interferences from other co-existing species, especially ascorbic acid (AA) and glucose which are generally oxidised at potentials similar to H_2O_2 oxidation. Hence, a series of detailed interference tests were performed by cyclic voltammetry and chronoamperometry techniques for electrodeposited Au, Mn_2O_3 and Mn_2O_3-Au composite. The results are presented in Fig. 4.8.

Fig. 4.8 (a), (b), and (c) show the comparative CVs of Au, Mn_2O_3 and Mn_2O_3-Au samples respectively in presence of 0.2 mM H_2O_2, 2 mM of AA, 2 mM glucose, 0.2 mM (Uric Acid) UA and 0.2 mM (dopamine) DA. As can be seen, at the Au working electrode the oxidation current response for H_2O_2 is significantly higher in comparison with AA, UA, and

DA, even though it does show a tendency towards glucose oxidation at lower potentials. The nature of the CV curve of H_2O_2 oxidation is in agreement with an earlier report on H_2O_2 oxidation at Au electrode in alkaline medium [40].

The onset of electro-oxidation of glucose at the Au occurs at a potential of -0.2 V. At the Mn_2O_3 deposited electrode, the response towards H_2O_2 oxidation is the best as compared with glucose, AA, DA, and UA. From the comparative CVs for Mn_2O_3-Au composite sample in presence of H_2O_2, glucose, AA, UA, DA, it is evident that the response towards H_2O_2 oxidation is the highest. Even though, the response of the composite sample towards the interfering species is similar to pristine Mn_2O_3, the value of current density towards H_2O_2 oxidation is significantly higher. Fig. 4.8 (d) shows the chronoamperometry response of Mn_2O_3-Au towards the interfering analytes and H_2O_2. The concentrations of the interfering analytes (glucose and AA) are taken to be an order higher than H_2O_2. The change in current density for the addition of 200 μM AA and glucose, 20 μM UA and 20 μM DA is negligible compared to the addition of 20 μM H_2O_2 suggesting a good selectivity of the Mn_2O_3-Au composite system towards H_2O_2 electro-oxidation. The molar concentrations of all interfering analytes were chosen keeping in mind their relative concentrations to H_2O_2 in real systems.

Furthermore, to assess the reusability of the working electrode, an EIS measurement was performed after one round of amperometric measurements and the results are depicted in Fig. 4.9. It is evident, from the graphical and fitting results, that there is a significant increase in the charge transfer resistance, suggesting the applicability of the Mn_2O_3-Au electrode in single use applications.

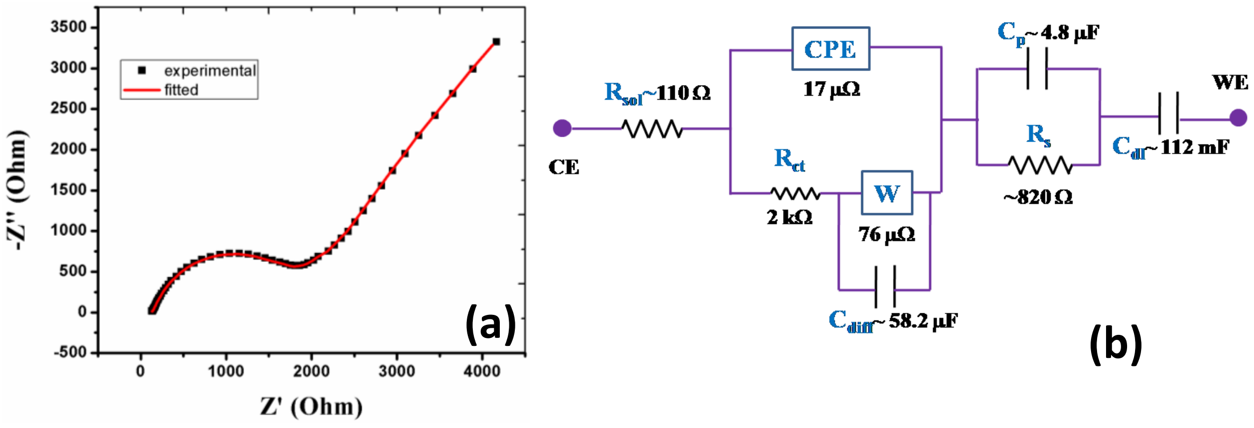

Fig.4.9: EIS spectra and fitted impedance data Mn_2O_3-Au composite after a single round of amperometric studies conducted in $K_3Fe(CN)_6$/$K_4Fe(CN)_6$ (1:1 mixture) in 0.1 M KCl from 0.1 Hz to 100 KHz at perturbation voltage of 5 mV, equivalent Randle circuit corresponding to the fitted data for Mn_2O_3-Au.

4.3 Conclusions:

In conclusion, the electrochemical H_2O_2 sensing studies were conducted on Mn_2O_3–Au composite spherical network and a detailed comparative analysis between the pristine Mn_2O_3 and Mn_2O_3-Au composite were performed. Our studies show a significant improvement in the electrocatalytic properties of the latter. Amperometric studies indicate that the Mn_2O_3-Au nanocomposite shows a linear response towards H_2O_2 oxidation with a sensitivity of 39.24µA/mM/cm^2 which is almost three orders higher than the pristine Mn_2O_3 sample. A comparison of Mn_2O_3-Au sensing performance with clean Au surface [89], nanoporous Au [94], and Au nanoparticles [89] reveal a lower detection limit of our system. Furthermore, comparison with HRP based enzymatic H_2O_2 sensors in similar working range of concentration reveal that the sensing performance of our Mn_2O_3-Au system is comparable [95], in some cases better [90] than enzyme based H_2O_2 sensors. Hence, characteristics such as easy synthesis, good sensitivity, low detection limit and negligible interference from other analytes, suggest that the Mn_2O_3-Au composite would be a good candidate for non-enzymatic H_2O_2 sensing.

Table 1 Comparative performances of electrochemical H_2O_2 sensors

Electrode Material	**Linear Range**	**Sensitivity**	**Limit of Detection**	**Reference**
Polycrystalline gold electrode	20 µM-6 mM	-------	4 µM	88
Nanoporous Au	10 µM-8 mM	-------	3.26 µM	94
Au NPs-graphene-chitosan composite	5 µM-35 mM	-------	1.6 µM	89
SWCNT-HRP	0.5-500 µM	5.1nA/µM/cm^2	0.4 µM	90
GCE/Prussian Blue NPs/Nafion	2.1-140 µM	136µA/mM/cm^2	1 µM	91
Tobacco Peroxidase	0.5-130 µM	24.7µA/mM	71 nM	97
Graphite/sulphonated polyaniline/HRP	Upto 0.3 µM	14µA/µM/cm^2	3 nM	98
MnO_2-GO composite	5-600 µM	38.2µA/mM/cm^2	0.8 µM	96
Mn_2O_3-Au	**10-500 µM**	**39.2mA/mM/cm^2**	**0.34 µM**	**This Work**

CHAPTER 5

Chapter 5

Electrochemical charge storage properties of Mn_2O_3-Au film

5.1 Introduction

5.1.1. Classification of Supercapacitors

Supercapacitor electrodes can be primarily categorized into three types, i.e. the electrochemical double layer capacitors (EDLCs), pseudocapacitors, and hybrid capacitors. The classification is presented diagrammatically in Fig. 5.1. EDLCs can store charge electrostatically, via a non-faradic process, which does not involve transfer of charge between the electrode and the electrolyte [100]. The principle of energy storage in the EDLCs is based on the formation of the electrochemical double layer. When an external voltage is applied, there is an accumulation of charge on the electrode surfaces. The difference in potential causes an attraction of the opposite charges, resulting in diffusion of ions in the electrolyte and onto the pores of the oppositely charged electrode. To avoid recombination of ions at electrodes, a double layer of charge is formed. The double layer, combined with the increase in specific surface area and reduction in distances between the electrodes, allows EDLCs to attain a higher energy density [101]. Additionally, the storage mechanism of EDLCs results in fast energy uptake, delivery, and better power performance. The charge storage mechanism being a non-faradic process, involves no chemical reactions. However, due to the electrostatic surface charging mechanism, EDLC devices experience a limited energy density. Currently, the major focus of EDLC research is towards improving the energy performance and working range of temperature, where batteries cannot operate. Performance of EDLCs may also be adjusted by modifying the type of electrolyte used.

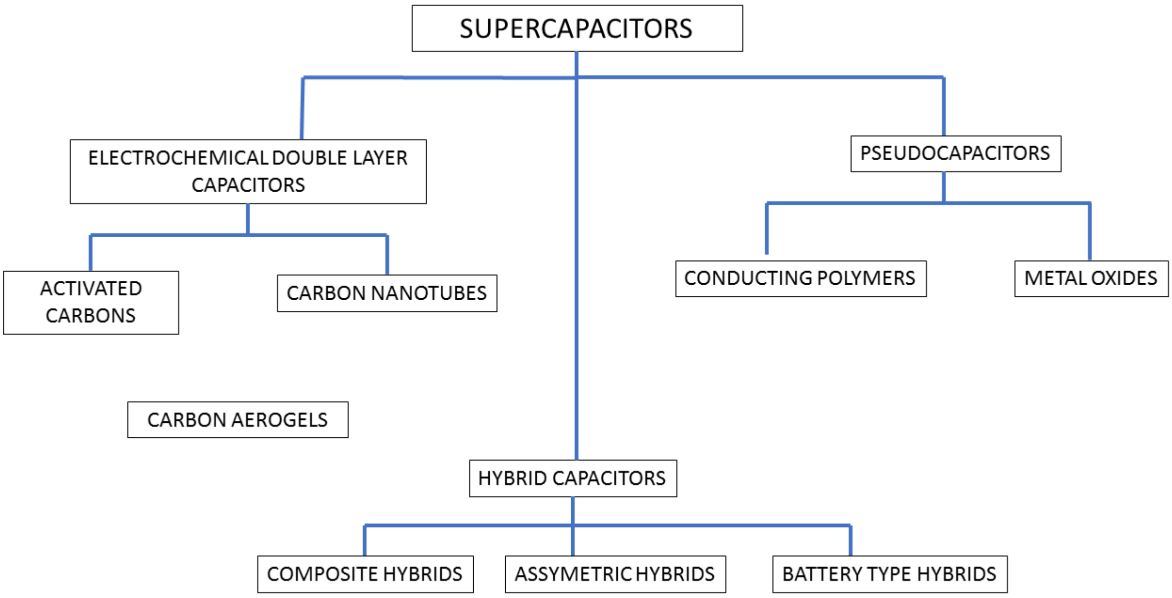

Fig.5.1: Classification of Supercapacitors

On the other hand, pseudocapacitors store charge via faradaic processes which involves the transfer of charge between electrode and electrolyte [102]. When an external potential is applied to a pseudocapacitor, reduction and oxidation takes place on the electrode material, resulting in passage of charge across the double layer. This causes a faradaic current to pass through the supercapacitor cell. The faradaic processes involved in pseudocapacitors allows them to achieve greater specific capacitances and energy densities compared to EDLCs [103]. The materials commonly employed in fabrication of pseudocapacitors are metal oxides and conducting polymers.

Hybrid capacitors combine non-faradaic and faradaic processes by coupling an EDLC with a psuedocapacitor electrode. They are set up in a way that the carbon material is used as a negative electrode while either metal oxide or conducting polymer as positive electrode [104].

Battery type hybrid combines two different electrodes, like in the case of asymmetric hybrids but in this case, they are made up by combining a supercapacitor electrode with battery electrode. This configuration was set up to utilize the properties of supercapacitors and batteries in a single cell [105].

5.1.2. Materials used for constructing supercapacitor electrodes

The fundamental parameters that decide the type of electrode materials which may be used in fabrication of supercapacitor electrodes are its capacitance and charge storage.

Owing to their low cost, high surface area, abundant availability, and established electrode production technologies, carbon materials and their various forms are widely used in the fabrication of supercapacitor electrodes. Since, the storage mechanism applicable in carbon materials is based on the electrochemical double layer formed at the interface between the electrode and electrolyte, the capacitance mainly relies on the surface area accessible to electrolyte ions. Important factors which influence the electrochemical performance are specific surface area, pore shape and structure, pore size distribution, surface functionality and electrical conductivity [106-109]. Having a high specific surface area in the case of carbon materials, results in a high capability for charge accumulation at the interface of electrode and electrolyte.

A great deal of attention has been focussed on the application of carbon nanotubes (CNTs) as a supercapacitor electrode material due to its unique pore structure, good mechanical and thermal stability, and superior electrical properties [110, 111]. Unlike other carbon-based electrodes, CNTs have mesopores that are interconnected, this allows for a continuous charge distribution that utilizes almost the entire accessible surface area. Recently, the application of graphene as supercapacitor electrode materials has been explored [112]. Among all carbon materials used as electrode materials in electrochemical double layer capacitors, graphene displays a specific surface area (SSA) of around 2630 m^2 /g. If the entire SSA is fully utilized, it is possible to achieve a capacitance of up to 550 F/g using graphene.

Metal oxides present another alternative for fabrication of supercapacitor electrodes. The commonly used metal oxides are nickel oxide, ruthenium dioxide, manganese oxide, and iridium oxide [113]. In general, their low cost of production and use of mild electrolyte solutions make them a feasible alternative in supercapacitor fabrication.

Since the electrochemical capacitor market continues to grow and expand to provide a greater number of applications, continuous research on electrode materials, cell assembly, and entire cell systems should yield electrochemical capacitors that exhibit the excellent properties of both conventional capacitors and batteries and might ultimately facilitate the emergence of new types of energy storage devices.

Composite electrodes integrate carbon based material with either metal oxide or conducting polymer materials, which in turn offers both physical and chemical charge storage mechanisms in a single electrode. In these lines, a comparative study has been performed between CNT, pure MnO_2 and a composite of MnO_2/CNT [114]. The composite was prepared using simple hydrothermal treatment wherein, the MnO_2/CNT nanocomposite electrode exhibited a higher specific capacitance and rate capability compared to CNT and pure MnO_2 electrodes. High specific capacitance obtained in the composite can be attributed to the high porosity of structure and high specific surface area.

Manganese oxides, as an environmentally friendly material with various oxidation states, have been used for a long time for electrode materials of batteries. The pioneering work on the pseudocapacitive behaviour of manganese oxide in an aqueous solution was published in 1999 by Lee and Goodenough [115]. Following this, several studies were performed to establish the charge storage mechanism in manganese oxide electrodes. Pseudocapacitive

(Faradic) reactions occurring on the surface and in the bulk of the electrode are the major charge storage mechanisms for manganese oxides. The surface Faradaic reaction involves the surface adsorption of electrolyte cations (H^+, Li^+, Na^+, and K^+) on the manganese oxide. The bulk Faradaic reaction relies on the intercalation or deintercalation of electrolyte cations in the bulk of the manganese oxide [116]. It is noted that, in both the mechanisms of charge storage, a redox reaction between the (+3) and (+4) oxidation states of Mn ions occurs. In general, hydrated manganese oxides exhibit specific capacitances within the 100–200 F/g range in alkali salt solutions, which are much lower than those for RuO_2.

Manganese (II, III, IV etc) oxides display poor electronic conductivity (10^{-5}–10^{-6} S/cm) due to which their application in high power performances continues to remain a major challenge. To improve the electrical conductivity of MnO_2 based electrode material, considerable research efforts have been invested towards the development of composite materials based on MnO_2 coupled with various conducting materials such as SnO_2 [117], conducting polymers [118], graphene [119], carbon nanotubes (CNTs) [120], and carbon [121] etc. In a report by Park et. al [121] the enhanced specific capacitance of thin film MnO_2 based electrode hybridized with an agarose gel (an ion-permeable and elastic layer coated on current collector) has been discussed [122].

Here, we discuss the capacitive behavior of the novel, co-electrodeposited Mn_2O_3-Au composite film using electrochemical characterization techniques. Since the CV plots of the co-electrodeposited sample for the second case exhibit higher current densities (of the order of mA), this sample was subsequently applied for studying electrochemical charge storage behavior. The detailed synthesis and materials characterization of the Mn_2O_3-Au composite and the pristine Mn_2O_3 have already been discussed in Chapter 3. For understanding its charge storage properties, our aim is to verify the electronic conductivity of the co-electrodeposited film after incorporation of metal nanostructure (Au). Since, both electronic and ionic transport properties along with charge transfer reaction at the electrode/electrolyte interface are required for better understanding of electrochemical behavior, a detailed investigation of these aspects have been performed. Electronic and ionic properties of the active electrode materials were characterized by Mott-Schottky (M-S) and electrochemical impedance spectroscopy (EIS) techniques and charge carrier concentrations in both the samples were obtained. CV on both samples was carried out in to compare their capacitive behavior. Furthermore, the frequency behavior of both the samples were studied to understand the supercapacitance property of the samples for possible charge storage application.

5.2 Electrochemical characterization and analysis

To investigate the mechanism for the enhanced electrical conductivity of Mn_2O_3–Au, Mott–Schottky (MS) measurements were obtained. This method was based on the Schottky barrier formation between the semiconductor material and an electrolyte [123]. The variation of the space charge capacitance (C_{sc}) was measured as a function of the applied potential. As shown in Fig. 5.2, both Mn_2O_3 and Mn_2O_3–Au samples exhibit a positive slope, indicating n-type semiconductor character. Carrier densities (N_d) of the samples were calculated using the following equation [124]. A detailed mathematical derivation of this formula has been discussed in chapter 2.

$$N_d = \frac{2}{\varepsilon\, \varepsilon_o e A^2} * \frac{dV}{dC_{sc}^{-2}} \qquad (1)$$

where ε is the relative dielectric constant of Mn_2O_3 (~1.5 × 104) [125], ε_0 is the permittivity of vacuum, V is the potential applied at the electrode, and A is the area of the electrode material. The ratio of the carrier densities of both the samples was calculated from equation (1) (with $A(Mn_2O_3) \sim 0.4\ cm^2$ and $A(Mn_2O_3\text{–}Au) \sim 0.36\ cm^2$ and the same ε for both the samples) and is inversely proportional to the slope of the MS plot of both samples. From this calculation, we have found that the carrier density of Mn_2O_3–Au is 3.7 times higher than the carrier density of the pristine Mn_2O_3 sample. Also, the carrier densities of both pristine and composite samples were calculated to be 2.1×10^{14} and 7.8×10^{14} cm^{-3}, respectively. In Mn_2O_3–Au composite films, Au is the source of extra charge carriers. In Fig. 5.2, we observe that the MS plot of Mn_2O_3–Au has a lower slope thereby representing the higher carrier concentration compared to pristine Mn_2O_3.

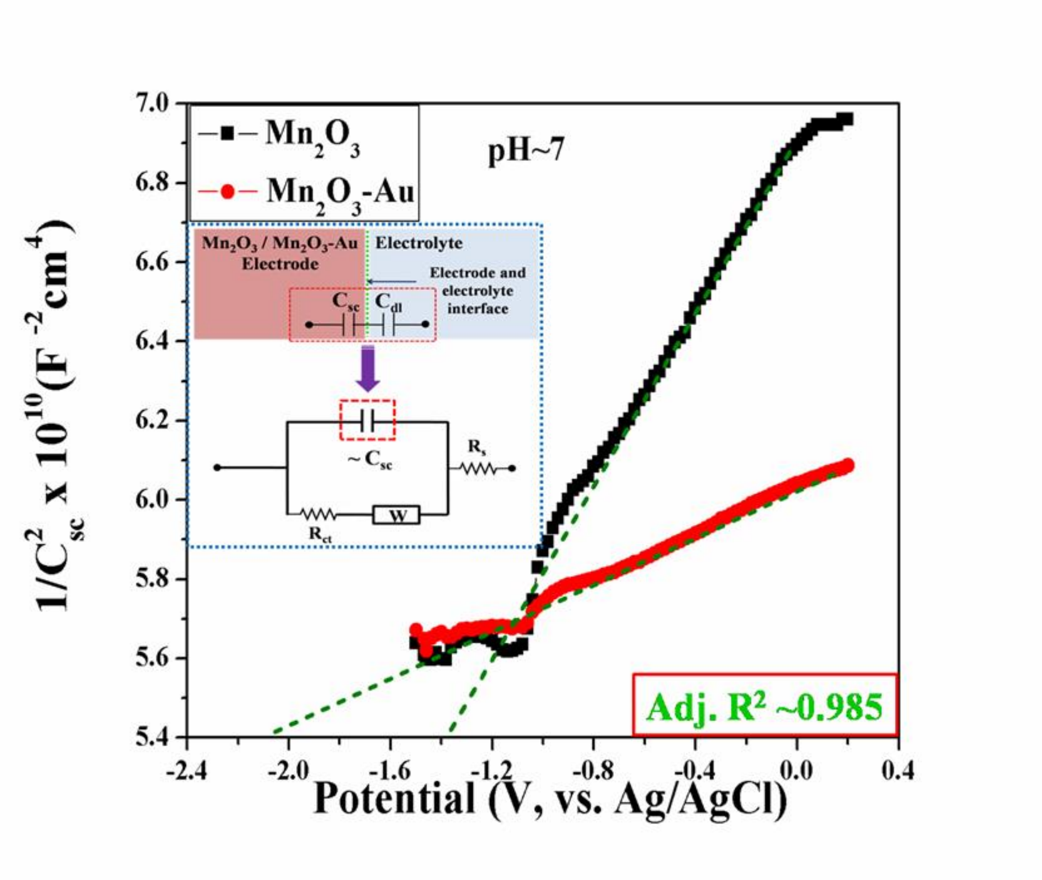

Fig. 5.2: Mott- Schottky plot of both pristine Mn_2O_3 and Mn_2O_3-Au. Inset schematic shows proposed Randle's circuit where capacitance is replaced by space charge capacitance (C_{sc}). Because both C_{sc} and double layer capacitance (C_{dl}, which is large than C_{sc}) are in series. So equivalent capacitance is C_{sc}. R_{ct}, W, and R_s are the charge transfer resistance, Warburg impedance and series resistance of the device respectively.

A higher charge carrier concentration in the composite sample has an influence on changing the work function of the material. This leads to a greater band bending, which enhances the charge transfer at the electrode electrolyte interface (as shown in Fig. 5.3).

Electrochemical impedance spectroscopy (EIS) was conducted to understand the conductivity of electrode material, charge transport in the electrode–electrolyte interface and mechanistic analysis of interfacial processes. Fig. 5.3 shows the Nyquist plot of both pristine Mn_2O_3 and Mn_2O_3–Au composite samples.

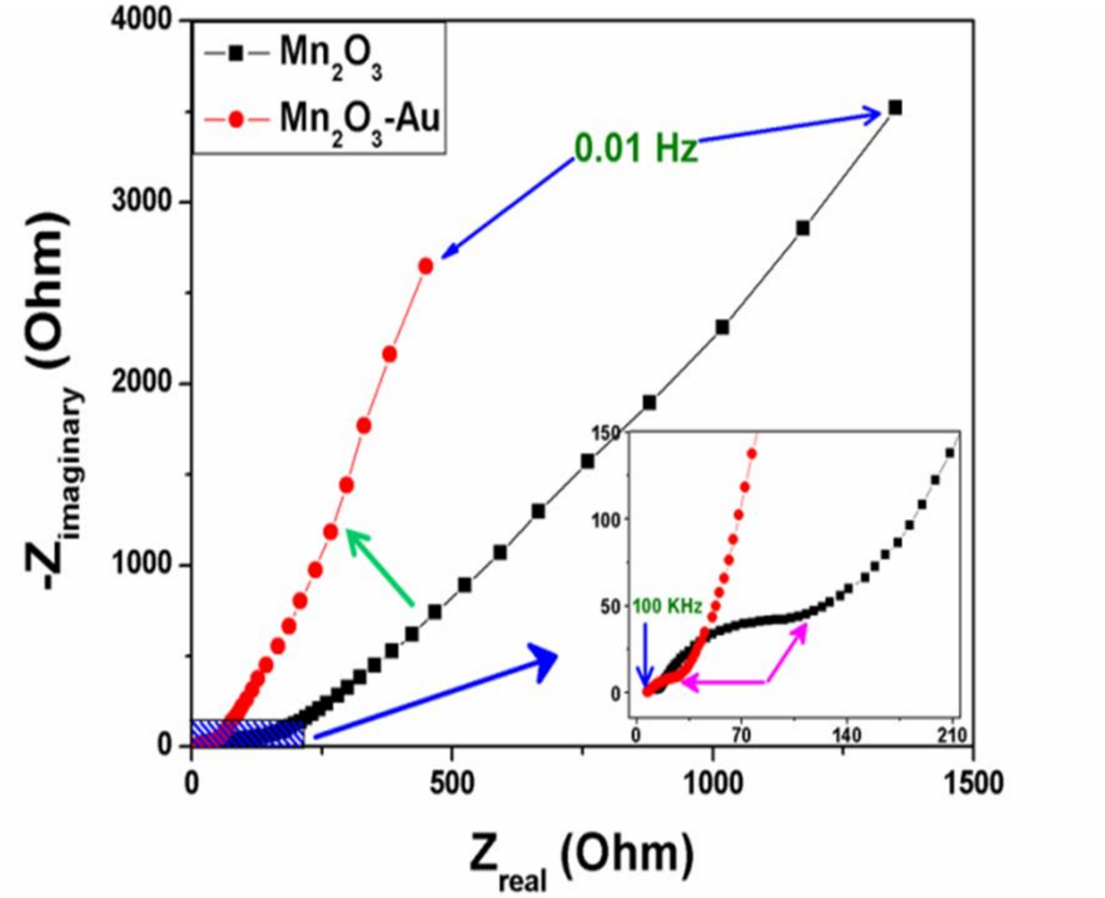

Fig.5.3: Comparative study of Nyquist plot and of both Mn_2O_3 and Mn_2O_3-Au sample.

These two plots display a semicircle in the high frequency region and a straight line in the low-frequency region, which corresponds to electron-transfer-limited and diffusion limited electron transfer processes, respectively. The inset graph shows the Nyquist plot of both the samples corresponding to a frequency range between 100 kHz to a few Hz. There are two intercepts of the semicircle to the real impedance axis at the high frequency region. At very high frequencies (~100 kHz), the intercept at the real part (marked with blue arrow in the inset graph of Fig. 5.3) is a combination resistance of the ionic resistance of the electrolyte, and the contact resistance at the active material/current collector interface [126]. These two intercepts show the two different values (~18 Ω for Mn_2O_3 and ~7.3 Ω for Mn_2O_3–Au). The decrease of this resistance value is attributed to the improvement of the current collector resistance (in both cases solution resistance is the same for the same solution) properties of the Mn_2O_3–Au sample because Au improves the interfacial resistance between the current collector (ITO) and active material (Mn_2O_3–Au). Hence, despite the higher molar concentration of manganese acetate used for the second co-electrodeposition process, it is interesting to note that the same concentration of $HAuCl_4$ is sufficient to improve the charge transfer behaviour of the composite film. Another major difference in the Nyquist plots is the arc of the semicircle in the high frequency range (marked with pink color arrow in the inset graph of Fig. 5.3), which corresponds to the charge-transfer resistance (R_{ct}) and is associated with the electronic properties of the porous electrode. The R_{ct} of Mn_2O_3–Au is (~30 Ω) much lower than R_{ct} of Mn_2O_3 (~130 Ω). The decrease of the charge transfer resistance of Mn_2O_3–Au is ascribed to the large number of charge carriers in the bulk of the same sample. These charge carriers are seen only because of the presence of Au inside the Mn_2O_3 which facilitates fastest electron transport and shortest ion-diffusion path inside the Mn_2O_3–Au sample. Another feature of the Nyquist plots is the straight line in the low frequency range (10 Hz to 10 mHz) which corresponds to the Warburg impedance [127] associated with the diffusion of ions inside the porous electrode material. Moreover, this straight line makes an angle (called the phase angle) with the Z_{real} axis. In our case, we observe that the Warburg impedance is lower in Mn_2O_3–Au compared to Mn_2O_3. This result indicates that Mn_2O_3–Au shows a better pseudocapacitive nature compared to Mn_2O_3. Furthermore, an increase in the phase angle (marked with green arrow) indicates the capacitive nature of the active electrode material. Thus, Mn_2O_3–Au shows much improved capacitance than the Mn_2O_3. This can be illustrated in details in the frequency dependent phase angle (Bode plot) plot of both Mn_2O_3 and Mn_2O_3–Au samples as shown in Fig. 5.4. The Bode plot (Fig. 5.4) can be separated into high, medium and low frequency regions. At the high frequency region (above ~300 Hz) the phase angle has a tendency to be close to zero and the characteristic behaviour of the samples in this region is like a resistor and at the low frequency region (below ~1 Hz) it indicates capacitive behaviour.

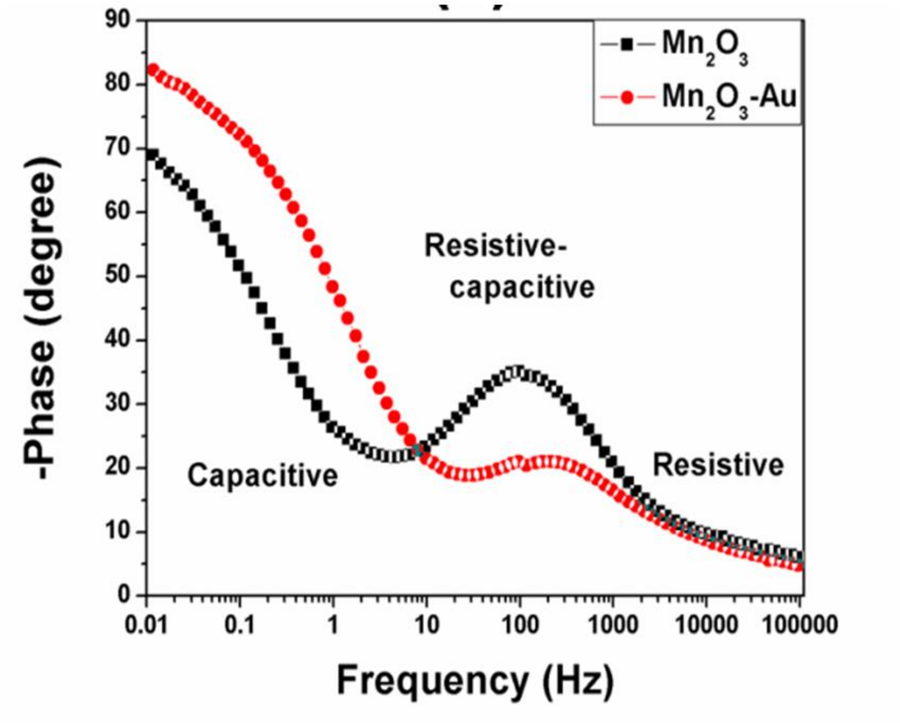

Fig. 5.4: Comparative study of frequency response on change in phase angle (Bode plot) of both Mn_2O_3 and Mn_2O_3-Au sample.

Approaching the phase angle towards −90° attributes behaviour like that of an ideal capacitor to the device [128]. In this case, the Mn_2O_3–Au sample shows a more capacitive nature than the pristine Mn_2O_3. The charge transfer resistance at the high frequency region is described already in Fig. 5.3. Between these two states both the samples behave as the R–C transmission line and in our case (above 10 Hz and below 2 KHz) two peaks are associated with the impedance of the R–C transmission line for the two samples. The higher peak intensity of the phase angle of Mn_2O_3 indicates its higher impedance compared to Mn_2O_3–Au and the frequency associated with the phase angle position of the two samples corresponds to the "Fig. of merit" of the respective samples. Mn_2O_3–Au shows that a higher "Fig. of merit" indicates a better ac response of the sample compared to Mn_2O_3.

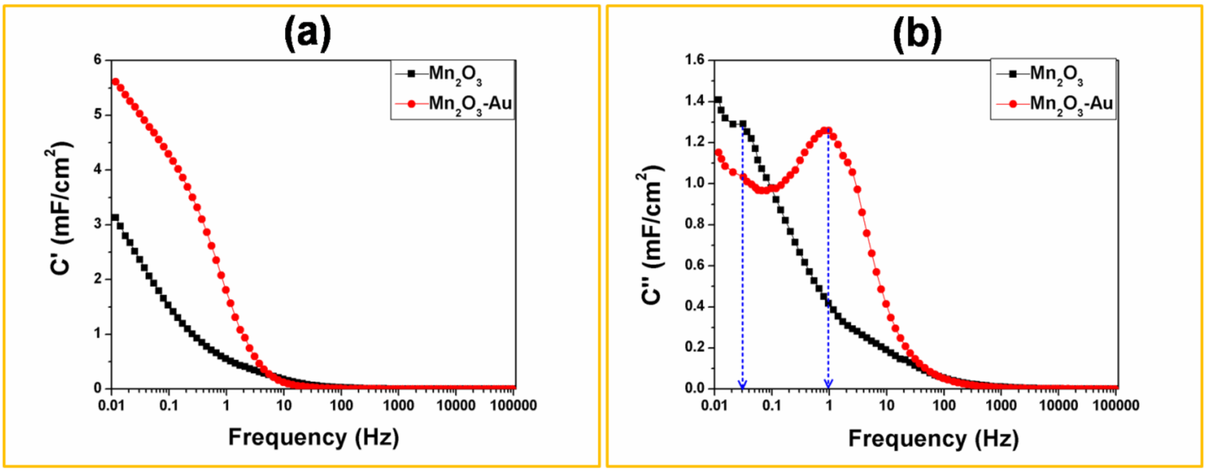

Fig.5.5: Analysis on the (a) real part of the capacitance vs. the frequency and (b) imaginary part of the capacitance vs. the frequency of both Mn_2O_3 and Mn_2O_3-Au.

Moreover, frequency analysis of the complex capacitance is performed to describe the capacitive nature of the electrode material [125] as shown in Fig. 5.5 (a) and (b). In Fig. 5.5(a), C′ represents the real part of the capacitance; it shows the variation of the available stored energy with the frequency. As we have described that the major portion of the capacitance is available only at a lower frequency, the same characteristics is obtained in both samples. In this case, Mn_2O_3–Au exhibits a higher capacitance than pristine Mn_2O_3. Fig. 5.5(b) shows the frequency behaviour of the imaginary part of the capacitance (C″) which represents the losses that occur during charge storage [127, 129]. This graph presents the capacitive dispersion related to energy losses. The peaks observed for each device can be used to determine the typical frequency attached to the relaxation time τ_0. This defines ion diffusion inside the bulk of the electrode material [128] and fast ion diffusion inside the material is attributed to the lower τ_o. The curved peaks (marked by the downward arrow in Fig. 5.5(b)) of the spectrum can be used to determine the relaxation time constant (τ_o) of the two samples. The time constant τ_o is calculated from the maximum frequency (f_p) using the equation $\tau_o = 1/f_p$ and the values are 50 and 1 s for Mn_2O_3 and Mn_2O_3– Au respectively. It is well known that higher power delivery corresponds to a lower τ_o value [129, 130] of the same sample. Hence, the presence of the Au nanostructure improves the supercapacitor power of Mn_2O_3–Au compared to Mn_2O_3. Fig. 5.6 shows a comparative study of the cyclic voltammograms (CVs) of both bare Mn_2O_3 and Mn_2O_3–Au films at a fixed scan rate of 0.06 V s^{-1}. In this Figure, we observe that Mn_2O_3–Au reveals the highest current compared to pristine Mn_2O_3. The enhancement of the current of Mn_2O_3–Au over the pristine film is ascribed to the effect of Au incorporation inside the Mn_2O_3. In Fig. 5.6, one can easily distinguish between two potential regions (0–0.5 V and 0.5–1 V) where the current density of both electrodes is independent of, and dependent on, the applied potential respectively. This means both electrodes exhibit a double layer capacitance in the potential range 0–0.5 V where capacitance (dQ/dV) is a constant and is independent of the voltage. Enhancement of the current and hence the charge storage capacity in this region is achieved by the increase of the overall surface area of the Mn_2O_3–Au sample because of the hierarchical Au nanostructure inside the Mn_2O_3 matrix. However, due to the low mass loading of our material, reliable BET measurements were not possible because it was difficult to measure the mass of the electrodeposited material. In the potential region 0.5–1 V, pseudocapacitance (dQ/dV is voltage dependent) is attributed to the faradic red-ox reaction which is confirmed by the red-ox peak identified by the blue arrow in Fig. 5.6. The enhancement of the pseudocapacitive peak current is much higher than the double layer current, so that we can say Au nanostructures not only increase the double layer current but also boost the faradaic current by a charge transfer process during the red-ox reaction. This faradaic charge transfer originates by a very fast sequence of reversible red-ox, electrosorption or intercalation processes. The presence of Au inside the Mn_2O_3 matrix can enhance the Faradic charge intercalation process and hence enhances the pseudocapacitance value. Moreover, both pseudocapacitance and double-layer capacitance contribute individually to the total capacitance value of the supercapacitor. As expected, the Mn_2O_3–Au composite electrodes exhibited a significantly higher charge storage capacity than pristine Mn_2O_3. The charge-storage mechanism of the MnO_2 based material is described in references [131, 132]. The mechanism is based on surface adsorption of electrolyte cations (Na^+) as well as proton incorporation according to the reaction:

$$\mathrm{MnO_2 + xNa^+ + xe^- \leftrightarrow MnO_2(xNa)} \qquad (2)$$

Pseudocapacitance is associated with the faradic charge transfer process between the Mn_2O_3–Au electrode and electrolyte (Na_2SO_4). The enhancement of the pseudocapacitive current is described schematically in Fig. 5.7. Au nanostructures have a large number of free surface charges which take part in the reversible faradic red-ox reaction process as described in the above equation. Enhancement of the pseudocapacitive current is measured by CV analysis of the Mn_2O_3–Au sample. During the cathodic potential scan (1 V to 0 V), electrons from ITO (e_{ITO}^-) and extra surface charge from Au (e_{Au}^-) (no structures exactly play the main role for Na+ ion insertion) inside the Mn_2O_3 through the Faraday reduction reaction mechanism. Conversely, both these electrons come back to the ITO through the oxidation reaction (in anodic potential scan 0 V to 1 V); as a result, the enhancement of the oxidation current is observed in the same sample. Therefore, the overall enhancement of pseudocapacitive current (through the faradaic red-ox reaction) of the Mn_2O_3–Au sample compared to pristine Mn_2O_3 is ascribed. So, the faradaic red-ox reaction which occurs in the Mn_2O_3–Au sample can be proposed as the following:

$$Mn_2O_3 + (x+y)Na^+ + (xe^-_{ITO} + ye^-_{Au}) \leftrightarrow Mn_2O_3[(x+y)Na] \qquad (3)$$

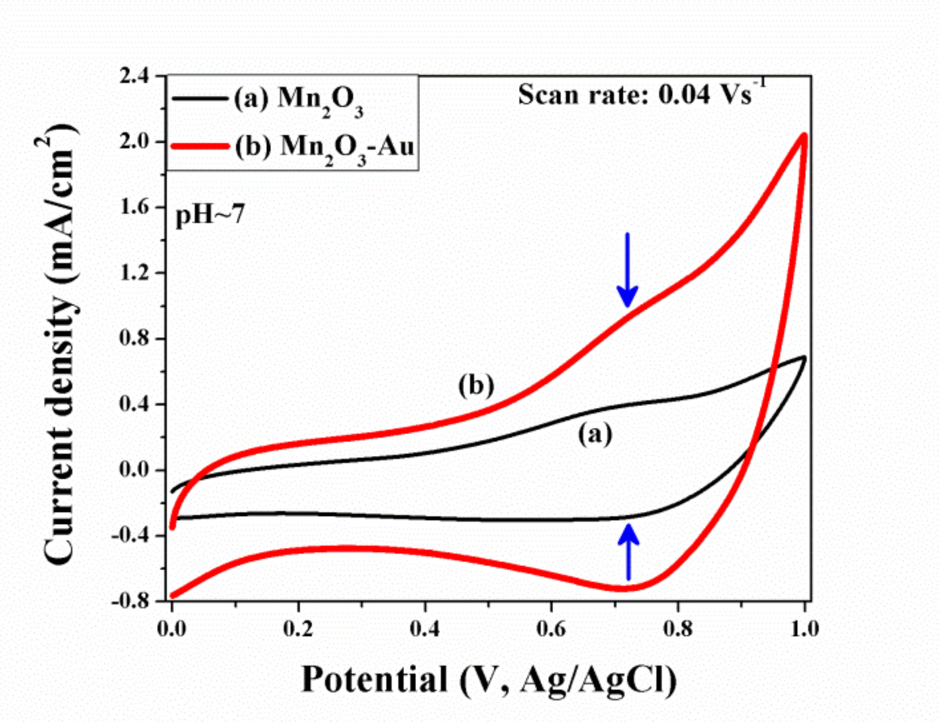

Fig.5.6: CV profile of both pristine and composite sample at a fixed scan rate of 0.04 Vs^{-1}.

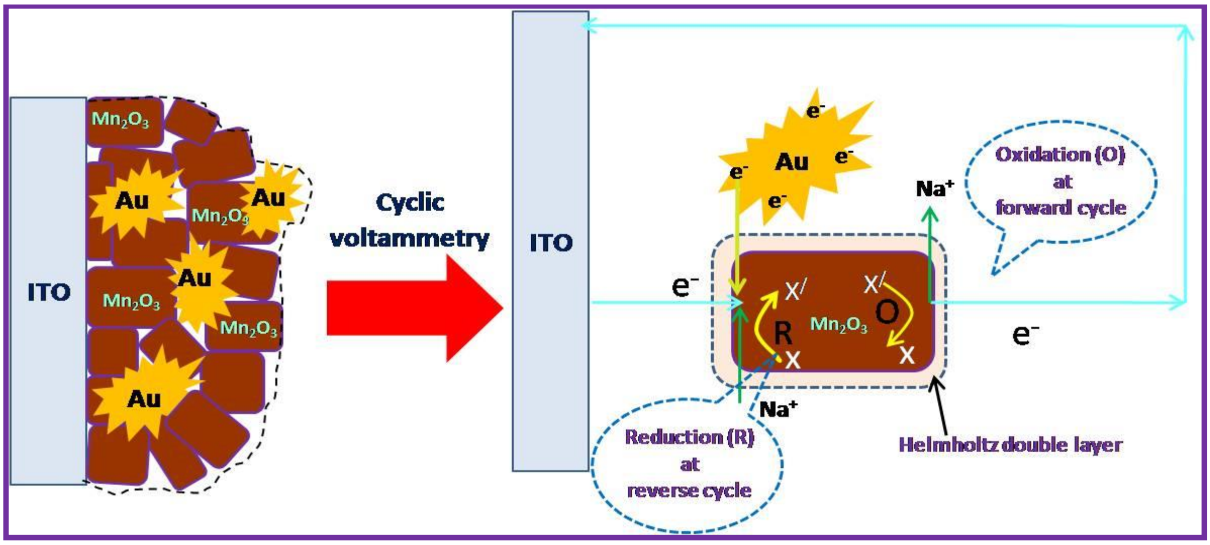

Fig. 5.7: Schematic representation of enhanced pseudocapacitive current of Mn_2O_3-Au.

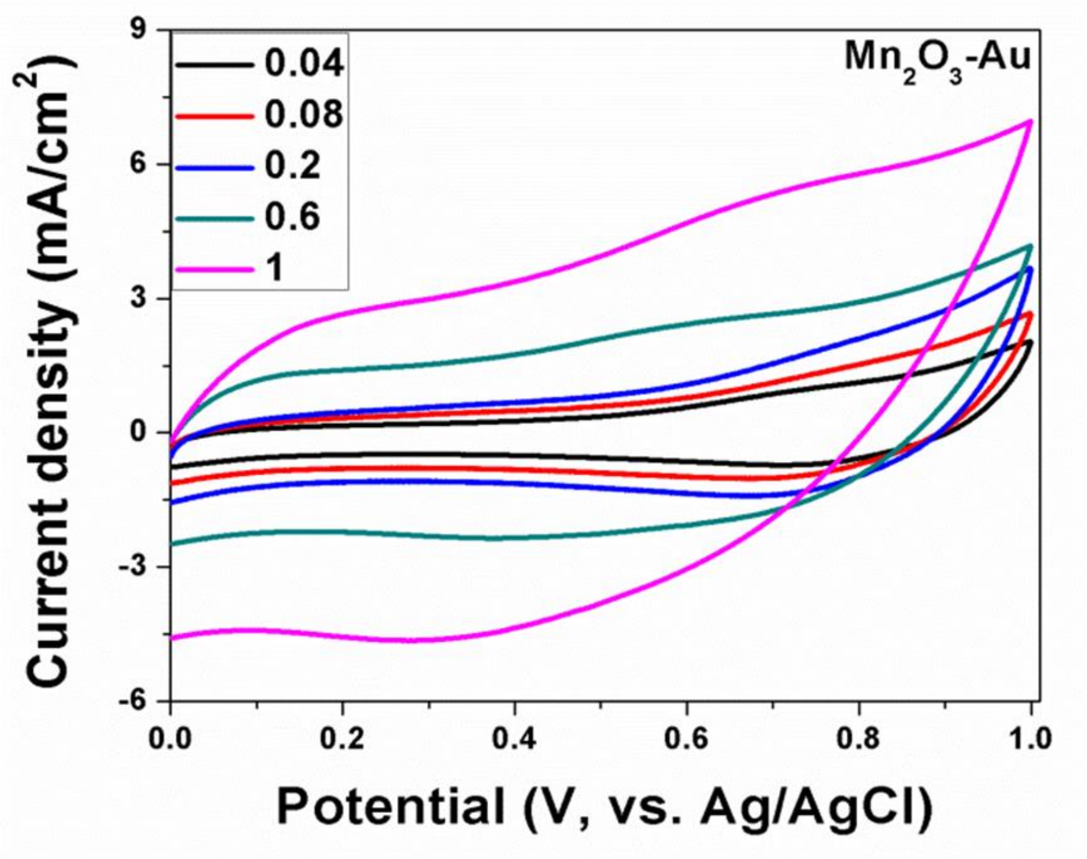

Fig.5.8: CV curves of Mn_2O_3-Au sample at different scan rate.

Scan rate dependent (0.02 to 1 V s^{-1}) CVs of the sample Mn_2O_3–Au is shown in Fig. 5.8. The shape of the CV curves is identical at all scan rates. These curves also indicate the fast ion diffusion inside the electrode material which induces the enhancement of charge storage capacity through the faradaic process [133].

1.3.Conclusions:

In summary, we have discussed the electrochemical charge storage application of the one step co-electrodeposited Mn_2O_3–Au composite material corresponding to the second set of electrolyte precursor concentration. Our analysis shows, that despite the higher concentration of manganese acetate used in this case, the same molar concentration of $HAuCl_4$, is sufficient for reducing the interfacial charge transfer resistance. The excellent performance of the Mn_2O_3–Au electrode can be ascribed to the following reasons: (1) an urchin-like gold nanostructure embedded in Mn_2O_3 increases the effective surface area as well as efficient ion intercalation/ de-intercalation, which can be attributed to the improved charge storage capability of the composite sample compared to pristine Mn_2O_3; (2) the highly conducting metal nanoparticles provide an effective pathway for charge transport; and (3) the binder-free device fabrication enables a low interfacial resistance and fast electrochemical reaction rate. Moreover, frequency response analysis of the Mn_2O_3–Au sample also confirms the superior charge storage properties of the sample, which can be used as an electrode material for supercapacitor applications.

CHAPTER 6

Chapter 6

A systematic approach for electrochemical characterization of drop-casted films: CdS nanorods

6.1 Introduction

In this work, we study the electrochemical performance of drop casted Cadmium Sulphide (CdS) coated Indium Tin Oxide (ITO) working electrode without enzyme immobilization for the detection of H_2O_2 and glucose. Electron transfer is an integral part of biological and chemical systems. One of the fields that offers great potential for electron transfer applications is that comprising redox enzymes and proteins. The electronic coupling between redox enzymes and electrodes for the construction of amperometric biosensors can be realized based on the electroactivity of the enzyme in the presence of biomolecules like glucose. Amperometric glucose biosensor can be categorized as 1st, 2nd, and 3rd generation based on their sensing principle using glucose oxidase (GOx). The technology for 3rd generation amperometric glucose sensing which is based on direct electron transfer (DET) process is already well developed and the mechanism of DET is a widely accepted strategy for enzyme based biosensing. In DET based glucose sensors, GOx is immobilized on the working electrode which is subsequently studied in the absence of an external mediator and redox couple. However, DET is not a commonly observed phenomenon. This is because the redox active centers of GOx such as the redox-active cofactor, flavin adenine dinucleotide (FAD) are usually shielded by the protein core which inhibits an efficient electron tunneling to the electrode surface. [136]. Furthermore, electron transfer through a tunneling mechanism is rarely encountered [137]. With the aim to overcome the above-mentioned disadvantages associated with GOx based DET systems, we wish to explore an alternate mechanism of glucose detection by dissolving GOx in PBS instead of immobilizing on working electrode. Recently, CdS based nanostructures for biosensor applications have been extensively investigated because of its 2D layer structures and excellent physicochemical properties. Moreover, these can be considered as being very important in electrochemical bio-sensing applications since they exhibit enhanced redox activity due to higher charge detaching efficiency and synergetic effects [138-141]. Zhu and co-workers have developed a novel label-free biosensor of CdS nanoparticles with co-reactant $K_2S_2O_8$ for the detection of low density lipoprotein [142]. Wang and co-workers have demonstrated that the CdS nanoparticles formed on the surface of multi-walled carbon nanotubes can react with the co-reactant of H_2O_2 in a neutral PBS solution [143]. Moreover, there is a recent report on the H_2O_2 sensor using other chalcogenides such as NiS nanostructures. [144].

Herein, we have used CdS coated ITO as the working electrode for electrochemical detection of H_2O_2 which is generated by glucose oxidation in the presence of GOx in the electrolyte. The main advantage of this technique is that, GOx is dissolved in the buffer and hence doesn’t suffer from any drawbacks associated with enzyme immobilization. Furthermore, electrochemical detection of H_2O_2 through electrocatalytic process by CdS electrode can be efficiently obtained without any electron shuttling at the interface, and as per our knowledge the onset potential (-0.2 V, vs. Ag/AgCl) for electrocatalytic process is lower compared to the reported value [145]. Moreover, a systematic optimization protocol for working electrode and electrolyte was carried out to achieve the enhanced electrochemical sensing performance.

6.2 Experimental:

6.2.1. Materials and characterizations

Cadmium Nitrate Tetrahydrate ($Cd(NO_3)_2.4H_2O$), thiourea, ethylene diamine, disodium hydrogen phosphate (Na_2HPO_4), sodium dihydrogen phosphate (NaH_2PO_4), ethanol, H_2O_2 30% w/w, D- Glucose, Ascorbic Acid (AA), Uric Acid (UA), potassium ferricyanide [$K_3Fe(CN)_6$], potassium ferrocyanide [$K_4Fe(CN)_6$] were obtained from Merck India Ltd and Dopamine (DA) from Sigma Aldrich. Chitosan (weight 100,000-300,000) was procured from Acros organics. Distilled water from Merck Millipore system with conductivity of 18.2 $MOhm^{-1}cm^{-1}$ was used during materials synthesis and their electrochemical measurements. All chemicals were analytical grade and used as obtained without further purification.

The X-ray diffraction (XRD) studies were conducted using Bruker AXS D8. Electron microscopy measurements, energy dispersive X- ray spectroscopy (EDS), and elemental mapping were performed with SEM FEI. The electrochemical characterizations were performed using CHI 660C electrochemical workstation with a standard three electrode configuration. The CdS/ITO was used as the working electrode, Pt wire as the counter electrode and Ag/AgCl as the reference electrode.

6.2.2 Synthesis of CdS Nanorods

CdS nanorods were synthesized following a previously reported hydrothermal procedure [146]. Briefly, 2.776 gm of $Cd(NO_3)_2.4H_2O$ and 2.055 gm of thiourea were dissolved in 80 ml of ethylene diamine with half an hour of constant stirring. After this, the mixture was transferred into a 100 ml Teflon lined steel autoclave and placed inside a preheated furnace at 200 ^oC. The mixture was allowed to react for 12 h. Next, the autoclave was cooled down to room temperature. Finally, the products were thoroughly washed with ethanol and distilled water 7-8 times and dried in vacuum oven at 50 ^0C for 8 h.

6.2.3. Preparation of working electrodes for electrochemical measurement

Prior to the fabrication of working electrode, ITO substrates were cut into fixed dimension (1 cm X 1 cm). Then, these substrates were thoroughly cleaned by ultrasonication in ethanol and distilled water for 15 mins each followed by drying in air at room temperature. Slurry was prepared with CdS NR powder sample and chitosan solution (dissolved in 1 wt% acetic acid). After this, 10 µL of the suspension was drop casted on the conducting side of the ITO sheet and dried in air at room temperature for further use. The effect of CdS loading and binder quantity were studied to analyze their influence on the electro-catalytic properties. The results have been discussed in the subsequent text.

6.2.4. Electrochemical characterizations

A series of cyclic voltammetry (CV), amperometric I-t, and electrochemical impedance spectroscopy (EIS) measurements were performed to evaluate the electrochemical sensing performance of the CdS NR modified ITO electrode for hydrogen peroxide and glucose. The molar concentration, temperature, and pH of PBS buffer along with the concentration of CdS NR coated on ITO, and amount of chitosan used to bind CdS with ITO were optimized systematically. Furthermore, optimizing the concentration of GOx dissolved in PBS and a comparative analysis of glucose sensing behavior with GOx immobilized CdS working electrode was carried out. The reproducibility, long term stability and interference studies with other analytes of the CdS/ITO electrode were also studied.

6.3. Results and discussion:

6.3.1. Structural characterizations of CdS nanostructures

The structure of the as prepared CdS sample was determined using powder XRD. Fig. 1a shows the XRD pattern with peak positions at 2θ values of 24.7 °, 26.4 °, 28.17 °, 36.3 °, 43.55 °, 47.8 °, and 51.77 ° corresponding to the (100), (002), (101), (102), (110), (103), and (112) planes of hexagonal phase of CdS (JCPDS no. 06-0314) [147]. To ascertain the morphology, scanning electron microscopy was performed. Fig. 1b shows the electron micrographs revealing a nanorod morphology with an average length of few hundred nanometers and diameter ~ 30 nm. EDX elemental color mapping as seen in Fig. 1b demonstrates that cadmium and sulphur are homogeneously present in the sample and Fig. 1c depicts the EDX spectrum confirming the presence of the elements cadmium and sulphur in the prepared sample.

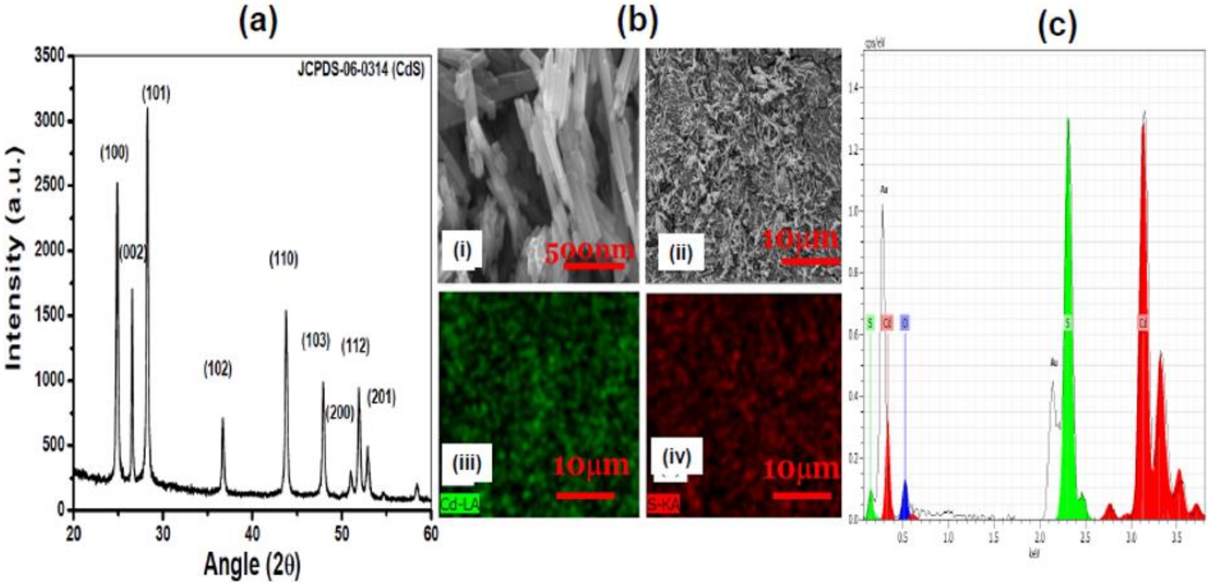

Fig. 6.1:(a) XRD plot of CdS nanorods, (b) SEM image of CdS nanorods with two different scales (i) 500 nm, (ii) 10 nm, elemental color mapping to show homogeneity at 10 μm scale of (iii) Cadmium and (iv) Sulfur, (c) EDX spectrum indicating the presence of Cadmium and Sulphur in the sample. (Au signal is due to the gold sputtering performed during SEM measurement.)

6.3.2 Electrochemical characterizations

6.3.2.1 Electrochemical H_2O_2 reduction studies by CdS/ITO electrode: Optimization of electrochemical reduction

Interfacial charge transfer behavior of CdS coated ITO electrode was investigated through EIS and the measurement was conducted in an equimolar (5 mM) mixture of potassium ferri/ferrocyanide dissolved in PBS electrolyte. This EIS plot is depicted in Fig. 2a and the inset represents the equivalent Randle circuit for the two cases.

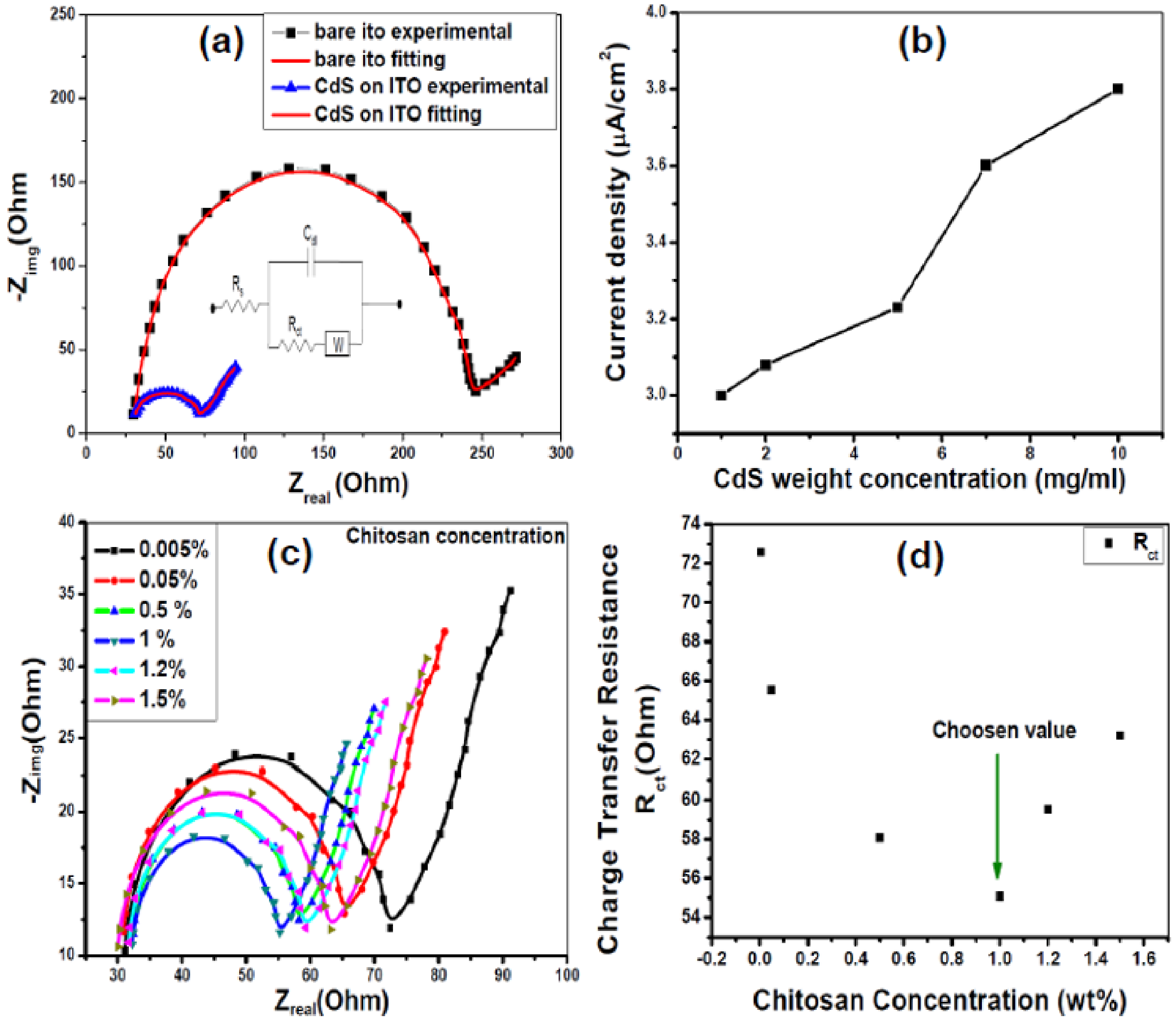

Fig. 6.2: (a) EIS spectra of bare ITO and CdS coated ITO along with equivalent Randle Circuit in the inset, (b) calibration plot between electro-reduction current density as a function of CdS weight, (c) EIS spectra for varying concentrations of chitosan solution and (d) the corresponding plot of charge transfer resistance as a function of chitosan concentration.

The reduced charge transfer resistance (R_{CT}, second intercept of the semicircle) of the CdS/ITO electrode is 75 Ohms as compared to 250 Ohms of the bare ITO substrate. Therefore, CdS/ITO electrode has better electron transport ability compared to bare ITO. Next, the H_2O_2 electro-reduction current was optimized w.r.t the concentration of CdS slurry. CV was conducted in PBS (pH ~7) in the absence and presence of H_2O_2 within a voltage range from -0.3 to 0.1 V at a scan rate 50 mV/s. Sample concentration of 5 mg/ml was chosen for subsequent studies since at higher values the sample had a tendency to flake off. The plot of electro-reduction current density with respect to the CdS loading has been depicted in Fig. 6.2(b). In the next step, the concentration of the chitosan solution was varied for 5 mg/ml CdS slurry to determine the optimum concentration of chitosan and the charge transfer properties in potassium ferri/ferrocyanide electrolyte mixture were examined using different concentrations of chitosan. A comparative EIS plot for varying chitosan concentration is shown in Fig. 6.2(c). As we can see, from Fig. 6.2(d), the charge transfer resistance is first decreases for an increase in chitosan concentration from 0.005 to 1 wt%. This could be due to an improved dispersion of the CdS sample in the chitosan solution, thereby, providing a better coverage and film formation on the ITO substrate resulting in an improved charge transfer behavior. However, beyond a concentration of 1 wt%, the charge transfer resistance increases, as evident from the EIS plot (Fig. 6.2(c)) (light blue curve) and this trend continues for further increase in chitosan concentration. Hence, even though chitosan is conducting, and is a commonly used polymer for drop casting [148, 149, 150], beyond a threshold concentration it has a blocking effect which is detrimental for charge transfer at electrode-electrolyte interface [151].

This is in agreement with the electroreduction behavior of H_2O_2 (Fig. 6.3(a)), implying that the optimization of binder concentration is an important pre-requisite towards efficient electrochemical sensing for drop casted films. The subsequent characterizations for H_2O_2 sensing, is undertaken with CdS slurry concentration of 5 mg/ml and chitosan solution concentration of 1 wt%. While tuning the properties of the electrode, the molar concentration, pH and temperature of the electrolyte were maintained as same. This is because, for a given set of parameters, the electrode properties showed the same trend. The detailed optimization of electrolyte concentration, operating temperature and pH of the electrolyte has been performed for obtaining optimum characterization conditions (Fig. 6.3, Fig. 6.4).

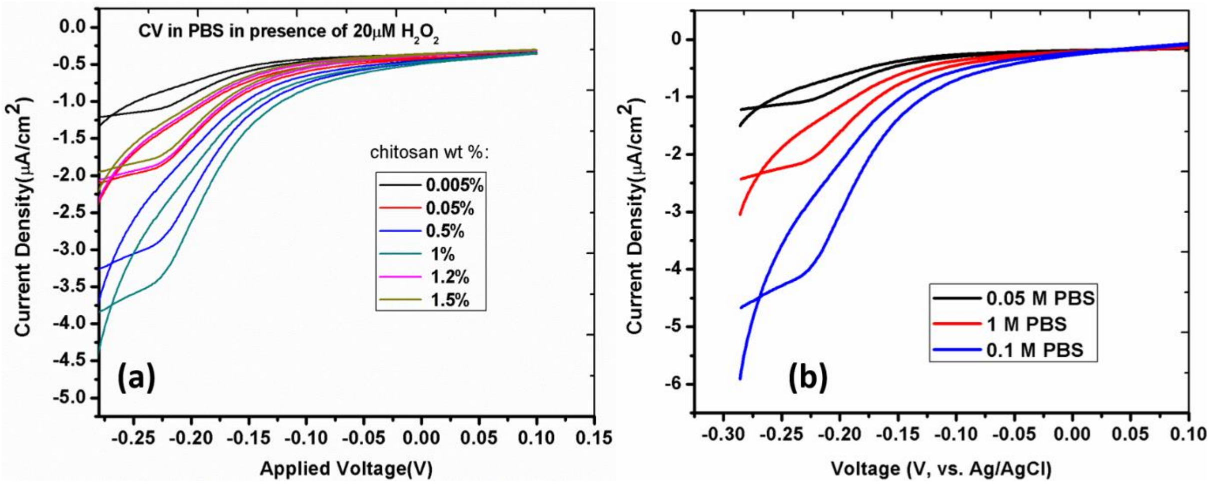

Fig. 6.3:(a) CV response CdS/ITO in presence of 20 μM H_2O_2 for increasing chitosan concentration for preparing drop casted electrode (b)CV response of CdS/ITO in presence of H_2O_2 for varying Electrolyte concentration

After optimization of the electrode and electrolyte parameters, the experiments for H_2O_2 electroreduction using CdS nanostructures were carried out at room temperature and the results are shown in Fig. 6.5. Fig. 6.5(a) and (b) show the CV responses for increasing concentration of H_2O_2 and at increasing scan rates for 20 µM H_2O_2 in PBS (pH ~ 7), respectively. Fig. 6.5(c) reveals the linearity in concentration vs. reduction current in the range between 10 µM and 30 µM and the calibration curve fits with the equation $J = -0.13749C_{H2O2} + 1.81878$. Furthermore, the reduction current bears a linear relationship with the square root of scan rate as can be seen from Fig. 6.5(d), indicating a diffusion controlled electro-reduction process [152].

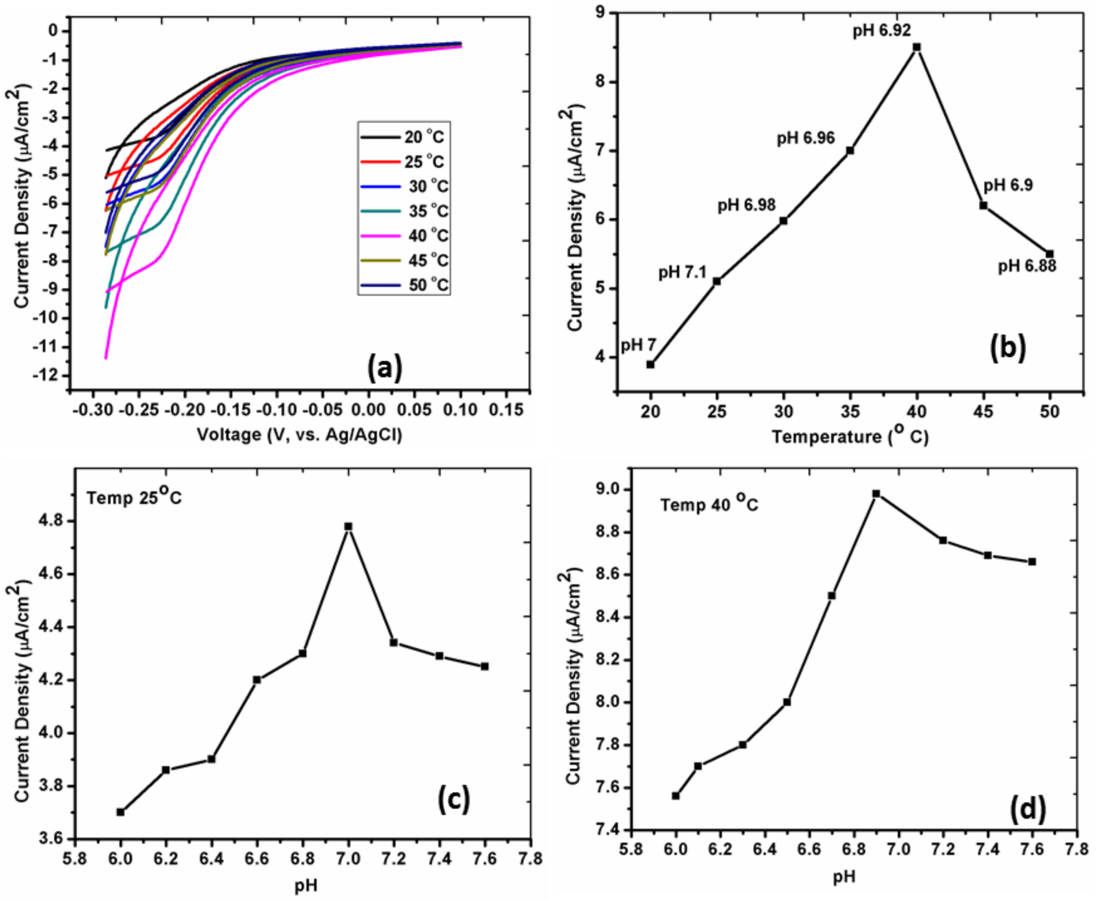

Fig. 6.4 (a)CV response of in presence of 20 μM H_2O_2 for different operating temperatures and the (b)corresponding plot of electro-reduction current density as a function of temperature and the corresponding values of pH (c) plot of current density as a function of pH, for increasing values of pH at room temperature, i.e.25°C, (d) plot of current density as a function of increasing values of pH at 40°C.

Subsequently, the calibration curve for H_2O_2 sensing were obtained from the amperometric I-t measurements performed at -0.22 V, with successive additions of fixed quantities of increasing molar concentrations of H_2O_2 added successively with PBS.

The amperometric response and the corresponding calibration graph are depicted in Fig. 6.5(e) and (f), respectively, showing a linear response up to 225 μM. The calibration data fits well with the linear equation $J = -1.436C_{H2O2} -0.1236$. A sensitivity of 1.436 μA/μM cm^2 was obtained from the calibration curve corresponding to the amperometric response of Fig. 6.5(e). The limit of detection (S/N=3) was estimated to be 0.08 μM. A comparison of the performance of our electrode with some of the previous reports on sulfide and horseradish peroxidase based

H_2O_2 sensors and the results are presented in Table 1. The high sensitivity of our CdS electrode is in agreement with its peroxidase like nature [153].

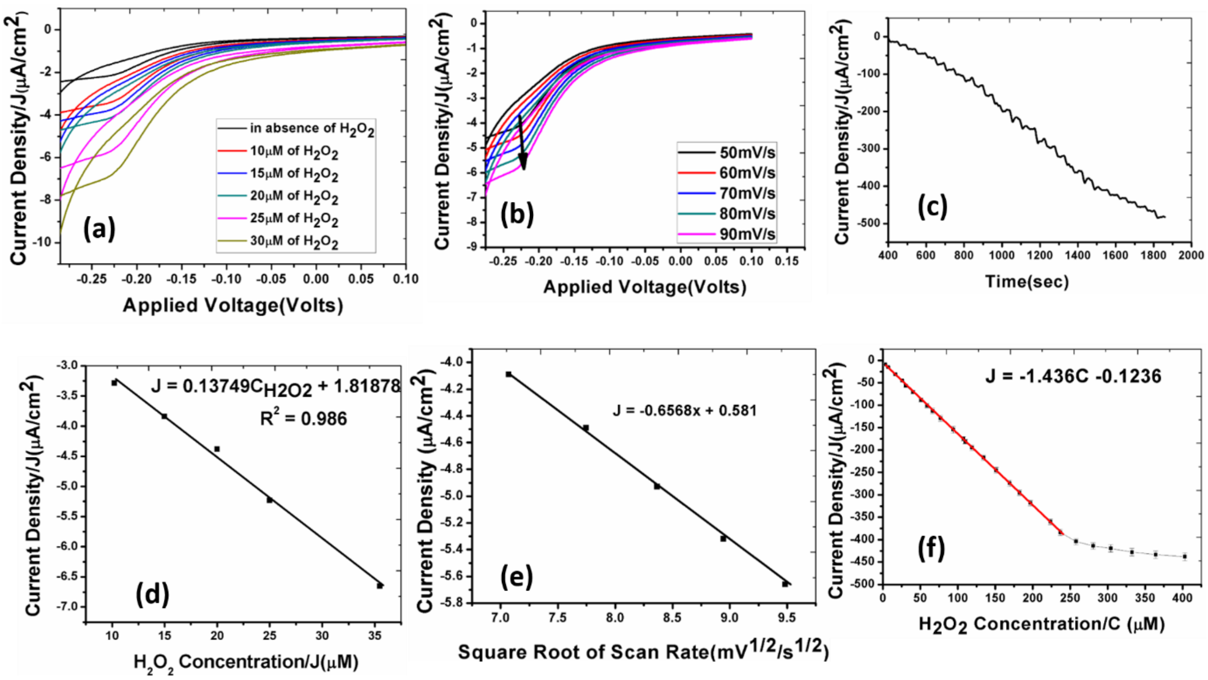

Fig. 6.5: (a) CV plot of CdS/ITO for increasing concentration of H_2O_2 (b) CV plot of CdS/ITO for increasing values of scan rate (c) amperometric I-t response for increasing molar concentration of H_2O_2, (d, e, f) calibration plot corresponding to (a), (b), and (c), respectively.

The performance of CdS working electrode towards H_2O_2 detection has been compared with Mn_2O_3-Au composite [154], FeS [155], CuS [156], and HRP [157].

Table 1 Comparative performance of previously reported H_2O_2 sensors with our work:

Sample	Linear Range	Sensitivity	LOD	Reference
Mn_2O_3-Au	10-500μM	39.24μA/mM cm^2	0.34μM	154
FeS on glassy carbon	5-140μM	0.85μA/mM	43μM	155
CuS	10-1900μM	62.93μA/mM	1.1μM	156
HRP	4-100μM	2.8μA/mM	1.6μM	157
CdS nanorod	2-225μM	1.436μA/μMcm^2	0.08μM	Our work

6.3.2.2 Glucose dissociation by GOx and selective detection of byproduct (H_2O_2) through AET by CdS/ITO

Here we want to establish an alternative electron transfer (AET) process and compare the results with those obtained using GOx immobilized CdS/ITO electrode. For testing the AET process we have prepared an electrolyte mixture comprising of 0.1 M PBS (pH~7) and GOx (1 mg/ml) for studying electrochemical glucose sensing on CdS/ITO working electrode. The chosen value of GOx concentration was based on a series of control experiments by varying of its concentration. The results have been depicted graphically in Fig. 6.6. A set of cyclic voltammetry measurements for increasing molar concentration of glucose and increasing scan rate with fixed glucose concentration were performed and the corresponding results along with the calibration plots are shown graphically in Fig. 6.7.

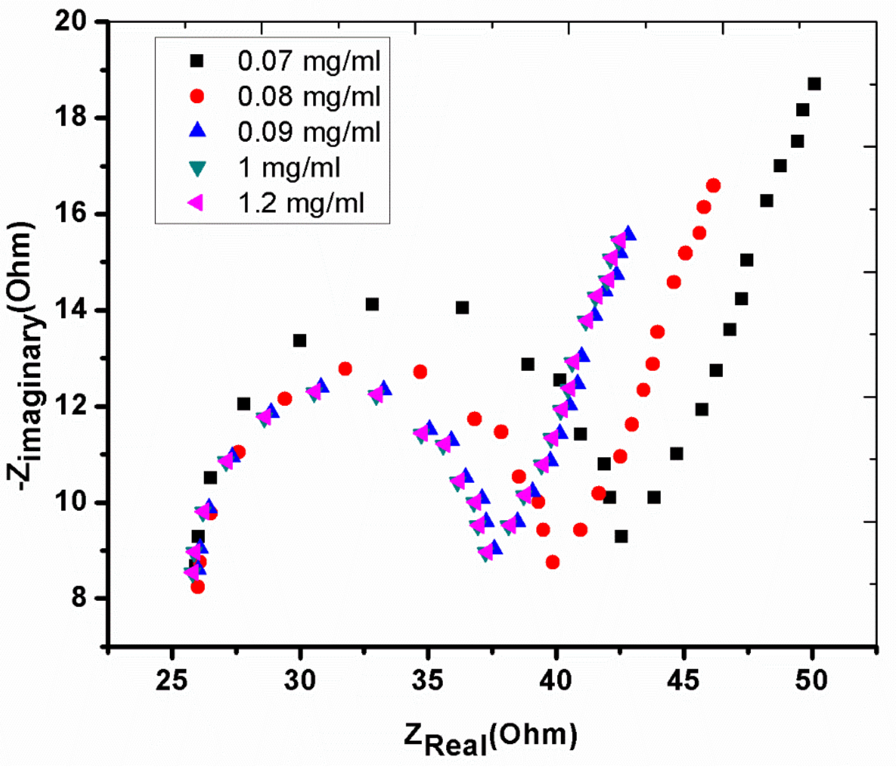

Fig. 6.6: EIS spectra revealing optimization of molar concentration of GOx dissolved PBS for performing AET studies

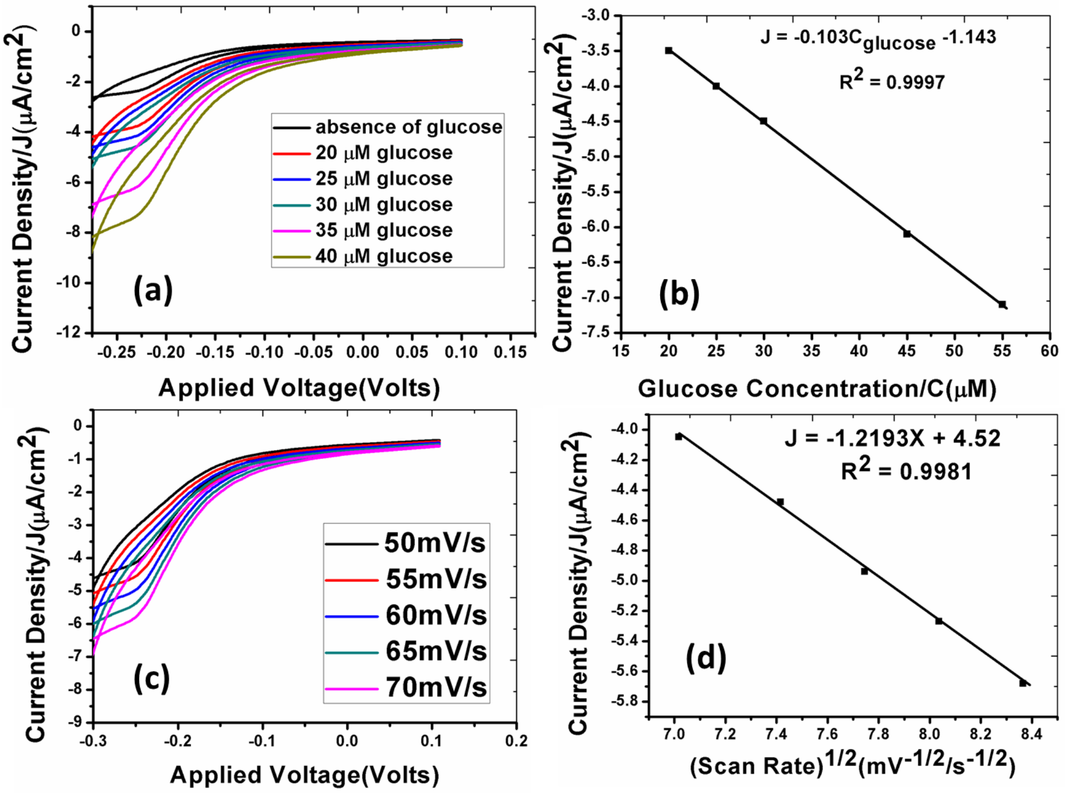

Fig. 6.7: (a) CV plot CdS/ITO in AET set-up for increasing molar concentration of glucose, (b) calibration plot corresponding to (a), (c) CV plot for increasing values of scan rate and (d) calibration plot corresponding to (c)

The glucose sensing was based on the electrochemical detection of H_2O_2, generated from glucose oxidation, in presence of the glucose oxidase in the buffer solution via the following process [158].

$$Glucose + O_2 \rightarrow Gluconic\ Acid + H_2O_2 \qquad (1)$$

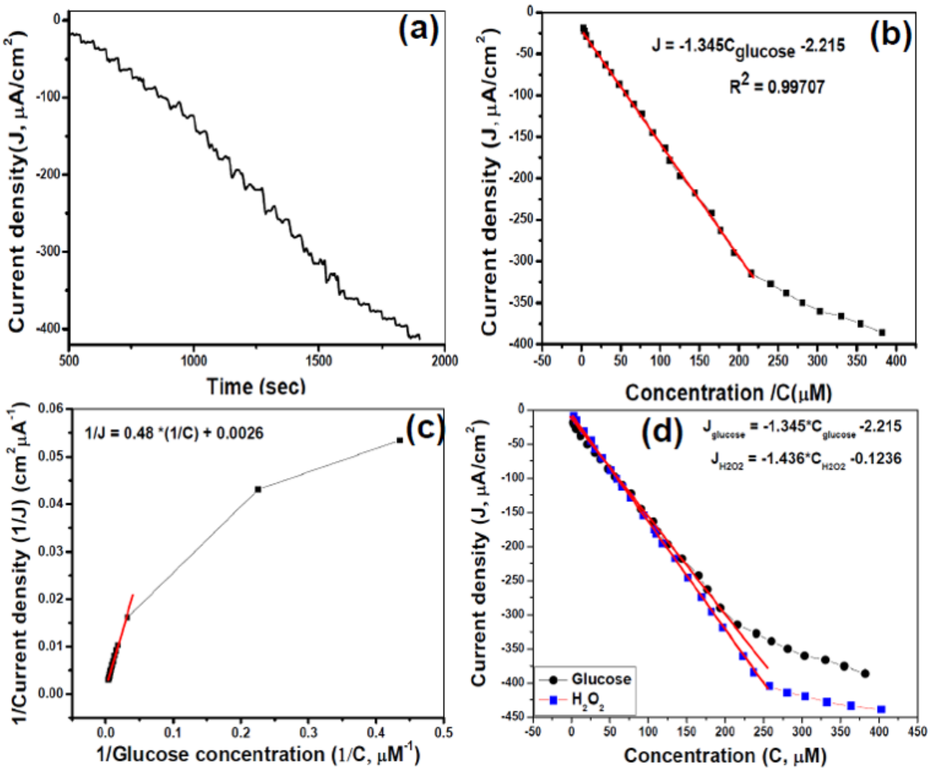

Fig. 6.8: (a) Amperometric I-t response for increasing glucose concentrations (b) current vs. glucose concentration calibration curve as obtained from amperometry, (c) Lineweaver-burk plot of inverse of current vs. inverse of concentration, and (d) comparison of calibration curve of electroreduction of both glucose and H_2O_2 by CdS nanostructure.

Glucose dissociates into gluconic acid and H_2O_2 in the presence of GOx, which is dissolved in the PBS electrolyte. H_2O_2 is reduced further at the CdS coated electrode and a possible reaction mechanism may be understood by both the cyclic voltammetry curves and the peroxidase mimic nature of CdS [155]. By virtue of its peroxidase mimicking nature, CdS should be converted into an intermediate by oxidation process with the simultaneous reduction of H_2O_2 into water [155, 158]. In the reverse scan, the CdS catalyst maybe further regenerated. Fig. 6.7(a) shows CV of different concentrations of glucose oxidation through intermediated H_2O_2 reduction at CdS surface. Fig. 6.7(b) represents linear variation of reduction current with different glucose concentrations and the linear variation of reduction current fits well with the equation: $J = - 0.103C_{glucose} - 1.143$. The linear response of the electroreduction behavior as a function of square root of increasing scan rate depicts its diffusion controlled electroreduction behavior shown in Fig. 6.7(c) and (d).

Amperometric I-t studies were conducted with successive addition of glucose solutions of increasing molar concentrations at regular intervals of 100 s up to 400 µM. The current vs. glucose concentration calibration curve has been obtained from amperometry (Fig. 6.8(a)) and the following calibration curve is shown in Fig. 6.8(b). The sensitivity towards glucose detection as determined from the amperometric I-t calibration plot by fitting the linear equation $J = -1.345*C_{glucose} - 2.215$ is obtained as 1.345 µA/µM cm^2 with a low detection limit of 0.1 µM (S/N=3) was obtained towards glucose sensing. From Fig. 6.8(c), we see the saturation in the current beyond 225 µM glucose which is a typical characteristic of Michaelis Menten mechanism from which the apparent Michaelis Menten constant can be obtained by using the Lineweaver-Burk model [156].

Mathematically, it is expressed as:

$$1/I_{ss} = 1/I_{max} + K_m / (I_{max} \times [S]) \qquad (2)$$

Where, I_{ss} is the steady state current, I_{max} the maximum current measured under conditions of enzyme saturation and [S] is the concentration of analyte. A plot of $1/I_{ss}$ vs 1/[S] is shown in Fig. 6.8(c). The values of the slope and the intercept correspond to K_m/I_{max} and $1/I_{max}$ respectively. Hence, the value of the apparent Michaelis Menten constant K_m was found to be 184 µM. This is comparatively lower than most other previously reported values [159, 160, 161, 162] of enzymatic glucose sensors suggesting that our working electrode – electrolyte set up shows a strong affinity towards glucose.

We have plotted the calibration curve of both H_2O_2 and glucose sensing by CdS nanostructure in Fig. 6.8(d). Here we would like to mention that calibration curve of H_2O_2 was extracted from Fig. 6.5(f) The linear fitting equations of the calibration curves of both H_2O_2 and glucose are shown in the inset of Fig. 6.8(d). Almost identical slope of the two curves attributes to the same reduction rate by CdS nanostructure of bare H_2O_2 and H_2O_2 produced as a reaction byproduct of glucose oxidation by GOx.

For the sake of completeness and better understanding of electrochemical sensing through DET process, same concentration of GOx enzyme, i.e. 1mg/ml was immobilized on CdS-chitosan coated ITO electrodes. For the enzyme coated electrodes, glucose detection is expected to proceed by the DET mechanism, given by the following reaction [163]:

$$Gox\ (ox) + glucose \rightarrow gluconotone + Gox\ (red) \qquad (3a)$$

$$Gox\ (red) \rightarrow Gox\ (ox) + ne^{-} \qquad (3b)$$

Fig. 6.9 (a) reveal the amperometric I-t measurements for GOx coated ITO which goes upto a linear working range of 40 µM, with a sensitivity of 1.7 µA/µMcm^2 and LOD 0.1 µM, which are obtained from the calibration curve of Fig. 6.9 (b). It is evident that the AET process shows a larger accessible working range of glucose sensing with higher sensitivity compared to the DET process, which is possible owing to the availability of higher enzyme concentration in the electrolyte. Hence, from the perspective of sensing performance, GOx dissolved PBS is a better sensing platform. A comparative performance of our results with previously reported CdS composite based glucose sensors are shown in Table 2. These include comparison with CdS-graphene-GOx composite system [164], Ni-CdS working electrode [165], and Ag@Cu-GOx system [166].

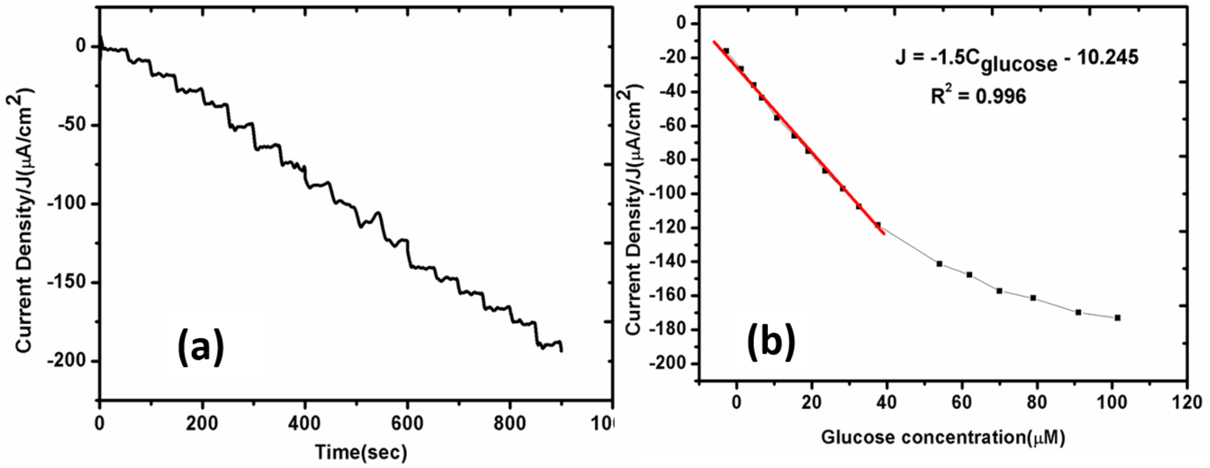

Fig. 6.9: (a) Amperometric I-t curve for successive addition of glucose to GoX immobilized CdS electrode, (b) corresponding calibration curve of glucose concentration vs current density.

Table 2: Comparative performance of recently reported glucose sensors with our work:

Sample	Linear Range	Sensitivity	LOD	Reference
CdS-graphene-GoX	2-16mM	-----	0.7mM	164
Ni-CdS	0.005-12mM	1136.67μA/mMcm^2	0.35μM	165
Ag@Cu-GoX	5-3000μM	-----	0.7μM	166
CdS nanorods GoX mixed in PBS	2-225μM	1.345μA/μMcm^2	0.1μM	Our Work

6.4. Conclusions

To conclude, we have developed an alternative electron transfer process for glucose detection using CdS nanostructures without immobilizing the enzyme on the working electrode. Here we use the GOx enzyme in electrolyte and glucose is oxidized by GOx and H_2O_2 is produced as a reaction by product. This byproduct is reduced further by CdS nanostructures and electron is collected by ITO. Using this technique, we have achieved best limit of detection (0.08 μM) even better than DET process (5 μM). Furthermore, we have developed a systematic approach for optimizing electrochemical sensing performance of CdS coated ITO electrodes. Interesting and meaningful observations were made regarding the role of the binder concentration (chitosan, in our case) in regard with the electrochemical properties. The CdS coated ITO electrodes, shows good sensing characteristics such as high sensitivity and low detection limit towards glucose. Successful detection of glucose concentration in real serum solutions validates its suitability for possible application in diagnostics. A comparative study between our electrode and commercial glucose sensing device suggests that CdS coated ITO electrode (our electrode) shows better results in blood serum compared to the commercial device. Hence CdS coated ITO electrode can be used in glucose monitoring device for diagnostic applications.

CHAPTER 7

Chapter 7

Conclusions and Future Outlook

This Thesis covers three prominent aspects of electrochemical materials science, and they are electrodeposition, electrochemical sensing and electrochemical capacitance (supercapacitance). Our studies show that electrodeposition can be utilized as a low cost, yet highly efficient technique for materials synthesis. In particular, we have formulated a novel synthesis protocol i.e. electrochemical co-deposition for the fabrication of gold nanostructure incorporated manganese oxide film by cyclic voltammetery technique. As discussed extensively in Chapter 3, two sets of electrolyte precursor solutions were used and in the second case the molar concentration of the manganese salt i.e. Manganese Acetate was increase ten-fold i.e. from 0.01 M to 0.1 M. All other conditions of co-electrodeposition were maintained to be the same. For the sake of comparison and to elucidate the role of the incorporated gold nanostructures, pristine manganese oxide samples were synthesized for both the electrolyte precursor concentrations. All the obtained samples were thoroughly characterized in terms of their morphology and structure.

For the first set of co-electrodeposited composite film, a formation mechanism of the Mn_2O_3-Au composite microsphere was proposed based on systematic voltammetry and electron microscopy studies. These results have also been supported with relevant electrochemical reactions. The co-electrodeposition cyclic voltammograms of the second set of electrolyte solutions reveal characteristics similar to the first co-electrodeposition case. Hence, even though the pristine and composite films obtained from the second set of electrodeposition are morphologically different, their structural characteristics are same i.e.

Mn_2O_3 and Mn_2O_3-Au. The same set of electrochemical reactions may be ascribed to their formation. Furthermore, it is evident that a higher concentration of manganese acetate causes a higher rate of deposition of Mn_2O_3 on the ITO substrate, thereby resulting in the disappearance of the microsphere like morphology.

Next, the samples obtained from these two sets of co-electrodeposition were investigated for electrochemical applications. Since the cyclic voltammogram of the sample obtained from the second set of electrodeposition exhibited higher values of current density, they were subsequently applied for electrochemical capacitance studies. Furthermore, the Mn_2O_3-Au microsphere obtained from the first set of co-electrodeposition exhibited good electrochemical sensing performance towards hydrogen peroxide. Detailed electrochemical analysis of the pristine and composite working electrodes were performed with electrochemical impedance spectroscopy, cyclic voltammetery, and amperometric I-t techniques. An improved electrochemical charge transfer behavior of the co-electrodeposited Mn_2O_3-Au composite was observed. An enhanced electrochemical oxidation of H_2O_2 was observed on the composite film. Based on the optimization of operating voltage and electrolyte concentration, a linear aperometric response of upto 500 μM of H_2O_2 was observed and a sensitivity of 39.24 μA/mM cm^2 was obtained along with a low detection limit of 0.34 μM. The composite miscrosphere sample further exhibited acceptable non-interference in the presence of ascorbic acid, uric acid, dopamine and glucose. A comparison with some recent reports of enzyme based and non-enzymatic electrochemical H_2O_2 sensors suggest the acceptable values of sensitivity and limit of detection of the Mn_2O_3-Au composite working electrode.

The electrochemical characterizations of the co-electrodeposited sample for the second set of electrolyte solutions revealed that despite the ten-fold increase of manganese acetate concentration, the same concentration of $HAuCl_4$ is sufficient to improve the electrochemical charge storage properties of the composite film. The Mott-Schottky Analysis revealed a higher charge carrier density of the Mn_2O_3-Au composite film. Frequency and phase analysis show that the composite film depicted improved capacitive properties over the pristine Mn_2O_3 film.

In the case of drop-casted CdS coated ITO working electrodes, a systematic route of electrochemical characterizations proved to be essential. The concentration of binder is crucial towards improving the electrocatalytic properties of drop casted film. A careful optimization led to highly sensitive electrochemical detection of H_2O_2. Furthermore, glucose oxidase dissolved PBS proved to be an alternate direct electron transfer pathway for glucose sensing, without compromising on the electrode's sensitivity and allowing its reusability. These aspects are expected to be crucial for efficient electrochemical sensing of drop casted working electrodes.

With the understanding developed about electrochemical processes performed in this thesis, in future, the following issues may be addressed:

(1) Further tuning of electrochemical co-deposition of manganese oxide with gold or other noble metals in terms of the molar concentrations of constituent electrolyte solutions to investigate the existence of a limiting concentration of noble metal nanostructures in influencing the electrochemical properties of the composite film.
(2) Investigating the possibility of utilizing co-electrodeposition as a generalized synthesis technique for transition metal oxides and sulphides and proposing a systematic optimization route for the same.
(3) Investigating the possibility of extending co-electrodeposition techniques for synthesis of graphene based composites with possible electrochemical applications such as sensing, anti-corrosion and supercapacitance.

Bibliography:

1. Electrochemical Dictionary, Allan J. Bard, Springer-Verlag Berlin Heidelberg, 2012, 2nd Edition
2. M. Bigas, E. Cabruja, High Density of electrodeposited Sn/Ag bumps for flip chip connection, Microelectronic Engineering, 83 (2006) 399-403.
3. E. Gomez, E. Pellicer, E. Valles, Electrodepsited Cobalt-Molybdenum magnetic materials, Journal of Electroanalytical Chemistry 517 (2001) 109-116.
4. Electrodeposited high-magnetic-moment material at writer gap pole, US Patent 6778357
5. Process for electrodeposition of copper chip to chip, chip to wafer and wafer to wafer interconnects in through-silicon vias (tsv), US Patent 20100206737 A1
6. Y. Lin, Q. Lin, X. Liu, Y. Gao, J. He, W. Wang and Z. Fan, A Highly Controllable Electrochemical Anodization Process to Fabricate Porous Anodic Aluminum Oxide Membranes, Nanoscale Research Letters 10 (2015)
7. S. Biring, K.-T. Tsai, U. Kumar Sur and Y.-L. Wang, Electrochemically replicated smooth aluminum foils for anodic alumina nanochannel arrays, Nanotechnology 19 (2007) 015304.
8. P. Roy, S. Berger, P. Schmuki, TiO_2 nanotubes: Synthesis and Applications, Angewandte Chemie 50 (2011) 2904-2939.
9. R. Hang, Y. Liu, L. Zhao, A. Gao, L. Bai, X. Huang, X. Zhang, B. Tang, P. K. Chu, Fabrication of Ni-Ti-O nanotube arrays by anodization of NiTi alloys and their potential applications, Sci Rep. 4 (2014) 7547.
10. Z. Li, Y. Chen, Y. Xin, Z. Zhang, Sensitive electrochemical nonenzymatic glucose sensing based on anodized CuO nanowires on three-dimensional porous copper foam, Sci. Rep 5 (2015)

11. M. C. N.-Martinez, M. P. Kobylanski, P. Mazieraki, J. Wolkiewikz, G. Trykowski, A. Malankowska, M. Kozak, P. J. E.-Montero, and A. Z. Medynska, Self organized TiO2-MnO2 nanotube arrays for efficient photocatalytic degradation of toluene, MDPI Molecules, 22 (2017) 564.
12. J. S. Sagu, K. G. U. Wijayantha, M. Bohm, S. Bohm, T. K. Rout, Anodized Steel electrodes for supercapacitors, ACS Appl. Mater. and Interfaces, 8 (2016) 6277-6285.
13. S. K. Jana, T. Majumder, S. Banerjee, Enhanced photoelectrochemical property of gold nanoparticle sensitized TiO2 nanotube: A crucial investigation at electrode electrolyte interface, Journal of Electroanal. Chem 727 (2014) 99-103
14. L. Shi, C. Wu, J. Ding, Nanoconfined solvothermal synthesis, formation mechanism and photoresponse properties of Cu_2CdSnS_4 nanowires array, Journal of Alloys and Compounds, 683 (2016) 46-50.
15. Z. Liu, W. Yang, L. Chen, J. Jia, Three-Dimensional Copper Foam Supported CuO Nanowire Arrays: An Efficient Non-enzymatic Glucose Sensor, Electrochimica Acta, 235 (2017) 519-526.
16. M. D. Ngyuyen, B. J. Venton, Fast-scan Cyclic Voltammetry for the Characterization of Rapid Adenosine Release, Computational and Structural Biotechnology Journal, 13 (2015) 47-54.
17. S. E. Cooper, B. J. Venton, Fast-scan cyclic voltammetry for the detection of tyramine and octopamine, Analytical and Bioanalytical Chemistry, 394 (2009) 329-336.
18. K. Wang, J. Lu, L. Zhuang, Direct determination of diffusion coefficient for borohydride anions in alkaline solutions using chronoamperometry with spherical Au electrodes 585 (2005) 191-196.

19. A. Remes, A. Pop, F. Manea, A. Baciu, S. J. Picken, J. Schoonman, Electrochemical determination of pentachlorophenol in water on a multi-wall carbon nanotubes-epoxy composite electrode, Sensors 12 (2012) 7033-46.
20. F. Mansfeld, The polarization resistance technique for measuring corrosion technique, Advances in Corrosion Science and Technology, Springer, Boston MA.
21. 3. L. Gray, B. Appleman, “EIS: Electrochemical Impedance Spectroscopy: A Tool to Predict Remaining Coating Life?, JPCL 20, 2 (2003): pp. 66-74.
22. M. Shao, Q. Chang, J. -P. Dodelet, R. Chenitz, Recent Advances in Catalysts for Oxygen Reduction Reaction.Chem. Rev. 116 (2016) 3594-3657.
23. D. Guo, R. Shibuya, C. Akiba, S. Saji, T. Kondo, J. Nakamura, Active sites of nitrogen-doped carbon materials for oxygen reduction reaction clarified using model catalysts, Science 351 (2016) 361-365.
24. K. Yu, W. Kim, C. Chung, Utilization of Pt/Ru catalysts in MEA for fuel cell application by breathing process of proton exchange membrane, Journal of Power. Sources, 163 (2006) 34-40.
25. Morphology dependence of electrochemical properties on palladium nanocrystals, J. Colloid. Interface. Sci. 490 (2017) 190-196.
26. D. Yu, Y. Xue, L. Dai, Vertically Aligned Carbon Nanotube Arrays Co-doped with Phosphorus and Nitrogen as Efficient Metal-Free Electrocatalysts for Oxygen Reduction, J. Phys. Chem. Lett. 3 (2012) 2863-2870.
27. Z. Zhang, J. Liu, J. Gu, L. Cheng, An overview of metal oxide materials as electrocatalysts and supports for polymer electrolyte fuel cells, Energy & Environ Sci, 8 (2014) 2535-2558.
28. J. Dupont, R. F. de Souza, and P. A. Z. Suarez, “Ionic liquid (moltensalt) phase organometallic catalysis,”Chemical Reviews, 102 (2002) 3667–3692.

29. P. Migowski, J. Dupont, “Catalytic applications of metal nanoparticles in imidazolium ionic liquids, Chemistry, 13, (2007) 32–39.
30. J. Dupont, G. S. Fonseca, A. P. Umpierre, P. F. P. Fichtner, and S.R.Teixeira, Transition-metal nanoparticles in imidazolium ionic liquids: recyclable catalysts for biphasic hydrogenation reactions, Journal of the American Chemical Society, 124, (2002) 4228–4229.
31. E. Mourad et.al, Bi-redox ionic liquids with solid like redox density in the liquid state for high energy supercapacitors, Nature Materials, 16 (2017) 446-453.
32. D. Rajkumar, K. Palanivelu, Electrochemical treatment of Industrial wastewater, J. of Hazardous Mat, 113 (2004) 123-129.
33. N. J. Ronkainen, H. B. Halsall, W. R. Heiniman, Electrochemical Biosensors, Chem. Soc. Rev. 39 (2010) 1747-1763.
34. S.V.Dzyadevych, V.N.Arkhypova, A.P.Soldatkin, A.V.El'skaya, C.Martelet, N.Jaffrezic-Renault, Amperometric enzyme biosensors: Past, present and future, IRBM, 29 (2008) 171-180.
35. A. Gonzalez, E. Goikolea, J. A. Barrena, R. Mysyk, Review of Supercapacitors: Technologies and Materials, Renewable and Sustainable Energy Reviews, 58 (2016) 1189-1206.
36. A. D. Pasquier, I. Plitz, S. Menocal, G. Amatucci, A comparative study of Li-ion battery, supercapacitor and nonaqueous asymmetric hybrid devices for automotive applications, J. Power Sources, 115 (2003) 171-178.
37. J. Yang, L. Lian, H. Ruan, F. Xie, M. Wei, Nanostructured porous MnO_2 on Ni foam substrate with a high mass loading via a CV electrodeposition route for supercapacitor application, Electrochimica Acta 136 (2014) 189-194.

38. A. Davies, P. Audette, B. Farrow, F. Hassan, Z. Chen, J.-Y. Choi, A. Yu, Graphene-Based Flexible Supercapacitors: Pulse-Electropolymerization of Polypyrrole on Free-Standing Graphene Films, J. Phys. Chem. C, 115 (2011) 17612-17620.
39. P. Shi et. Al, Design of Amorphous Manganese Oxide@Multiwalled Carbon Nanotube Fiber for Robust Solid-State Supercapacitor, ACS Nano, 11 (2017) 444-452.
40. V. Augustyn, P. Simon, B. Dunn, Pseudocapacitive oxide materials for high-rate electrochemical energy storage, Energy Environ Sci, 7 (2014) 1597-1694.
41. S. Chen, J. Zhu, X. Wu, Q. Han, X. Wang, Graphene Oxide−MnO_2 Nanocomposites for Supercapacitors, ACS Nano, 4 (2010) 2822-2830.
42. D. Saha et.al Studies on Supercapacitor Electrode Material from Activated Lignin-Derived Mesoporous Carbon, Langmuir 30 (2014) 900-910.
43. S. Maity, A. Pramanik, S. Mahanty, Interconnected Network of MnO2 nanowires with a cocoon like morphology: Redox couple Mediated Performance Enhancement in Symmetric Aqueous Supercapacitor, ACS Appl. Mater Interfaces 6 (2013) 1944-8244.
44. R. Kumar. A. Agrawal, R. K. Nagarale, A. Sharma, High performance supercapacitors from novel metal doped ceria decorated aminated graphene, J. Phys. Chem. C, 120 (2016) 3107-3116.
45. X. Lang, A. Hirata, T. Fujita, M. Chen, Nanoporous metal/oxide hybrid electrodes for electrochemical supercapacitors, Nature Nanotechnology 6 (2011) 232-236.
46. Allan J. Bard, Electrochemical Methods: Fundamentals and Applications, Wiley 1980.
47. Israel Rubinstein, Electroanalytical Chemistry: A Series of Advances, CRC Press, 1999.
48. Allan J. Bard, M. Stratmann, I. Rubinstein, M. Fuihira, J. H. Rusling, Encyclopedia of Electrochemistry: Modified Electrodes, Wiley, 2007

49. Andrzej LasiaElectrochemical impedance Spectroscopy and its Applications, Springer New York, 2014.
50. Emil Zolotoyabko, Basic concepts of X-Ray Diffraction, Wiley, 2014.
51. B. Deitzek, Introduction to Fundamentals of Raman Spectroscopy, Springer, 2010.
52. V. V. Nemoshkalenko, Fundamentals of the Method of Photoelectron Spectroscopy, Springer, 1979.
53. JEOL 2000 FX Handbook
54. D. B. Williams and C B Carter, Transmission Electron Microscopy, Plenum, 1996.
55. Peter B. Hirach, Electron Microscopy of thin crystals, Butterworths, 1965.
56. B. Chakraborty, B. Show, S. Jana, B. C. Mitra, S. K. Maji, B. Adhikary, N. Mukherjee, N. Mondal, Cathodic and anodic deposition of FeS_2 thin films and their application in electrochemical reduction and amperometric sensing of H_2O_2, Electrochim. Acta 94 (2013) 7.
57. A. Ramirez, P. Hillebrand, D. Stellmach, M. M. May, P. Bogdanoff, S. Fiechter, J. Phys. Chem. C 118 (2014) 14073-14081.
58. H. K. Schmid, W. Mader, Oxidation States of Mn and Fe in various compound oxide systems, Micron 37 (2006) 426.
59. L. Laffont, P. Gibot, High Resolution Electron Energy Loss Spectroscopy of Manganese Oxides: Application to Mn_3O_4 Nanoparticles 61 (2010) 1268.
60. G. H. Du, Z. W. Yuan, G. W. Tendeloo, Transmission Electron Microscopy and electron energy loss spectroscopy Analysis of Manganese Oxide Nanowires, Appl. Phys. Lett. 86 (2005) 063113.
61. H. Q. Dong, Y. Y. Chen, M. Han, S. L. Li, J. Zhang, J. S. Li, Y. Q. Lan, Z. H. Dai, J. C. Bao, Synergistic Effect of Mesoporous Mn_2O_3-supported Pd Nanoparticle Catalysts

for Electrocatalytic Oxygen Reduction Reaction with Enhanced Performance in Alkaline Medium, J. Mater. Chem. A 2 (2014) 10560.

62. P. Pal, A. K. Giri, S. Mahanty, A. B. Panda, Morphology mediated Tailoring of the performance of porous nanostructured Mn_2O_3 as an anode material, Cryst. Engg. Comm 16 (2014) 10560.
63. M. Chigane, J. Ishikawa, Manganese Oxide thin film preparation by Potentiostatic Electrolysis and Electrochromism, J. Electrochem. Soc. 147 (2000) 2246.
64. Y. Luo, Y. Q. Deng, W. Mao, X.J. Yang, K. Zhu, J. Xu, Y. F. Han, Probing the Surface Structure of a-Mn2O3 nanocrystals during CO oxidation by Operando Raman Spectroscopy, J. Phys. Chem. C 116 (2012) 20975.
65. J. M. Ceratto, M. F. Hochella Jr, W. R. Knocke, A. M. Dietrich, T. F. Cromer, Use of XPS to identify the oxidation state of Mn in solid surfaces of Filtration Media oxide samples from drinking water treatment plants. Environ Sci. Technol. 44 (2010) 5881.
66. J. P. Petitpierre, C. Comninellis and E. Plattner, Electrochim. Acta, 1990, 35, 281–287.
67. SK Jana, T Majumder, S Banerjee, Enhanced photoelectrochemical property of gold nanoparticle sensitized TiO2 nanotube: A crucial investigation at electrode-electrolyte interface, J. Electroanal. Chem, 727 (2014) 99-103.
68. S. Zhang, K. J. T. Livi, A. C. Gaillot, A. T. Stone and D. R. Veblen, Determination of manganese valence states in (Mn3+, Mn4+) minerals by electron energy-loss spectroscopy Am. Mineral., 2010, 95, 1741–1746.
69. G. H. Du, Z. Y. Yuan and G. V. Tendeloo, Transmission electron microscopy and electron energy-loss spectroscopy analysis of manganese oxide nanowires, Appl. Phys. Lett., 2005, 86, 063113–063113.

70. J. Duay, S. A. Sherril, Z. Gui, E. Gillette and S. B. Lee, Self-Limiting Electrodeposition of Hierarchical MnO2 and M(OH)2/MnO2 Nanofibril/Nanowires: Mechanism and Supercapacitor Properties, ACS Nano, 2013, 7, 1200–1214.
71. T. Reidl, T. Gemming and K. Wetzig, Extraction of EELS white-line intensities of manganese compounds: Methods, accuracy, and valence sensitivity, Ultramicroscopy, 2006, 106, 284–291.
72. D. H. Pearson, C. C. Ahn and B. Fultz, White lines and d-electron occupancies for the 3d and 4d transition metalsPhys. Rev. B: Condens. Matter, 1993, 47, 8471–8478.
73. J. Soji Adeyinka, A. Rim-Rukeh, Effect of Hydrogen Peroxide on Industrial Waste Water Effluents: A Case Study of Warri Refining and Petrochemical Industry, Environ. Monitoring and Asessment, 1999, 59, 249-256.
74. S. B. Berger, L. E. S.Soares, A. A. Martin, G. M. B. Ambrosano, C. P. Tabchoury, M. Giannini, Effects of various hydrogen peroxide bleaching concentrations and number of applications on enamel, Braz. J. Oral Sci. 2014, 13, 1677-3225.
75. I. A. Smellie et.al, Alternative Hydrogen Peroxide Sources for Peroxyoxalate “Glowstick” Chemiluminescence Demonstrations, J. Chem. Educ., 2017, 94, 112-114.
76. M. Nasir, M. H. Nawaz, U. Latif, M. Yaqub. A. Hayat, A. Rahim, An overview on enzyme-mimicking nanomaterials for use in electrochemical and optical assays, Microchim. Acta, 2017, 184, 323-342.
77. A. A. Karyakin, E. E. Karyakina, Prussian Blue-based `artificial peroxidase' as a transducer for hydrogen peroxide detection. Application to biosensors, Sens. Act. B:Chemical, 1999, 57, 268-273.
78. T. Margaf, Comparison between Folin-Ciocalteu and Prussian Blue Assays to Estimate The Total Phenolic Content of Juices and Teas Using 96-Well Microplates., J. Food Sci., 2015, 80, 2397-23403.

79. G. Zhao, .J.-J. Feng, J.-J. Xu, H.-Y. Chen, Direct electrochemistry and electrocatalysis of heme proteins immobilized on self-assembled ZrO_2 film, Electrochem. Commun. 2005, 7, 724-729.
80. I. V. Zaporotskovaa, N. P. Borozninaa, Y. N. Parkhomenkob, L. V. Kozhitov, Carbon nanotubes: Sensor properties. A review, Modern Electron. Mat. 2016, 2, 95-105.
81. C. M. Lousada, A. J. Johansson, T. Brinck, M. Jonsson, Mechanism of H_2O_2 decomposition on Transition Metal Oxide Surfaces, J. Phys. Chem. C, 2012, 116, 9533-9543.
82. M. Sui, L. She, Review on research and application of mesoporous transitional metal oxides in water treatment, Front. of Environ. Science and Engg., 2013, 7, 795-802.
83. Z. Taha, J. Wang, Electrocatalysis and flow detection at a glassy carbon electrode modified with a thin film of oxymanganese species, 1991, 3, 215-219.
84. S. Yao, J. Xu, Y. Wang, S. Hu, A highly sensitive hydrogen peroxide amperometric sensor based on MnO_2 nanoparticles and dihexadecyl hydrogen phosphate composite film, Anal. Chim. Acta, 2006, 557, 78-84.
85. Y.-S. Ding et.al, Synthesis and Catalytic Activity of Cryptomelane-Type Manganese Dioxide Nanomaterials Produced by a Novel Solvent-Free Method, Chem. Mater. 2005, 17, 5382-5389.
86. L.-C. Chang, W.-D. Zhang, Electrodeposition of TiO_2 Nanoparticles on Multiwalled Carbon Nanotube Arrays for Hydrogen Peroxide Sensing, Electroanalysis, 2009, 21, 988-993.
87. B. Xu, M.-L. Ye, Y.-X. Yu, W.-D. Zhang, A highly sensitive hydrogen peroxide amperometric sensor based on MnO2-modified vertically aligned multiwalled carbon nanotubes, Anal. Chim. Acta, 2010, 674, 20-26.

88. Y.-H. Bai, H. Zhang, J.-J. Xu, H.-Y. Chen, Relationship between Nanostructure and Electrochemical/Biosensing Properties of MnO_2 Nanomaterials for H_2O_2/Choline, J. Phys. Chem. C, 2008, 112, 18984-18990.
89. R. Sharma et.al, Label-free electrochemical impedance biosensor to detect human interleukin-8 in serum with sub-pg/ml sensitivity, Biosens. Bioelectron, 2016, 80, 607-613.
90. M. Gerlache, Z. Senturk, G. Quarin, J.-M. Kauffman, Electrochemical behaviour of H_2O_2 on gold, Electroanalysis, 1997, 9, 1088.
91. N. Jia, B. Huang, L. Chen, L. Tan, S. Yao, A simple non-enzymatic hydrogen peroxide sensor using gold nanoparticles-graphene-chitosan modified electrodes, Sens. Actuators B 2014, 195, 165.
92. F. Chekin, L. Gorton, I. Tapsobea, Direct and mediated electrochemistry of peroxidase and its electrocatalysis on a variety of screen printed carbon electrodes: amperometric hydrogen peroxide and phenols biosensor, Anal. Bioanal. Chemistry 2015, 407, 439.
93. B. Haghighi, H. Hamidi, L. Gorton, Electrochemical behaviour and application of Prussian blue nanoparticle modified graphite electrode, Sens. Actuators B 2010, 147, 270.
94. X. Yu, G.A. Sotzing, F. Papadimitrakopoulos, J.F. Rusling, Wiring of enzymes to electrodes by ultrathin conductive polyion underlayers: enhanced catalytic response to hydrogen peroxide, Anal. Chem. 2003, 75, 4565.
95. B.V. Chikkaveeraiah, H. Liu, V. Mani, F. Papadimitrakopoulos, J.F. Rusling, A microfluidic electrochemical device for high sensitivity biosensing: detection of nanomolar hydrogen peroxide, Electrochem. Commun. 2009, 11, 819.
96. F. Meng, X. Yan, J. Liu, J. Gu, Z. Zou, Nanoporous Gold and non-enzymatic sensor for hydrogen peroxide, Electrochim. Acta, 2011, 56, 4657.

97. I.G. Gazaryan, L. Gorton, T. Ruzgas, E. Csoregi, W. Schuhmann, L.M. Lagrimini, D. M. Khushpul'yan, V.I. Tishkov, Tobacco peroxidise as a new reagent for amperometric biosensors, Journl. Of Anal. Chem 2005, 60, 558.

98. L. Li, Z. Du, S. Liu, Q. Hao, Y. Wang, Q. Li, T. Wang, A novel non-enzymatic hydrogen peroxide sensor based on MnO_2/grapheme oxide nanocomposite, Talanta 2012, 82, 1637.

99. X. Guo, D. Zheng, N. Hu, Enhancement of Au nanoparticles formed by in situ electrodeposition on direct electrochemistry of myoglobin loaded into layer- by-layer films of chitosan and silica nanoparticles, J. Phys. Chem. B 2008, 112, 15513.

100. H. J. Gores, H. J. Schweiger, Electrolytes for Electrochemical Double Layer Capacitors, Encyclopedia of Applied Electrochemistry, 2014.

101. P. Sharma, T. S. Bhatti, A review on electrochemical double layer capacitors, Energy Conversion and Management, 2010, 51, 2901-2912.

102. C. Costentin, T. R. Porter, J.-M. Saveant, How do pseudocapacitors store energy? Theoretical Analysis and Experimental Illustration, ACS Appl. Mater. Interfaces, 2017, 9, 8649-8658.

103. Y. Wang, Y. Song, Y. Xia, Electrochemical capacitors: mechanism, materials, systems, characterization and applications, Chem. Soc. Rev. 2016, 45, 5925-5950.

104. R. B. Rakhi, W. Chen, D. Cha, H. N. Alshareef, High performance supercapacitors using metal oxide anchored graphene nanosheet electrodes, J. Mater. Chem, 2011, 21, 16197-16204.

105. A. A. Alguaila,, A. H. Al-Eggielya, M. M. Gvozdenović, B. Z. Jugovićb, B. N. Grgur, Battery type hybrid supercapacitor based on polypyrrole and lead-lead sulfate, J. Power Sources, 2016, 313, 240-246.

106. L. Wang, H. Ji, S. Wang, L. Kong, X. Jianga, G. Yang, Preparation of Fe_3O_4 with high specific surface area and improved capacitance as a supercapacitor, Nanoscale, 2013, 5, 3793-3799.

107. J. S. Sagu, K. G. U. Wijayantha, M. Bohm, S. Bohm, T. K. Rout, Anodized Steel Electrodes for Supercapacitors, ACS Appl. Mater. Interfaces, 2016, 8, 6277-6285.

108. X. Xiao et.al, Freestanding functionalized carbon nanotube-based electrode for solid-state asymmetric supercapacitors, Nano Energy, 2014, 6, 1-9.

109. L. Huang, B. Yao, J. Sun, X. Gao, J. Wu, J. Wan, T. Li, Z. Hu, J. Zhou, Highly conductive and flexible molybdenum oxide nanopaper for high volumetric supercapacitor electrode, J. Mater. Chem. A, 2017,5, 2897-2903.

110. M. Beidaghi, C. Wang, Micro-Supercapacitors Based on Interdigital Electrodes of Reduced Graphene Oxide and Carbon Nanotube Composites with Ultrahigh Power Handling Performance, Adv. Mater., 2012, 7, 4501-4510.

111. C. Du, N. Pan, High power density supercapacitor electrodes of carbon nanotube films by electrophoretic deposition, 2006, 17.

112. M. Li, Z. Tang, M. Leng, J. Xue, Flexible solid-state supercapacitor based on graphene-based hybrid films, Adv. Funct. Mater., 2014, 24, 7495-7502.

113. A. Gonzáleza, E. Goikoleab, J. A. Barrenaa, R. Mysyk, Review on supercapacitors: Technologies and materials, Renewable Sustnbl Energy Rev. 2016, 58, 1189-1206.

114. L. Li, Z. A. Hu, N. An, Y. Y. Yang, Z. M. Li, H. Y. Wu, Facile Synthesis of MnO_2/CNTs Composite for Supercapacitor Electrodes with Long Cycle Stability, J. Phys. Chem. C 2014, 118, 22865-22872.

115. Y. H. Lee, J. B. Goodenough, Supercapacitor Behavior with KCl electrolyte, J. Solid State Chem. 1999, 144, 220-223.

116. R. Abdur, K. Kim, J. -H. Kim, J. Lee, Electrochemical behavior of manganese oxides on flexible substrates for thin film supercapacitors, Electrochim. Acta, 2015, 153, 184-189.

117. A. M. A. Hashem, H. Abuzeid, A. A.- Ghany, C. Julien, SnO_2–MnO_2 composite powders and their electrochemical properties, J. Power Sources, 2012, 202, 291-298.

118. S. A. Hashmi, H. M. Updahyaya, MnO_2-polypyrrole conducting polymer composite electrodes for electrochemical redox supercapacitors, Ionics, 2002, 8, 272-277.

119. H. Lee, J. Kang, M. S. Cho, J.-B. Choic, Y. Lee, MnO_2/graphene composite electrodes for supercapacitors: the effect of graphene intercalation on capacitance, J. Mater. Chem, 2011, 21, 18215-18219.

120. L. Li, Z. A. Hu, N. An, Y. Y. Yang, Z. M. Li, H. Y. Wu, Facile Synthesis of MnO_2/CNTs Composite for Supercapacitor Electrodes with Long Cycle Stability, J. Phys. Chem. C, 2014, 118, 22865–22872.

121. J. M. Ko, K. M. Kim, Electrochemical properties of MnO_2/activated carbon nanotube composite as an electrode material for supercapacitor, Mat. Chem. Phys., 2009, 114, 837-841.

122. S. Park, I. Nam, G.-P. Kim, J. Yi, A Hybrid MnO2 Film with Agarose Gel for Enhancing the Structural Integrity of Thin Film Supercapacitor Electrodes, ACS Appl. Mater. Interfaces, 2013, 5, 9908–9912.

123. Y. Jiao, A. Hellman, Y. Fang, S. Gao, M. Kall, Schottky barrier formation and band bending revealed by first- principles calculations, Sci. Rep. 2015, 5, 11374.

124. X. Lu, Y. Zeng, M. Yu, T. Zhai, C. Liang, S. Xie, M. S. Balogun, Y. Tong, Oxygen-Deficient Hematite Nanorods as High-Performance and Novel Negative Electrodes for Flexible Asymmetric Supercapacitors Adv. Mater., 2014, 26, 3148– 3155.

125. V. G. Bhide and R. V. Damle, Dielectric properties of manganese dioxide part I, Physica, 1960, 26, 33 –42.

126. J. Gamby, P. L. Taberna, P. Simon, J. F. Fauvarque, M. Chesneau, Studies and characterisations of various activated carbons used for carbon/carbon supercapacitors J. Power Sources, 2001, 101, 109–116.

127. P. L. Taberna, C. Portet and P. Simon, Electrode surface treatment and electrochemical impedance spectroscopy on carbon/carbon supercapacitors, Appl. Phys. A, 2006, 82, 639–646.

128. K. Sheng, Y. Sun, C. Li, W. Yuan, G. Shi, Ultrahigh-rate supercapacitors based on eletrochemically reduced graphene oxide for ac line-filtering Sci. Rep., 2012, 2,1 –5.

129. P. L. Taberna, P. Simon and J. F. Fauvarque, Electrochemical Characteristics and Impedance Spectroscopy Studies of Carbon-Carbon Supercapacitors J. Electrochem. Soc., 2003, 148, A292–A300.

130. C. Portet, P. L. Taberna, P. Simon, E. Flahaut and C. L. Robert, High power density electrodes for Carbon supercapacitor applications, Electrochim. Acta, 2005, 50, 4174–4181.

131. P. Simon and Y. Gogotsi, Materials for electrochemical capacitors, Nat. Mater., 2008, 7, 845–854.

132. S. K. Jana, V. P. Rao and S. Banerjee, Enhancement of supercapacitance property of electrochemically deposited MnO_2 thin films grown in acidic medium, Chem. Phys. Lett., 2014, 593, 160–164.

133. P. C. Chen, G. Shen, Y. Shi, H. Chen and C. Zhou, Preparation and Characterization of Flexible Asymmetric Supercapacitors Based on Transition-Metal- Oxide Nanowire/Single-Walled Carbon Nanotube Hybrid Thin-Film Electrodes, ACS Nano, 2010, 4, 4403–4411.

134. Renato S. Freire, Christiana A. Pessoa, Lucilene D. Mello and Lauro T. Kubota, Direct electron transfer: an approach for electrochemical biosensors with higher selectivity and sensitivity, J. Braz. Chem. Soc., Vol. 14, No. 2, 230-243, 2003
135. M. Wooten, S. Karra, M. Zhang, and W. Gorski, On the direct electron transfer, sensing, and enzyme activity in the glucose oxidase/carbon nanotubes system, Anal. Chem., 2014, 86, 752–757.
136. Y. Zhang, J. Lei, Q. Hao, H. Ju, Photoelectrochemical Immunosensor for Detection of Carcinoembryonic Antigen Based on 2D TiO2 Nanosheets and Carboxylated Graphitic Carbon Nitride, Biosens Bioelectron. 2016, 77, 557-564.
137. H. Dhyani, Md. A. Ali, M. K. Pandey, B. D. Malhotra, and P. Sena, Electrophoretically deposited CdS quantum dots based electrode for biosensor application, J. Mater. Chem., 2012, 22, 4970-4976.
138. L. Xia, L. Xu, J. Song, R. Xu, D. Liu, B. Dong, H. Song, CdS quantum dots modified CuO inverse opal electrodes for ultrasensitive electrochemical and photoelectrochemical biosensor, Sci Rep., 2015, 5, 10838.
139. J. Qian, S. Yan, Z. Xiao, Electrochemical biosensor based on CdS nanoastructure surfaces, J Colloid Interface Sci., 2012, 366, 130-134.
140. G. Jie, B. Liu, H. Pan, J.-J. Zhu, and H.-Y. Chen, Anal. Chem., 2007, 79, 5574-5581.
141. C. Z. Wang, Y. F. E., L. Z. Fan, Z. H. Wang, H. B. Liu, Y. L. Li, S. H. Yang, Y. L. Li, Adv. Mater., 2007, 19, 3677-3681.
142. J. Zhang, C. Xu, D. Zhang, J. Zhao, S. Zheng, H. Su, F. Wei, B. Yuan, and C. Fernandez, J. of Electrochem. Soc., 2017, 164, 4, B92-B96.
143. Y. Sun, M. Luo, Y. Qin, S. Zhu, Y. Li, N. Xu, X. Meng, Q. Ren, L. Wang, and S. Guo, ACS Appl. Mater. Interfaces, 2017, 9, 40697–40706.

144. A. Kar, A. Datta, A. Patra, Fabrication and optical properties of core /shell CdS/LaPO4:Eu nanorods, J. Mater. Chem., 2010, 20, 916-922.

145. J. C. Ramos, I. Mejia, C. A. Martinez, M. A. Q.-Lopez, Direct on chip cadmium sulphide thin film transistors via modified chemical surface deposition, J. Mater. Chem. C, 2013, 1, 6653-6660.

146. B. K. Shrestha, R. Ahmad, H. M. Mousa, I.-G. Kim, J. I. Kim, M. P. Neupane, C. H. Park, and Cheol Sang Kim, J. Coll. Intf. Sci, 2016, 482, 39-47.

147. L. F. Ang, L. Y. Por, M. F. Yam, Plos One, 2013, 8, e70597.

148.. W. Zhang, X. Li, R. Zou, H. Wu, H. Shi, S. Yu and Y. Liu, Designed self-assembled hybrid Au@CdS core-shell nanoparticles with negative charge and their application as highly selective biosensors, Sci. Rep., 2015, 5, 11129.

149. Y. Huang, C. Cheng, X. Tian, B. Zheng, Y. Li, H. Yuan, D. Xiao, M. M. F. Choi, Electrochim. Acta, 2013, 89, 832-839.

150. S. A. Bhat, M. A. Rather, S. A. Pandit, P. P. Ingole, M. A. Bhat, Oxides in silver-graphene nanocomposites: electrochemical signatures and electrocatalytic implications Analyst, 2015, 140, 5601.

151. S. K. Maji, A. K. Dutta a, D. N. Srivastava, P. Paul, A. Mondal, and B. Adhikary, J. Mol. Cat. A: Chem, 2012, 358, 1-9.

152. V. Linek, P. Benes, J. Sinkule, O. Holecek, and V. Maly, Adv. Sci., 1980, 22, 2515-2527.

153. A. K. Dutta, S. Das, P. K. Samanta, S. Roy, B. Adhikary, P. Biswas, Electrochim. Acta, 2014, 144, 282-287.

154. B. Saha, S. K. Jana, S. Majumder, B. Satpati, and S. Banerjee, Selective Growth of Co-electrodeposited Mn2O3-Au Spherical Composite Network Towards Enhanced Non-enzymatic Hydrogen Peroxide Sensing, Electrochim. Acta, 2015, 174, 853-863

155. A. K. Dutta, S. K. Maji, D. N. Srivastava, A. Mondal, P. Biswas, P. Paul, B. Adhikary, Synthesis of FeS and FeSe nanoparticles from a single source precursor: A study of their photocatalytic activity peroxidase like behaviour, and electrochemical H2O2 sensing, ACS Appl. Mater. Interfaces, 2012, 4, 1919-1927.

156. A. K. Dutta, S. Das, P. K. Samanta, S. Roy, B. Adhikary, P. Biswas, Non-enzymatic amperometric sensing of hydrogen peroxide at a CuS modified electrode for the determination of urine H_2O_2, Electrochim. Acta, 2014, 144, 282-287.

157. S. K. Maji, A. K. Dutta a, D. N. Srivastava, P. Paul, A. Mondal, and B. Adhikary, Peroxidase-like behaviour, amperometric biosensing of hydrogen peroxide and photocatalytic activity by cadmium sulphide nanoparticles, J. Mol. Cat. A: Chem, 2012, 358, 1-9.

158. V. Linek, P. Benes, J. Sinkule, O. Holecek, and V. Maly, Adv. Sci., 1980, 22, 2515-2527.

159. M. Elkaoutit, I.N. Rodriguez, M. Domínguez, M.P.H. Artiga, D.B. Milla, J.L.H. Hidalgo de Cisneros, A third-generation hydrogen peroxide biosensor based on Horseradish Peroxidase (HRP) enzyme immobilized in a Nafion–Sonogel–Carbon composite, Electrochim. Acta, 2008, 53, 7131–7137.

160. S. Dong, Q. Yang, L. Peng, Y. Fang, T. Huang, Dendritic Ag@Cu bimetallic interface for enhanced electrochemical responses on glucose and hydrogen peroxide, Sens. Actuators B, 2016, 232, 375-382.

161. J. Li, Y. Tang, J. Yang, Z. Yang, Y. Zhang, X. Hu, Cage-like PbS nanostructure for the construction of novel glucose electrochemical biosensor, Sens. and Actuators B, 2014, 190, 549-554.

162. H. Zheng, H. Xue, Y. Zhang, Z. Shen, A glucose biosensor based on microporous polyacrilenitrile synthesized by single rare earth catalyst, Biosens. Bioelectron., 2002, 17, 541-545.

163. X. Zhang, Q. Liao, M. Chu, S. Liu, Y. Zhang, Structure effect on graphene-modified enzyme electrode glucose sensors, Biosens. Bioelectron., 2014, 52, 281-287.

164. K. Wang, Q. Liu, Q.-M. Guan, J. Wu, H.-N Li, J.-J. Yan, Enhanced direct electrochemistry of glucose oxidase and biosensing for glucose via synergy effect of graphene and CdS nanocrystals, Biosens. and Biolectronics 26 (2011) 2252-2257.

165. C. Guo, H. Huo, X. Han, C. Xu, H. Li, Ni/CdS bifunctional Ti@TiO2 core-shell nanowire electrode for high performance nonenzymatic glucose sensing, Anal. Chem.86 (2014) 876-883.

166. S. Dong, Q. Yang, L. Peng, Y. Fang, T. Huang, Dendritic Ag@Cu bimetallic interface for enhanced electrochemical responses on glucose and hydrogen peroxide Sens. Actuators B 232 (2016) 375-382.